TECHNISCHE UNIVERSITÄT WIEN
Vienna | Austria

Dissertation

Phase transformation derived protective effects of PVD coatings

carried out for the purpose of obtaining the degree of PhD (or Dr. tech.), submitted at TU Wien, Faculty of Mechanical and Industrial Engineering, by

Dipl.-Ing. Bernhard Kohlhauser

Mat.Nr.: 0826032

Anschützgasse 25/3, 1150 Wien, Austria

under the supervision of

Univ.Prof. Dipl.-Ing. Dr.mont. Paul Heinz Mayrhofer

at the

Institute of Materials Science and Technology, E308

reviewed by

Prof. Dr. Ali Erdemir

Argonne National Laboratory,

Energy Systems Divison

9700 Cass Avenue, IL 60439, USA

Univ.-Prof. Dr.-Ing. Carsten Gachot

Institute for Engineering Design and

Logistics Engineering, TU Wien

Getreidemarkt 9, 1060 Wien

Vienna, December 2018

This work was supported by the Austrian COMET-Program (Project 2 X Tribology, Grant no. 849109) and has been carried out within the TU Wien, Argonne National Laboratory and the Excellence Centre for Tribology AC2T research GmbH (Wiener Neustadt, Austria).

Affidavit

I declare in lieu of oath, that I wrote this thesis and performed the associated research myself, using only literature cited in this volume.

Date

Signature

Acknowledgements

First and foremost, I want to thank **Univ.Prof. Dipl.-Ing. Dr.mont. Paul Heinz Mayrhofer** for giving me the opportunity to perform my research and write this thesis in his group. It often was not easy for him to keep track of all of us and to find time in his busy schedule, yet he always managed to provide important input and pass on his knowledge. His unbreakable fascination with materials science were a big motivator for all of us. **Thank you, Paul!**

My research would have been impossible without the help of **Dr. Helmut Riedl** as well as **Univ.-Prof. Dr.-Ing. Carsten Gachot**. Whenever a problem or unanswered question arose, they were the first to help find a solution.

I also want to thank **Paul** and **Carsten**, for supporting my ambitions to perform part of my research in the United States. In this context, I want to thank **Dr. Ali Erdemir** for accepting me as a guest student at Argonne National laboratory and including me to his team. A special thanks goes to **Dr. Giovanni Ramirez**, who also helped me finding my way around their lab, and **Dr. Osman Levent Eryilmaz** for helping me to stay positive through all Chicago-crises.

Furthermore, I want to thank the postdoc team (**Christian**, **Matthias** and **David**) for all their input and interesting discussions.

At this point, I want to thank **Dr. Manel Rodríguez Ripoll** for organizing the framework of my Ph.D. position and want to thank **all my co-authors** for their support and contribution.

Thank you, **DI Werner Artner**, you are the fairy godmother of the Getreidemarkt 9. Without him our coating systems would probably still be homeless and the whole campus most likely would not work as well as it does.

Heartfelt thanks go to **all my active and former colleagues** on both sides of the Atlantic Ocean. In particular, I want to mention those who shared an office with me and over the last years have become close friends: **Vincent** (and his relentless hunger for Schnitzel), **Valentin** (who did not allow one misspelled word to sneak past him), **Philipp** (who is the only man, standing between us and the collapse of all equipment), **Elias** (the call-cemter king, for his artistic eye as well as for lifting everybody's spirit) and **LukiLukiLuki** (who might have failed his peanut duties, but anyway always contributed to a good mood in the office).

I am profoundly grateful to all my **friends and family**, for all their support and for making the last three years a wonderful time. In particular, I want to highlight a few groups of close friends: The **Chicago Winterkinder** for making my time in the States a very exciting and fortunate experience on a private level as well. The **Sieger der Herzen**, who not only supported me during my studies, but also continued being close friends and valuable colleagues afterwards. The **DIENSTAG** community might not have promoted efficient work on Wednesdays, but were essential in recharging my physical and mental batteries (while being taught additional knowledge of the Universe by **Otto Clemens**).

Stela, I do not dare to imagine, what the last years would have looked like without you. You showed me parts of the world that I would have never seen on my own. You always supported me in everything I wanted to do, and told me what I really needed to hear (whether I wanted to, or not). With you, my life will never get boring and that is the greatest gift anybody could give me.

Thank you!

Table of content

Acknowledgements I

Table of content III

Abstract VI

List of Figures VIII

List of Abbreviations XV

1 Introduction 1

2 Theoretical Background 5

2.1 Phase Transformations 5

2.1.1 Phase Stability 6

2.1.2 Nucleation and Growth 9

2.1.3 Solid-State Phase Transformations 10

2.1.4 Pressure-Induced Solid-state Phase Transformations 11

2.2 From Friction to Tribofilm Formation 12

2.2.1 Tribology: Friction, Wear and Lubrication 12

2.2.2 Tribofilms and their Formation 20

2.3 Material Systems 22

2.3.1 Tungsten Nitride 22

2.3.2 Transition Metal Dichalcogenides 23

2.3.3 Alumina and Alumina Thin Films 25
3 Methodical Approach: From Synthesis to Analytics 30
3.1 Thin Films: Deposition and Growth 30
3.1.1 Sputtering 32
3.1.2 Magnetron Sputtering 36
3.1.3 Reactive Sputtering 37
3.1.4 Film Growth 40
3.2 Tribofilm Analysis and its Difficulties 43
3.2.1 Scanning Electron Microscopy and Focused Ion Beam 44
3.2.2 Energy-Dispersive X-ray Spectroscopy 45
3.2.3 X-ray Photoelectron Spectroscopy 46
3.2.4 Secondary Ion Mass Spectroscopy 48
3.2.5 Raman Spectroscopy 50
4 In-situ formation of high performance low-friction tribofilms 52
4.1 Following Breadcrumbs towards In-situ Solid Lubrication 56
4.2 Tungsten Nitride Coatings – the Key to In-situ WS_2 Formation 60
4.3 Summary (Chapter IV) 66
4.4 Additional Information 67
4.4.1 Specific Methods 67
4.4.2 Supplemental Information 73
5 Reactive Self-assembly of MoS_2 for Low Friction 77
5.1 Methods 79
5.2 Results and Discussion 81
5.3 Summary (Chapter V) 91

6 Rebound Sputtering and the Mechanical Properties of Transition Metal doped Alumina Thin Films 93

6.1 Experimental 96

6.2 Results and Discussion 98

6.3 Summary (Chapter VI) 111

7 Influencing the γ- to α-Al_2O_3 Phase Transformation in Thin Films 112

7.1 Results and Discussion 114

8 Conclusion 123

9 Contribution to the Field 128

10 Financial and Experimental Support 130

11 References 131

Abstract

Phase formation and phase transformations are of high interest for the development of thin films. Thin film materials regularly experience phase transformations, whereat the transformation occurs either at the coating to atmosphere interface (e.g. corrosion, oxidation, catalytic/mechanochemical effects and many more) or within the coating itself (e.g., decomposition, structural changes or chemical changes). This work focuses on two effects: the influence of W or Mo based coatings on the tribofilm formation for wear-protective applications, as a surface phase transformation, while the thermally induced transformation of metastable γ-Al_2O_3 thin films to α-Al_2O_3 represents solid state coating phase transformations.

To gain a better understanding of the in-situ formation of transition metal disulfide based tribofilms, detailed studies, uncovering the reaction pathway in uncoated metallic W and Mo contacts, have been carried out. The conclusions were utilized to design a coating that allows for exceptional wear protection via the formation of a crystalline WS_2 phase. The lubricating nature of the tribofilm was established in ball on disk tests and the formation of WS_2 confirmed by Raman spectroscopy and transmission electron microscopy.

In terms of solid-state phase transformation of the coating, the influence of heavy element micro-alloyed Al-targets on the deposition process of alumina thin film was investigated. While the dopants (Cr, Mo, Nb or W) generally lead to a stabilization of

the deposition process, they have very different influences on the deposition rate, structure and mechanical properties of alumina thin films. Low levels of W show the overall most beneficial effect, and a particularly high increase of the deposition rate as a result of the rebound sputtering effect. Doping alumina coatings with W also showed the most favorable influence on the γ- to α-Al_2O_3 transformation in differential scanning calorimetry and non-ambient temperature X-ray diffraction measurements, delaying the transformation to higher temperatures. This delay is contributed to a solute drag effect as well as the minimization of surface energy. It therefore opens alumina thin films, produced by physical vapor deposition, to applications at high temperatures.

List of Figures

Figure 1: Illustration of the Gibbs free energy of a material (constant temperature and chemical composition) with respect to the arrangement of its atoms (adapted from [21])....7

Figure 2: Effect of the mixing enthalpy and temperature on the Gibbs free energy of mixing, showing the formation of a miscibility gap with a positive mixing enthalpy at low temperatures (adapted from [21])....8

Figure 3: Stribeck curve of a lubricated contact. The contact schematics highlight the separation of the surfaces by a lubricant film and defines three different regimes of hydrodynamic lubrication....15

Figure 4: Schematics of the four wear mechanisms, highlighting the interaction and influences of surfaces (adapted from [57])....18

Figure 5: Symbolic S-Me-S sandwich structure of the TMDs [120]....24

Figure 6: Unit cell of (a) γ- and (b) α-Al_2O_3. Only 83 % of the atom-sites that are not fully colored are occupied [120]....28

Figure 7: Arrangement of a magnetron sputtering system that allows for the use of reactive gases. The magnetic field-lines trap electrons close to the target to allow for sputtering at lower pressures and lead to the formation of the race track....33

Figure 8: Schematic of a voltage-current characteristic for different regimes in plasma discharges adapted from [42] 34

Figure 9: Common events after ion impact on a surface, highlighting the collision cascade [166]. 35

Figure 10: Poisoning behavior of an Al target in Ar/O_2 mixture, demonstrating the three operation modes in reactive sputtering. 40

Figure 11: The structure zone model, as proposed by A. Anders [181], provides information about the influence of the deposition parameters on the morphology of coatings. 42

Figure 12: High-resolution XPS fitted spectra of S 2p (top) and W 4f (bottom) for a WC hammer peened surface with 1.5% EP additive, tested at 10 N load [186]. 48

Figure 13: SIMS image (WO^{2-}/WS^{-} signal) of a WS_2 containing tribofilm 50

Figure 14: The proposed tribochemical reaction is separated into three steps (and works for W and Mo analogically). In the 3rd step, the initially amorphous WS_2 undergoes a shear stress induced self-organization [88, 131, 198]. 55

Figure 15: (a) Interactions of the Mo surface with 2 at.-% S in the oil lead to a drastic reduction of the COF. While metallic W surfaces do not follow this low friction behavior, a thermally annealed tungsten oxide surface demonstrate an immediate drop in friction at sufficient S concentrations in the lubricant. (b) The low COF for S-containing tests on Mo and oxidized W can be directly linked to the formation of MoS_2 and WS_2 respectively, via Raman spectroscopy of the wear scar on the counter body while on W no sulfide is formed. 58

Figure 16: (a) The in-situ formation of MoS_2 offers excellent wear protection (e). (b) Tests on W surfaces lead to the formation of abrasive particles and (f) result in high

wear on the ball. (c) A similar wear mechanism can be noticed on oxidized W surfaces without the presence of S. (d) The addition of 1.2 at.-% S to the contact sustains the formation of WS_2, leading to the same polishing as with Mo and averting any measurable wear (g).....59

Figure 17: (a) Low friction via the in-situ generation of WS_2 can also be achieved by applying coatings in the presence of S containing additives. The evolution of the COF depends on the contact pressure, as the tribofilm suffers from higher loads. Raman spectroscopy (b) demonstrates that WS_2 has formed in higher amounts as the contact pressure increases. (c) Without any additive to react and form the WS_2 based tribofilm, the wear is quite severe and increases proportionally. (d) Although (despite the presence of the S containing additive), the COF increases for higher contact pressures, the wear protection capabilities are still excellent pushing the amount of wear below detectable levels.....61

Figure 18: (a) The contact area of a ball at 0.9 GPa with 2 at.-% S exhibits no measurable wear and presents areas of accumulated debris (investigated by Raman spectroscopy, contains WS_2) and tribofilm, that has been investigated with TEM. (b) The coated flat does not show any measurable wear as well, but illustrates the formation of a debris zone around the wear track (intensifying with the contact pressure). This area was investigated with secondary ion mass spectroscopy (c) revealing a high concentration of S in the debris, while (d) oxygen species are absent from the debris.....63

Figure 19: (a) The tribofilm (protected by an Au and Pt layer), that formed on the Si_3N_4 ball, was investigated with TEM and exhibits a mostly amorphous appearance. (b) In the tribofilm crystalline WS_2 nanoparticles are embedded. (c) The chemical composition (determined by EDX) across the tribofilm is dominated by amorphous carbon (from decomposed oil) and W as well as S in a 1:2 ratio. (d) The in-situ

formation is also suggested by density functional theory calculations, which suggest that at increasing contact pressure the WS_2 becomes energetically more favorable than WO_3 which has formed in the contact. 64

Figure 20: (a) The HIPIMS sputtered coating is comprised of a W interlayer and a tungsten nitride based nanocrystalline topcoat. The metallic interlayer acts as bond coat and compensates the dissimilar mechanical properties of substrate and coating. Due to the biaxial sample rotation while sputtering (with one cathode) the growth rate fluctuates periodically giving the coating a multilayer-like appearance in transmission electron microscopy (TEM) images. While the actual coating appears to be of nanocrystalline to amorphous structure in images, selected area diffraction (SAED) in (b) reveals its hexagonal δ-WN structure (with a N content of roughly 60 at.-%). (c) The interlayer predominantly grows with a 100 orientation. (d) X-ray diffraction confirms the hexagonal δ-WN structure of the coating on top of the steel substrate and the W interlayer. The overall phase fraction of metallic W was obtained by Rietveld refinement and is in agreement with the amount of W we were expecting from an interlayer of this thickness. Concluding, that the topcoat is free of a metallic phase fraction. 74

Figure 21: The hardness H of the coating did not decrease with the penetration depth ht and was 31 ± 3 GPa, whereas the indentation modulus E was 350 ± 25 GPa. 75

Figure 22: DFT calculations (VASP) demonstrate the increasing formation enthalpy for WN and WO_3 with increasing pressure, whereas the formation enthalpy of WS_2 remains constant, making it energetically more favorable at high pressures. At the same time, the formation enthalpy of WN also highlights why the coating is so beneficial to the formation of WS_2. 75

Figure 23: The long term performance of the coating in combination with the S-

containing lubricant at 100 °C and a contact pressure of 0.5 GPa is excellent. For verification of the results long term tests have been performed with a second Nanovea micro tribometer at another institution. (a) The COF remains at very low levels around 0.05 even after 100 h. (b) Even after 100 h of testing, no wear on the coating can be detected in a radial line scan or with microscopy. It is important to mention that the two areas with reduced height can clearly be linked to preexisting coating and sample defects. As a comparison, for the appearance of a worn coating and to reference the location of the undetectable wear track, an additional track with excessive force was introduced. (c) The ball shows no measureable wear after 100 h of testing as well. .. 76

Figure 24: Influence of the EP additive concentration. (a) Development of the coefficient of friction over time with a steel ball at 100 °C (b) Raman spectra of the corresponding tribofilms (c) comparison of Raman peak intensities according to the position of the (d) measured region 84

Figure 25: Influence of the contact temperature at 3 % EP additive. (a) High temperatures lead to lower friction and (b) stronger C-based signals in Raman spectroscopy..... 85

Figure 26: Influence of the counter body at 3 % EP additive. (a) Si_3N_4 counter bodies lead to very stable runs at low friction. (b) At 100 °C with Si_3N_4 ball, high amounts of carbon are formed. 86

Figure 27: Chemical composition of the tribofilm in a Mo Vs steel contact at 100 °C with 3 % EP additive. (a) Scanning TEM overview of the FIB cross-section (b) chemical composition of a young surface near tribofilm obtained by EELS (c) chemical composition of older tribofilm debris. 89

Figure 28: HR TEM images of the tribofilm (Mo vs. steel, 100 °C, 3 % EP additive). (a) SAED pattern of the debris area (b) HR image of a young tribofilm (c) MoS_2 sheets

formed on top of Mo debris (d) MoS_2 sheets are covered by a layer of residual carbon. 90

Figure 29: Poisoning behavior of the (a) Cr-, (b) Mo-, (c) W-, and (d) Nb- micro-alloyed targets with increasing oxygen contents. The gray shaded areas represent the hysteresis of a non-alloyed Al target. 100

Figure 30: Plasma parameters based on Langmuir measurements: (a) floating potential, (b) ion density, and (c) electron density for gas mixtures in the metallic, transition, and poisoned mode, respectively. 102

Figure 31: (a) Deposition rate depending on the transition metal content of the micro-alloyed targets. (b) SEM top-view of the 5 at.-% W alloyed Al target after a sputtering process in the transition region (especially the Al regions around W particles are sputtered at higher rates, forming characteristic craters around these particles). (c) Light optical microscopy cross-section of a virgin 5 at.-% W alloyed Al target. 103

Figure 32: (a) ERDA obtained TM content within the prepared coating with respect to those of the targets. An ideal relation for the formation is given by the grey solid line. (b) Al:O ratio within the coating. The colored horizontal lines indicate the composition of the undoped alumina coating. 105

Figure 33: GID (XRD) measurements of our coatings in dependence of the chemical target composition, indicated on the right side of the graph. The peak positions of γ-Al_2O_3 are marked. 106

Figure 34: Cross sectional TEM BF images of the interface near region and coating structure. Every panel for each dopant (2 at.-%): (a) pure Al_2O_3, (b) Cr, (d) Mo, (e) W, and (c) Nb also includes an SAED pattern of the crystalline regions in the right upper corner and an overview across the whole sample at the bottom. (f) A line-scan through the 2 at.-% W doped coating (perpendicular to the substrate). 108

Figure 35: Hardness (a) and indentation modulus (c) of our coatings with respect to the target composition and in dependence on the chemical composition within the coating (b) and (d). 110

Figure 36: TEM investigation of the coating. (a) The coating is initially amorphous and exhibits cone-shaped crystalline γ-Al_2O_3 regions. (b) SAED pattern of the coating showing the reflexes of γ-Al_2O_3 and an amorphous fraction. Fourier Transformation (c) of HD TEM images (d) also confirm the nanocrystalline γ-Al_2O_3 structure of the coating. 116

Figure 37: DSC evaluation of the doped coatings, considering the heat flow (a) and mass change (b) of the coating powders. (c) Summary of onset temperatures for the γ- to α-Al_2O_3 transformation of pure and Cr, Mo, Nb, or W doped Al_2O_3 coatings. 118

Figure 38: XRD spectra (4 h long-term data acquisition) of the coating powders from 2 at.-% alloyed targets in their as deposited state (a) and after the DSC annealing up to 1600 °C (b). 119

Figure 39: Stepwise non-ambient XRD measurements from 600 °C to 1200 °C with 2 at.-% target doping. The transformation from γ- to α-Al_2O_3 is clearly visible for undoped Al_2O_3 coatings (a), Mo doped (b), Nb doped (c), and W doped(d) coatings. 121

Figure 40: Highlight I, reaction pathway for the in-situ generation of WS_2..... 124

Figure 41: Highlight II, formation of MoS_2 on metallic Mo under a carbon film, produced by catalytic breaking of hydrocarbon bonds. 125

Figure 42: Highlight III, Al_2O_3 deposition rate increase and poisoning retardation by rebound sputtering with heavy element (W) micro-alloyed Al targets. 126

Figure 43: Highlight IV, significantly delayed γ-Al_2O_3 to α-Al_2O_3 transition due to increased surface area and the solute drag by W-dopants. 127

List of Abbreviations

bcc ..... *body-centered cubic*

bct ..... *body-centered tetragonal*

COF ..... *coefficient of friction*

CVD ..... *chemical vapor deposition*

DC ..... *direct current*

DLC ..... *diamond-like carbon*

EDX ..... *energy-dispersive X-ray spectroscopy*

EELS ..... *electron energy loss spectroscopy*

EP ..... *extreme pressure*

fcc ..... *face-centered cubic*

FIB ..... *focused ion beam*

FWHM ..... *full width at half maximum*

HCBU ..... *high current bunched mode*

HIPIMS ..... *high-power impulse magnetron sputtering*

HR ..... *high-resolution*

LMIG ..... *liquid metal ion gun*

MoDTC ..... *molybdenum dithiocarbamates*

MoDTP ..... *molybdenum dithiophosphates*

PAO 8 ..... *poly-alpha-olefin 8*

PAW ..... *projector augmented plane wave*

PBE ..... *Perdew-Burke-Ernzerhof*

PVD ..... *physical vapor deposition*

RF ..... *radio frequency*

SAED ..... *selected area diffraction*

SEM ..... *scanning electron microscopy*

SIMS ..... *secondary ion mass spectroscopy*

SZM ..... *structure zone model*

TEM ..... *transmission electron microscopy*

TMD ..... *transition metal disulfide*

TMDC ..... *transition metal dichalcogenide*

TOF ..... *time of flight*

UHV ..... *ultra-high vacuum*

VASP ..... *Vienna Ab initio simulation package*

XPS ..... *X-ray photoelectron spectroscopy*

ZDDP ..... *zinc dialkyldithiophosphates*

1 Introduction

Our society has always been shaped by advances in technology and the materials that made new technology possible. It is no coincidence that big sections of our history are named after ancient breakthroughs of material development. A long history in the exploration and research of new bulk materials continued. Although we regularly used composite materials for building (mud and straw to modern concrete), jewelry (gilding) or warfare (e.g. the Mongolian composite bow) it took us until the 20th century to realize that we can also apply this fundamental idea of combining different materials to any other material related issue. In a society, that was increasingly driven by competitive pricing, this meant that expensive materials often could be replaced by combination of much cheaper materials, setting the stage for thin film technology. Especially in the tooling industry, the application of hard coatings yielded a significant increase in tool service life and work piece quality. There is another obvious benefit of coating technology, other than the avoidance of expensive materials. The application of hard and durable bulk materials often involves high expenses for shaping, which now can be avoided by selecting an easy-to-shape material (like steel), forming it, hardening it and subsequently coating it with ceramic materials (like TiN) in order to achieve a high quality component.

Thin film technology was also supported by the technology revolution of microelectronics and their untamable drive for miniaturization. Soon, the application of thin films in microelectronics became an additional pillar of thin film technology, particularly physical vapor deposition (PVD). PVD made it possible to deposit thin films of a wide range of materials with relatively low effort. Like all other materials, thin films can interact with surrounding material and are affected by thermal loads during applications that can induce phase transformations. While phase transformations have always been of high interest to thin film technology (due to the nucleation and growth during deposition), it is apparent that controlling or inducing phase transformations can be essential for some applications.

Nowadays, PVD has reached almost every part of our life, although we often do not realize or recognize it. It is a key component in achieving a sustainable industry and essential in conserving resources and saving energy. One sector that has already benefitted from the application of coated tool is the transportation sector. Nevertheless, its main inefficiency lies not in the production of vehicles, but rather in the produced vehicles themselves [1-4]. Thanks to political and social pressure, the goal of car manufacturers shifted from just producing high quality as cheap as possible to reducing car's emissions and providing a product with a minimal ecological impact. To achieve this goal it is essential to reduce the high energy loss due to friction and maximize service time that is limited due to wear. While friction and mild wear are usually addressed by lubrication, it is not uncommon to protect highly strained surfaces with coatings. One of these coatings is diamond-like carbon (DLC) [5-7], which has taken the automotive industry by storm. Unfortunately, many coatings do not interact with modern additivated oils (as they require ferrous surfaces), or in case of some DLC coatings, might even suffer from the application of engine oils that contain friction modifiers or extreme pressure (EP) additives [8, 9]. In addition, many conventional

lubricants are also linked to increasing environmental problems and an endeavor towards green lubricants is of high importance [10-12]. Chapters 4 and 5 will prove a coating-lubricant synergy that is capable to eliminated wear and reduce friction by the formation of 2D-materials. In a first step, a phase transformation (that is induced by a chemical alteration) produces an amorphous product. In a second (this time structural) phase transformation, this amorphous product self-assembles to form lubricating crystalline structures. This tribochemical reaction addresses both, the issues of wear protection and low friction. It suggests an alternative take to conventional lubrication strategies via a chemical reaction and phase transformation at the coating-lubricant interface.

Modern transportation also relies heavily on the aerospace sector, where increasing passenger numbers and high oil prices highlight the need for maximum efficiency. Composite materials are being implemented to reduce weight. Passenger capacity is being increased. At the same time engines need to improve while becoming more sustainable, eco-friendly and less noisy. Two substantial contributors to recent jet engine advances are the realization of geared turbo fans and the implementation of novel alloys (like γ-TiAl) [13]. These novel lightweight alloys, based are mechanically capable to replace heavy Ni-base super alloys [13-15], but unfortunately suffer from sever oxidation at temperatures above 600 °C. Therefore, the oxidation protection for such alloys is essential to suppress oxygen diffusion into the base material. One coating material that is known for its capabilities as a diffusion- and at the same time thermal barrier coating is alumina [16-19]. Due to the temperature-sensitivity of many modern machine component materials, the deposition of alumina can only be achieved with PVD. In this low temperature regime of PVD, alumina can only be deposited in its metastable γ-Al_2O_3 structure, which transforms to stable α-Al_2O_3 at temperatures around 1000 °C. This transformation includes a densification of alumina due to a volume decrease, leading to cracking and degrading its protective effect. Therefore, the

oxidation protection arises from a delay of a phase transformation and chapter 7 will outline, how this can be achieved by doping with transition metals. The dopants can, at the same time (in chapter 6), address the problem of low deposition rates and instabilities during the deposition process of PVD alumina coatings.

2 Theoretical Background

The following chapter will provide a better understanding of phase transformations in solid materials as well as the conditions that arise in a tribological contact. It should also give some details on the background of the involved materials and in which applications they are most relevant.

2.1 Phase Transformations

The development of coatings always requires a careful consideration of the thermodynamic stability of the deposited structures as well as their phase transformations. Phase transformations occur when a system is not in its thermodynamic equilibrium state and do not necessarily require a change of the state of matter. They can also describe structural, magnetic, ordering or many other changes. There are many classification methods for phase transformations, building on different criteria. One example is the classification by *Ehrenfest*, assigning any phase transformation an order n according to the discontinuance of derivatives of the free energy [20].

The easiest way to gain information about phase transitions in materials are phase diagrams, giving information in dependence on temperature and chemical composition. Phase diagrams always display materials in an equilibrium state. In many modern materials, especially in PVD coatings with extreme cooling rates at the substrate, the

materials' structures differ significantly from the equilibrium state and further investigations into metastable or intermediate phases are necessary.

2.1.1 Phase Stability

There are many factors influencing the stability of a phase, with the dominating factors being chemical composition, temperature, shear and pressure. The best tool to describe stability is the Gibbs free energy, G, defined as

$$G = H - T * S \tag{2.1}$$

with H being the enthalpy, T the absolute temperature and S the entropy. It is an extensive property, meaning that a system can be subdivided into any number of subsystems and the overall Gibbs free energy would be the sum of all subsystems. The Gibbs free energy also gives insight into any reaction or transformation, as they occur self-driven if the difference in Gibbs free energy between the final and the initial state is negative:

$$\Delta G = G_{final} - G_{initial} \tag{2.2}$$

Any phase is considered stable, when its Gibbs free energy reaches a global minimum. As shown in **Figure 1**, materials can also have atomic arrangements that differ from the stable state, yet pose a local minimum. These arrangements are considered as metastable phases, whose transformation to the stable phase are kinetically hindered by an energetic barrier, called activation energy. A coating that might be deposited in its metastable form, will during application often be subjected to severe thermal stress (consider cutting tools or thermal barrier coatings). This energy input can easily surpass the activation energy and trigger a transformation to the stable form.

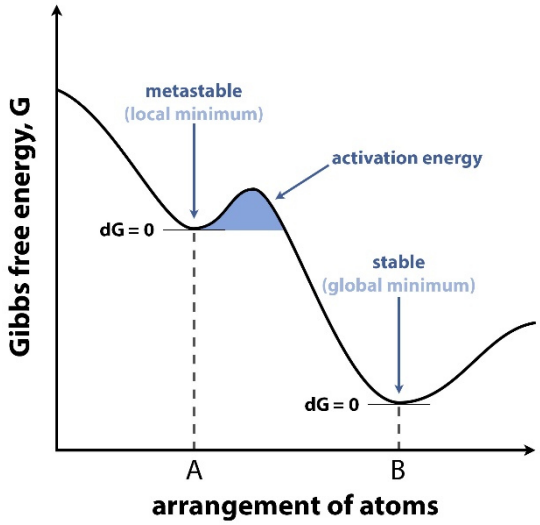

Figure 1: Illustration of the Gibbs free energy of a material (constant temperature and chemical composition) with respect to the arrangement of its atoms (adapted from [21]).

When we mix two chemically different systems, as in solid solutions or compounds, we have to consider the free energy of mixing, ΔG_{mix}, which accounts for the mixing enthalpy ΔH_{mix}, as well as the mixing entropy ΔS_{mix}. The mixing entropy is always positive as the number of possible microscopic configurations increases and contributes to the stabilization of the mixture. The mixing enthalpy, however, depends on the bond energy between the species A and B as well as the A-A and B-B bonds, respectively. Stronger A-B bonds ($\Delta H_{mix} < 0$) favor the formation of a mixture ($\Delta G_{mix} < 0$). There are four possible outcomes for the Gibbs free energy of mixing of an ideal solution, drafted in **Figure 2**.

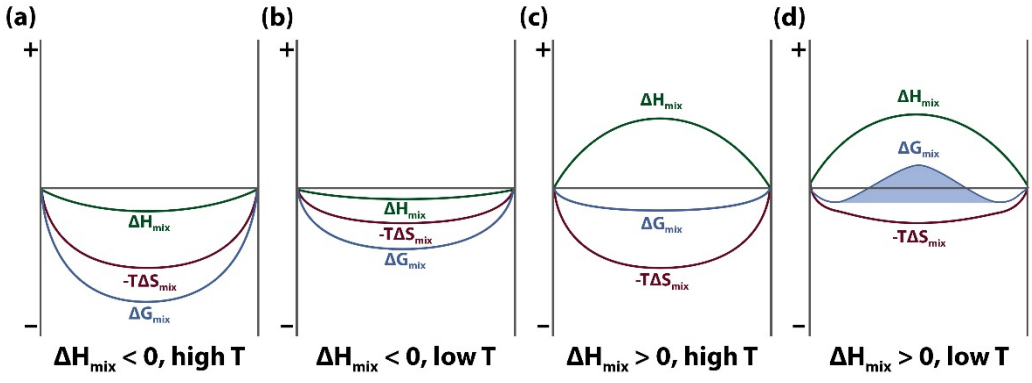

Figure 2: Effect of the mixing enthalpy and temperature on the Gibbs free energy of mixing, showing the formation of a miscibility gap with a positive mixing enthalpy at low temperatures (adapted from [21]).

Figure 2a and **b** show ΔG_{mix} for a negative (exothermal) mixing enthalpy at high and low temperatures, respectively. In this case the ΔG_{mix} is negative over the whole concentration range and there are no solubility limits for a solid solution. If the ΔH_{mix} is positive on the other side, the solubility is highly dependent on the temperature. At high temperatures (in **Figure 2c**) the entropy term outweighs the ΔH_{mix} and a solution is possible. However, if the temperature decreases (in **Figure 2d**) the ΔH_{mix} ascends over the entropy term leading to the highlighted region, called a miscibility gap, where the ΔG_{mix} becomes positive and therefore not stable. At this place, it is necessary to mention that if the concentration of either one of the components A or B converges to 0, the number of possible microscopic configuration increases rapidly, leading to an initial almost vertical slope of $-T\Delta S_{mix}$. The slope of the ΔH_{mix} on the other hand tends to a finite value, resulting in the characteristic shape of ΔG_{mix} in **Figure 2d**. As a result, ΔG_{mix} initially always decreases and facilitates the addition of small solute amounts (above 0 K) [21]. In the miscibility gap between the minima of ΔG_{mix}, the instability leads to a decomposition to material A and B [20-22].

2.1.2 Nucleation and Growth

Whenever a material experiences a phase transformation, whether it is the deposition of sputtered atoms at the substrate, a solidification of metal, or a solid-state transformation, the transformation occurs locally by a nucleation and growth mechanism.

The nucleation process in a solidification occurs when a driving force (ΔG) due to a temperature decrease, leads to a local accumulation of atoms, arranging in a crystal structure. The nucleus represents a new phase in the system and therefore has an interphase to its surrounding. However, the generation of this new surface requires energy. While the ΔG for the bulk formation is negative, the energy requirement by the surface is higher and leads to an overall instability of the nucleus until a threshold-size is reached and growth occurs. In this context, the nucleation of crystalline phases often requires an overshooting of the transformation temperature. Nucleation can occur homogenously (spontaneous without preferential nucleation sights) or heterogeneously at preferential sites like impurities or defects.

In physical vapor deposition, nucleation occurs at the substrate surface, whereat defects of any kind (steps, dislocations, grain boundaries and many more) are preferential nucleation sites [23]. Although overcooling generally helps with nucleation, the high cooling rates of PVD can lead to a very limited surface mobility of adatoms, having the opposite effect by preventing the nuclei from growing. Due to the continuous flux of species towards the substrate, this mechanism leads to amorphous thin films and can be prevented by increasing surface mobility (e.g. by heating). Another effect that can suppress nucleation and growth will be visible in chapter 6, where dopants (of a concentration inside a miscibility gap) are introduced into the coating. While that would simply lead to a decomposition into two stable phases at higher temperatures, the high cooling rate of PVD can force them into a metastable solid solution, or in case of very high crystal lattice differences into an amorphous mixture.

2.1.3 Solid-State Phase Transformations

Solid-state transformations, like the γ- to α-Al_2O_3 transformation, do not occur simultaneously across the whole material. Many of them (in particular most structural phase transformations) also require nucleation and subsequent growth that moves the transformation interface through the initial material. Solid-state transformations often rely on heterogeneous nucleation at crystal defects, interfaces or grain boundaries [24]. While there are many different solid-state transformations (e.g. eutectic reaction, precipitation, superconductivity), which occur for a variety of reasons (mostly reliant on temperature), this section focuses on polymorphic phase transformations. They are structural solid-state transformations without a chemical change, that imply a rearrangement of constituents, which can occur displacive (diffusionless) or reconstructive (diffusional) [20, 22, 25].

Displacive phase transformations, as the name suggests, only involve a displacement (or shear) of the atoms without any rearrangement and atoms remain in contact with the same neighbors. The martensitic transformation of face-centered cubic (fcc) austenite (hexagonal close-packed) to body-centered tetragonal (bct) martensite (cubic close-packed) is a good example for this type of reaction, which due to its high industrial relevance has been studied intensively. It is a so-called 'military' transformation, as atoms at the transformation interface are displaced in a coordinated fashion (in oppose to the 'civilian' diffusionless massive transformation). Military transformations always induce a shape change (shear) [20, 26]. Because no diffusion is involved (requires activation energy), martensitic-type transformation can also occur at very low temperatures and grow at excessive speeds of 1000 $m \cdot s^{-1}$ [26]. Martensitic type of reactions are also very common in ceramic materials of thin film technology.

Reconstructive phase transformations are always of a 'civilian' type and due to the high activation energy (required for diffusion), they are associated with high

temperatures. The necessary long-range diffusion also leads to a slower advance of the transition interface. Reconstructive transformations are considered to be sluggish and therefore the high temperature polymorph can often be cooled down to room temperature without further transformations. Typical diffusional phase transformations would be decompositions and eutectic reactions. In relation to this work, the transformation of γ- to α-Al_2O_3 would represent a reconstructive transformation as the densification requires long-range diffusion.

2.1.4 Pressure-Induced Solid-state Phase Transformations

Le Chatelier's principle states that if we put an equilibrium system under constraint by e.g. temperature changes or adding pressure, it will adjust in a way to minimize its energy. If we put vapors under pressure, they will (depending on the temperature and the Joule-Thompson-coefficient) condense to a liquid in order to avoid the implemented stress. As stated before, phase transformations require a driving force that allow the reduction of the system energy. While the most common phase transformations are based on temperature changes, they can also be triggered by pressure. At the same time, additional pressure can shift the transformation temperature of thermally induced phase transitions. To give an example of the magnitude of this influence of pressure, the transition temperature from γ- to α-Al_2O_3 can be lowered by more than 50 % to around 500 °C by applying a pressure of 1 GPa [27]. Especially electronic phase transformations can be sensitive to pressure, but considering the structural phase transformation, many compounds and metals (e.g. also titanium nitride and tungsten nitride) can assume high-pressure modifications. In general, the high pressure polymorphs are closer-packed and denser than their ambient pressure phases [28, 29]. Under high pressure many fcc NaCl-type structures will transform to a body centered cubic (bcc) CsCl-type [29]. This transformation is also expected for a common coating material like TiN [30].

2.2 From Friction to Tribofilm Formation

A tribofilm (also called boundary lubrication film) is a thin reaction layer that forms on surfaces under tribological shear and contact stresses. They are not restricted to lubricated contacts and represent a major field of tribology. But, before addressing the formation of these reaction films, it is important to cover the underlying basics.

Tribology is the science and engineering of interacting surfaces in relative motion [31]. The word tribology itself derives from the Greek word "tribo" (rub) and "-logia" (study of). Classic tribology addresses the optimization and interaction of wear, friction and lubrication, with many new additional topics being added in modern tribology. It is a very interdisciplinary field of research, involving engineering, physics, chemistry, materials science, biology, mathematics and computational science.

2.2.1 Tribology: Friction, Wear and Lubrication

Looking back in history, friction and wear have always been addressed by trial and error. The first scientific approach by *da Vinci* in 1493 was never published and it took until the late 17th century until the scientific approach was picked up by *Amontons* [32]. He (*Amontons)* defined two laws of friction that were later on completed by *Coulomb* with a third law:

- Friction is independent of the apparent contact area.
- The frictional force is directly proportional to the normal load, via the dimensionless coefficient of friction (COF).
- Dynamic friction is independent of the sliding speed (for dry contacts, within certain limitations).

While those laws are the basis of tribology, we have to acknowledge that they are not sufficient to describe many modern tribological systems [33]. While the COF was

initially viewed as a material property, many studies have shown that friction can in reality only be described by regarding the COF as a property of the complete tribological system and that the consolidation to simple material pairings (e.g. steel on steel) is not accurate enough.

The conception of tribology as an independent branch of science (as well as the name) were molded in 1966 by *Jost* in his important report, highlighting the enormous costs of friction, wear and corrosion to the economy [31]. This report sparked decades of research, that nowadays (a century of sustainability and environmental friendliness) is probably as relevant as never before [4]. *Holmberg* and *Erdemir* gave an extensive survey of the impact of friction and wear on our society, highlighting an extreme potential to increase efficiency [2, 3].

When we talk about friction, we have to differentiate between several types of friction: internal friction (force against deformation on an atomic scale), skin friction (resistance of fluid motion across a surface), fluid friction (between molecules of a viscous fluid), lubricated friction and dry friction. In the following section, I want to expand on the latter two, as they both are of high significance to PVD coatings in general, and lubricated friction to this thesis in particular.

Dry friction covers static friction, kinetic friction and rolling friction. Most of the fundamentals of dry friction were already discussed above, but it is also important to discuss what the source of the frictional force is. Surfaces are never perfectly smooth (down to the nanometer scale) and if they are in contact with each other, the contact can be rather described as the sum of interacting single asperities. Exactly these single asperities are the source of friction as they undergo elastic and plastic deformations as well as break (or rupture) deformations, leading to the dissipation of energy. Due to the load force and the friction force being transferred only by the few asperities in contact, the contact pressure is locally much higher than the geometrical calculated

contact pressure. As a result, real conditions (pressure & temperature) in the single asperity contact can vary significantly from the surrounding material [34]. There are models and studies concerning the single asperity contact [35, 36], portraying progress in simulating the deformation mechanism and the overall dissipation of energy in the single asperities, but e.g. the localized temperature and energy spikes are still widely unknown.

In lubricated friction, the principles that are the origin of the friction are similar, but we have to take into account that the solid surfaces are separated by a lubricating fluid. There are two fundamental approaches on the generation of fluid films: In hydrostatic lubrication, the lubricating film between the surfaces is sustained by applying pressure to a lubricant reservoir and delivering the pressurized lubricant directly into the contact. In the second approach, hydrodynamic lubrication, the motion of the lubricated surfaces creates a frictional viscous resistance that pressurizes the lubricant in the contact, carrying the load. This complex hydrodynamic theory is based on the Reynolds equation [37] and the lubricating properties are highly dependent on the lubricant viscosity (therefor also temperature dependent), sliding speed and load. This dependence can best be described by Stribeck curves [38]. An exemplary Stribeck curve is displayed in **Figure 3**, showing the dependence of the COF on sliding speed and temperature (viscosity). It shows that hydrodynamic friction can be subdivided into three sections:

- **Hydrodynamic lubrication**, in its proper form: The surfaces are fully separated by the fluid film and the coefficient of friction is defined by fluid friction. The design of the contacts (formal, nonconformal) and techniques like surface texturing [39] can benefit the hydrodynamic regime as well.

- **Mixed lubrication**, occurs if the generated hydrodynamic pressure is not high enough to completely separate the two surfaces. Initially the contact between single asperities is low, but with decreasing sliding speed (and therefore decreasing hydrodynamic pressure) the contact between single asperities increases.

- **Boundary lubrication**: At high loads and/or low sliding speeds, the asperity contact has a significantly higher bearing on the COF than the hydrodynamic effect. As a result of the single asperity contact, localized temperature and pressure spikes occur [40]. These conditions and the presence of lubricating molecules are the perfect base for chemical alterations and the formation of tribofilms. These mechanisms will further be discussed in the seperate section 2.2.2 about tribofilm formation.

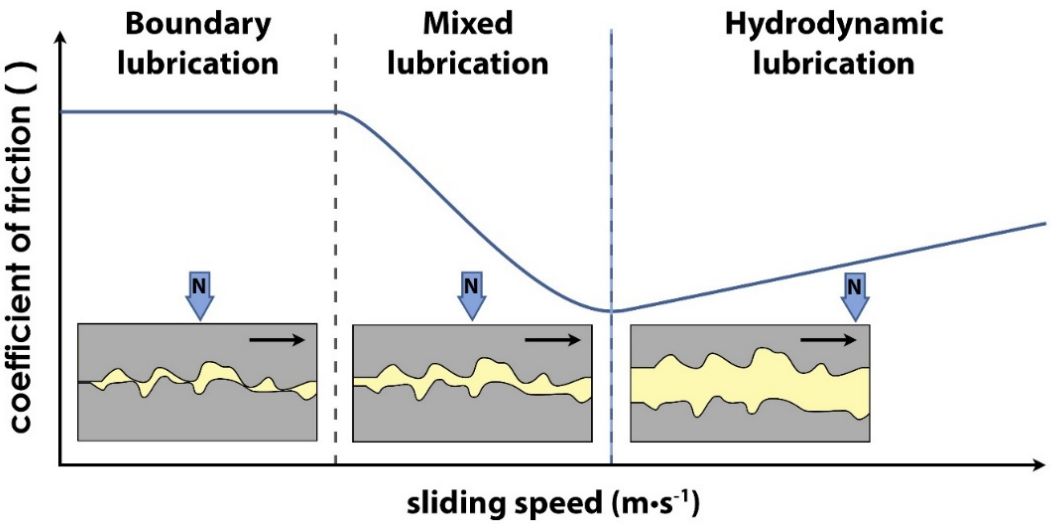

Figure 3: Stribeck curve of a lubricated contact. The contact schematics highlight the separation of the surfaces by a lubricant film and defines three different regimes of hydrodynamic lubrication.

Although there is no direct correlation, whenever we talk about friction, we also have to talk about wear. Wear, like friction, is a system property and depends on parameters like loading type, motion, temperature, lubrication and the contacting materials' mechanical properties. On the materials side, the predominant influencing properties are hardness, roughness, fracture toughness, thermal stability and possible chemical interactions (oxidation, tribochemical reactions). Sliding surfaces in contact always result in material removal that can be categorized into four major wear mechanisms, depicted in **Figure 4** [41, 42]:

- **Adhesive wear** can generally be described as the transfer of wear debris and material from one surface to another. Two pieces of the same material with perfect conforming smooth surfaces (on an atomic level) would, if brought together in a perfect oxygen free vacuum, sick together and form bonds that are just as strong as the rest of the material [41]. This mechanism is also commercially applied in cold welding of metals [43]. During single asperity contact, especially when a high degree of deformation is involved, material mixing and cold welding (that leads to the transfer of material during detachment) can occur (**Figure 4a**) [44]. Adhesive wear is promoted, if the bonds between material A and material B are stronger than within material B. Adhesive wear does not require a shearing load component, but additional shearing would lead to the formation of build-up on material A. Adhesive wear and build-up are typical problems in tools for dry cutting [45], that are addressed with protective coatings [46-50].

- **Abrasive wear** arises, when a hard surface with pronounced asperities slides against a softer surface, leading to high wear of the latter one. Abrasive wear is promoted by rough hard surfaces (like they often occur in PVD coatings with

insufficient surface quality) and can be identified easily due to the formation of characteristic grooves on the softer material. Additionally, we can differentiate between three mechanisms in abrasive wear that lead to different surface damage: plowing, cutting and fragmentation. While in blowing, the material is displaced to the side and does not involve direct material removal, cutting leads to much higher wear rates as material is removed from the surface. Fragmentation occurs, when in addition to cutting wear, the worn surface is damaged by localized fractures, leading to additional material removal. Abrasive wear does not necessarily need to be initiated by hard material protuberances. The abrasive mechanism can also be initiated by hard wear debris, tribochemical reaction products or contaminations (three-body wear), as shown in **Figure 4b** [41].

- **Fatigue**: Surface fatigue arises essentially in cyclically loaded systems like ball bearings. Fatigue wear occurs when micro-cracks are induced and (horizontal) crack growth leads to the detachment of particles (**Figure 4c**). The visual appearance is often in form of pitting and the detached particles can potentially lead to three-body wear.

- **Chemical effects**: The number of possible chemical effects is vast. I will divide them into three groups as outlined in **Figure 4d**. Interaction with the surrounding gases can lead to the formation of compounds. One obvious example would be oxidative attack that often leads to the formation of a mechanically poor oxide scale, which is easily worn away (a common problem in fretting) [51]. Oxidative particles can in some cases act as an abrasive third body, but interactions with gas can sometimes lead to the formation of lubricating compounds [52-54]. Similar behaviors can also be noticed in

lubricated contacts with corrosive lubricants or media (e.g. tribocorrosion) and beneficial chemical interactions as further described in sections 2.2.2 and 2.3.2. Chemical interaction between two surfaces in a dry tribocontact are rather exotic, but do exist (e.g. with the intend to lower friction by formation of WS_2 [55, 56]).

The options to counteract wear and friction are almost limitless and in most cases, the limiting factors are feasibility and costs. Possible approaches include topics like contact design, material selection, adjusting material properties themselves, lubrication, lubricant additives, hard facings and coatings. Since wear protection is the beating heart of thin film technology the number of publications for a search containing 'wear' and 'coating' increased to a staggering 35 000 publications since 1970.

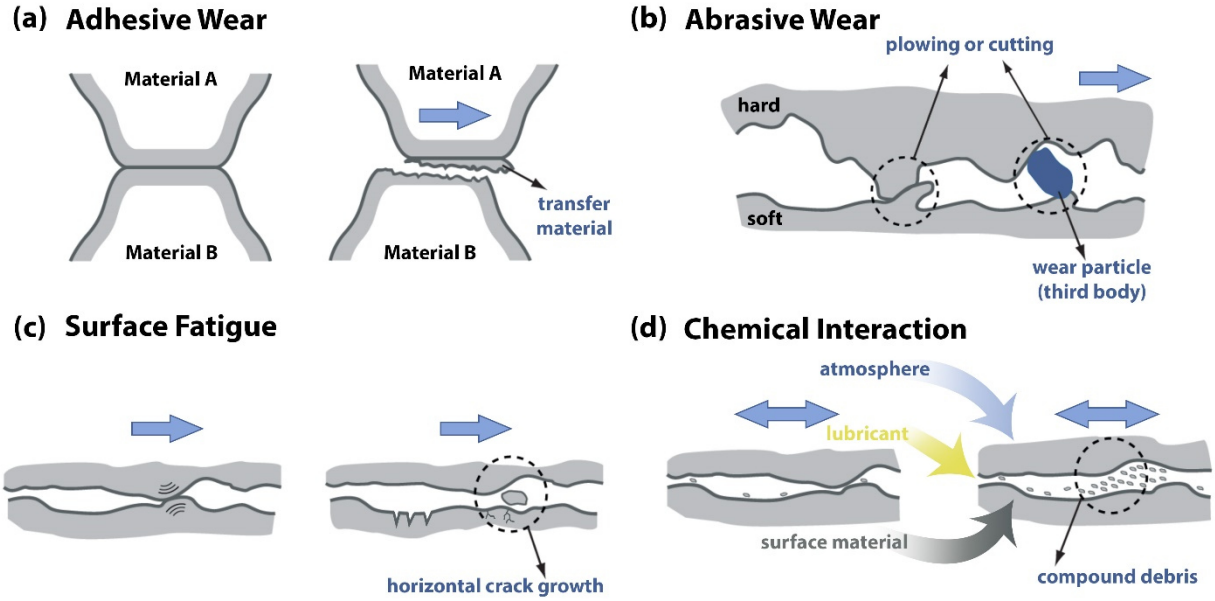

Figure 4: Schematics of the four wear mechanisms, highlighting the interaction and influences of surfaces (adapted from [57]).

We therefore want to focus on low friction coatings (most of them address wear protection too, anyway). For many applications, the easiest solution is simple lubrication, but when temperatures, contact pressures, cleanliness requirements or precision goals do not allow their use, coatings are the method of choice. This means that most applications for PVD coatings also involve elevated temperatures. For lower to medium range temperatures, coatings based on MoS_2 and WS_2 (as described in section 2.3.2), as well as diamond-like carbon coatings [5, 49, 58] are common. In medium to high temperatures the formation of oxides becomes unavoidable in applications, therefore many coatings rely on the formation of self-lubricating oxides (based on easy shear planes) like V_2O_5 [59], TiO_2 or MoO_3 [52, 60] on the surface of transition metal nitride coatings [61]. The relationship between the crystal-chemical and tribological properties of potential oxides for high temperature lubrication was given by *Erdemir* et al. [62]. Another alternative for high temperatures are hard coatings, containing soft metals like Ag, capable of diffusing out of the coating into the contact where they unfold their lubricating effect. Other metals like Pt and Au have been investigated due to their low hardness, good lubricating properties at high temperatures and high oxidation resistance as well [63, 64]. In an effort to create coatings that adapt to the temperature and environmental conditions, *Voevodin* et al. have developed complex (so called) chameleon coatings [65] that combine all of those approaches.

Conventionally, when we talk about tribofilms we think of boundary lubrication. However, all coating strategies for low friction are united by the effort to create some sort of top-layer with easy shear planes that reduce friction. Even if these layers might be extremely thin, they are altered in structure and sometimes in chemical composition and can therefor be considered as tribofilms or reaction layers.

2.2.2 Tribofilms and their Formation

The origin of tribofilms lies in the discovery of reaction layers in boundary lubricated metal contacts by *Bowden* in 1945 [66]. This was also the time, when extreme pressure (EP) additives to reduce wear in heavily loaded contacts came around. Initially they were based on lead soaps or fatty acids but soon were replace by S- and P-based organic compounds.

In boundary lubrication, interacting surfaces cannot be separated by a continuous oil film anymore. Instead, separation can be achieved by the formation of a tribofilm, highlighting the importance of oil additives (and in some cases coatings) [67]. While tribofilms can have a beneficial effect on the COF (like in chapter 4 and 5), their main task is protection against wear. The goal is, to provide an interface material that keeps wear and degradation away from the actual surface material. Therefore, it is essential that the tribofilm is formed at higher rates, than it is worn away. In return, the oil additives that are used for tribofilm formation are depleted from the oil instead of surface material being worn. The functionality of those additives, their formation and stability are often very complex and highly sensitive to the underlying wear mechanism, contact pressures [68], oxidation, materials [69] and temperature [68, 70].

Additives for tribofilm formation can be classified in different ways: According to their intended contact pressure, they can be subdivided into anti-wear additives (low and medium loads) and EP additives for high loads. Another classification criteria are the chemical interactions the additives are based on. They can *(i)* react with the surface material (like many S- or Cl-based additive compounds), or *(ii)* they can form tribofilms by thermal or oxidative triggered reactions without sacrificial surface material (although it still might have an catalytic influence) [67]. While the EP additives investigated in this work are of the first type, the commercially most successful EP additives so far belong to the second group and are called

zinc dialkyldithiophosphates (ZDDP), molybdenum dithiocarbamates (MoDTC) and molybdenum dithiophosphates (MoDTP).

ZDDP was first introduced to the market as a corrosion inhibitor in 1941 and only later, in the 50s, its potential as anti-wear additive was discovered. The effect of ZDDP starts to unfold in its solute form, where it deactivates metal surfaces and reacts with radicals to inhibit oxidation. On rubbing iron surfaces it can form tribofilms, based on ortho- and pyrophosphates that provide a protective effect in mild wear. In addition, it can also form metal sulfides and 'digest' iron oxide based abrasive particles [71-73]. The big downside to ZDDP are environmental concerns and its damaging interaction with catalysts in the exhaust treatment of internal combustion engines [74]. A potential replacement for ZDDP are 2D layered compounds like MoS_2 or WS_2 [75]. MoS_2 has already been used as friction modifier in combination with ZDDP [76] and is usually generated in the contact by decomposition of the two anti-wear additives MoDTC [77] and MoDPT [78]. In order to reduce pollutive additives (that also require treatment of waste oil), the possibility to replace them by direct addition of MoS_2 or WS_2 nanoparticles is investigated [10, 75, 79-84]. Their sulfide form (MoS_2 is found as a natural mineral) is chemically very stable and does not pose a threat to the environment (or catalysts).

Long-term studies on hazardous behavior of nanoparticles are not yet available, but their dangerous effects have already been uncovered [85-87]. In addition, the expense to produce them and keep them suspended in the lubricant is relatively high. Dispersants can also reduce the effectiveness of the nanoparticles [81]. While MoS_2 and WS_2 can also be introduced by coatings that contain their particles of them [88], this work focuses on an in-situ generation between the lubricant and a reactive coating. This potentially allows the formation of MoS_2 or WS_2 tribofilms with environmental-friendly green additives [12, 89], that are much needed at present [90].

Erdemir et al. gave a completely different approach on protective low friction tribofilms in 2016, reporting on Cu-doped molybdenum nitride coatings that allow the catalytic breakdown of lubricating hydrocarbons. As a result of fragment recombination, a graphite like tribofilm as well as onion-like carbon particles were formed that provided low friction and eliminated wear [91]. Based on these results, other materials have demonstrated similar behaviors [92, 93]. Chapter 5 will show that the formation can also occur in much simpler systems.

2.3 Material Systems

While the introductions to the following chapters will provide a short application-relevant presentation of all used materials, this section aims to provide a more fundamental and widespread background to the applied materials.

2.3.1 Tungsten Nitride

Transition metal nitrides are the workhorse of the PVD coating industry. However, people usually talk about titanium nitride (and its derivatives) or maybe chromium or molybdenum nitride [94, 95]. Despite promising mechanical properties, chemical stability and a high electrical conductivity, tungsten nitride thin films on the other hand are rather rare and relatively unexplored [96]. Due to their electric conductivity and low interaction with copper, tungsten nitride films attracted the attention of the microelectronics industry [97-99]. This focus on electronic properties leaves the structure-property relationship and the phase development during deposition widely unknown.

The W-N system has two main phases: γ-W_2N (a NaCl-type high temperature phase with 30-50 at.-% N) and δ-WN (stable below 1250 °C, hexagonal WC-type). However, there are also reports about cubic WN, cubic W_3N_2, hexagonal W_2N, hexagonal W_5N_4, hexagonal W_5N_8, rhombohedral W_7N_6 and a hexagonal WN type with 67 at.-% N. Tungsten nitride can obviously crystallize with a wide range of anion to cation ratios and is highly sensitive to deposition conditions. The most common phase in tungsten nitride PVD coatings is the γ-W_2N phase, although (in comparison to other phases) its tendencies to form amorphous thin films and the formation of metallic phases at low oxygen contents limit their application as hard coatings. Tungsten nitride coatings (in dependence on the exact chemical composition) decompose around 1000 °C and lead to the formation of a highly porous W-enriched phase. Exactly this instability is of high importance in chapter 4 as it, in comparison to metallic W, facilitates a tribochemical reaction due to the weaker bonding and less stable structure.

2.3.2 Transition Metal Dichalcogenides

Two dimensional materials have experienced a huge leap forward since the first isolation of graphene in 2004 [100]. A single layer of graphene with a thickness of 1 atom is flexible, transparent, stronger than steel and more conductive than copper. It was not long until scientists realized that there are more 2D materials, shedding light onto transition metal dichalcogenides (TMDC). Their structure (**Figure 5**) can simply be described as a single layer of transition metal atoms, sandwiched between two layers of chalcogen atoms (S, Se, Te). The most prominent of them are the two transition metal disulfides (TMD) MoS_2 and WS_2. These disulfides possess a unique combination of interesting, structural [101], chemical [102], electronic [103-106], optical [107] and thermal [108, 109] properties. Their properties are highly dependent on their structure [110], arrangement [111, 112], and composition [105, 113-119].

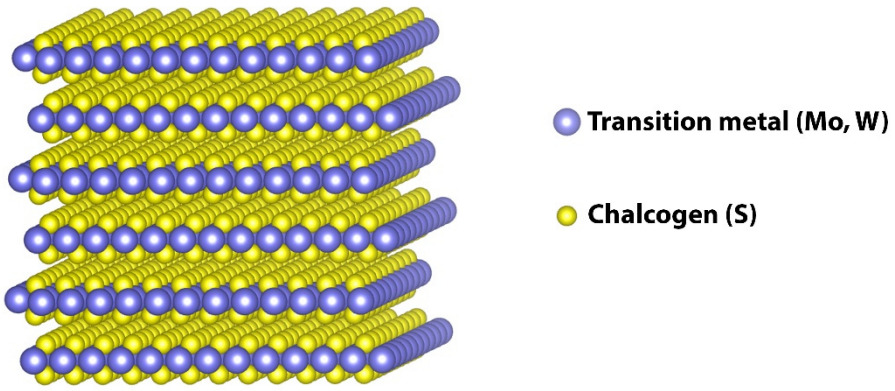

Figure 5: Symbolic S-Me-S sandwich structure of the TMDs [120].

While the interest in afore mentioned properties is relatively new, TMD's mechanical properties have long marked them as excellent solid lubricants. They provide an easy-shear plane between the stacked individual S-Me-S sandwiches that are mainly bound by weak van-der-Waals forces, allowing for exceptionally low coefficients of friction [121-123]. To estimate the lubricity of such lamellar structures, the interlayer-to-intralayer bond length ratio can provide some insight. It has been reported that the greater this ratio is, the lower the interlayer bond strength, leading to high lubricity (MoS_2 has a ratio of 1.5) [41, 124, 125]. MoS_2, probably the most used TMD, delivers reliable lubrication up to 350 °C and can withstand oxidizing atmospheres. The only major downside to MoS_2 is its sensibility to humidity, leading to a drastic deterioration of its lubricating effects [126]. While it was initially suspected that this is the result of oxidation, recent studies have demonstrated that this is most likely due to an adsorption at the sliding interface [127].

Tungsten disulfide, although very similar in structure and properties, allows for low friction up to even higher temperatures of 590 °C in air and 800 °C in Ar. In comparison to MoS_2, WS_2 is less sensitive to humidity and has a higher load bearing capability.

Aside from their application as dry lubricants, these two materials have been heavily investigated for use as additives in oil based lubricants. As already mentioned, they can be formed in-situ by organic precursors under sliding conditions or added as nanoparticles to form lubricating tribofilms [80, 82-84].

TMDs can also be applied as lubricating coatings with a wide range of deposition methods [128-133], sputtering being the most widely used of them. Although sputtered coatings are initially amorphous, they can self-assemble under sliding to form the characteristic low friction sandwich structure [134]. Sputtered MoS_2 thin films usually produce a coefficient of friction around 0.05 (in dry atmosphere), but in highly pure oxygen free stoichiometric films can achieve coefficients of friction as low as 0.01 [122]. Unfortunately, due to the easy delamination of sheets, those coatings suffer from high wear. To overcome wear problems, the common approach is to dope the TMD with predominantly C, but in some cases, other transition metals as well [130, 135, 136]. Due to temperature-tolerance and exceptionally low friction in vacuum TMD thin films had great success in aerospace engineering.

2.3.3 Alumina and Alumina Thin Films

There is hardly any material that has been utilized by mankind for such a long time, yet still holds so many unanswered questions as aluminum oxide [137, 138]. Even today, there is some level of uncertainty to many of its metastable phases and over time it collected nearly as many trivial names, ranging from the most common *alumina* to *aloxide*, *aloxite* or *alundum*. Its first accounted utilization (in form of aluminous clays) was in 5000 BC Mesopotamia. Later on (around 2000 BC), Babylonians and Egyptians would, in addition to pottery, use it in chemicals and medicines as well. For a long time, humans would also treasure its gem-quality crystals, rubies (Cr impurities) and sapphires (mainly Fe or Ti impurities), without knowing the connection. It took until 1798 for a first accurate description of an Al_2O_3 mineral, to be given by *Charles Greville*

in the *Philosophical Transactions, of the Royal Society of London*. He called his discovery *corundum*, derived from the native Indian name of the stone.

The production of Al_2O_3 relies on *bauxite*, a rock that was discovered in Baux, France and is often mistaken for a mineral. To be correct, it is a sedimentary rock that contains economically recoverable amounts of the Al bearing minerals *gibbsite*, *boehemite* and *diaspore* [139]. Its quality is mainly defined by an as low as possible fraction of accompanying iron oxide, titanium dioxide and silicon dioxide. Australia and Brazil possess the largest deposits of high quality bauxite, covering most of the world's needs (e.g. the USA import up to 99 % of their demand). The refinement process, called the Bayer process, was one of chemistry's big success stories. It is a selective solution of alumina in NaOH and a subsequent precipitation as aluminum hydroxide ($Al(OH)_3$), which can be calcined to form pure Al_2O_3. Alumina is the inorganic chemical with the highest production volume and is in use across almost all branches of industry ranging from cosmetics, medicine and food processing all the way to ceramics, electronics and even fracking. Despite, the vast amount of applications, almost 90 % of its production is electrolytically converted to metallic aluminum in the Hall-Héroult process [139].

Alumina has only one stable morphology: the α-Al_2O_3 corundum form, but many metastable polymorhs called transition aluminas. They can be devided into two groups with different anion arrangement. A group with face center cubic arranged oxygen atoms includes γ- (cubic), η- (cubic), θ- (monoclinic) and δ- (either tetragonal or orthorhombic) alumina, while the hexagonal close-packed oxygen arrangement represents κ- (orthorhombic), χ- (hexagonal) and the stable α- (trigonal) alumina [137].

The formation of the individual polymorphs is highly dependant on the educts they derive from and the production conditions. This does not only define the Al_2O_3 product, but also the sequence of metastable intermediate transition aluminas. Also in alumina based coatings, the process parameters have an influence on the thermal transformation

sequence as the transformation from γ- to α-Al_2O_3 is in some cases is based on the formation of an intermediate θ-Al_2O_3. The transformation temperatures cannot be determined with high precision as the crystallinity, defect structure, grain size and especially impurities and dopants have a high influence on them. This influence will be discussed in detail at a later point in chapter 7. The transformation from γ- to α-Al_2O_3 (**Figure 6**) includes a densification as not all possible Al sublattice positions are occupied (as implied in **Figure 6a**).

Alumina's high hot hardness and chemical stability at high temperatures, as well as their low chemical interaction with work-piece materials attracts the coating industry. The first alumina thin films were deposited with chemical vapor deposition (CVD) in the 1970s. Due to the high temperatures that are required for the reaction between the gaseous precursors, the resulting thin films are **α-Al_2O_3** with a coarse grain size. Alumina generally plays a vital role in oxidation protection and the formation of thermally grown oxide scales and therefore α-Al_2O_3 thin films are considered to be among the best oxidation protection coatings [19, 140]. CVD makes the deposition of α-Al_2O_3 thin films possible, but they suffer from impurities, rounding of edges and increased coating thickness at work-piece edges. In addition, the high deposition temperatures of 900 to 1100 °C in regular CVD and 700 °C in plasma-assisted CVD [141] limit the application to temperature and oxidation resistant materials like cemented carbides [142].

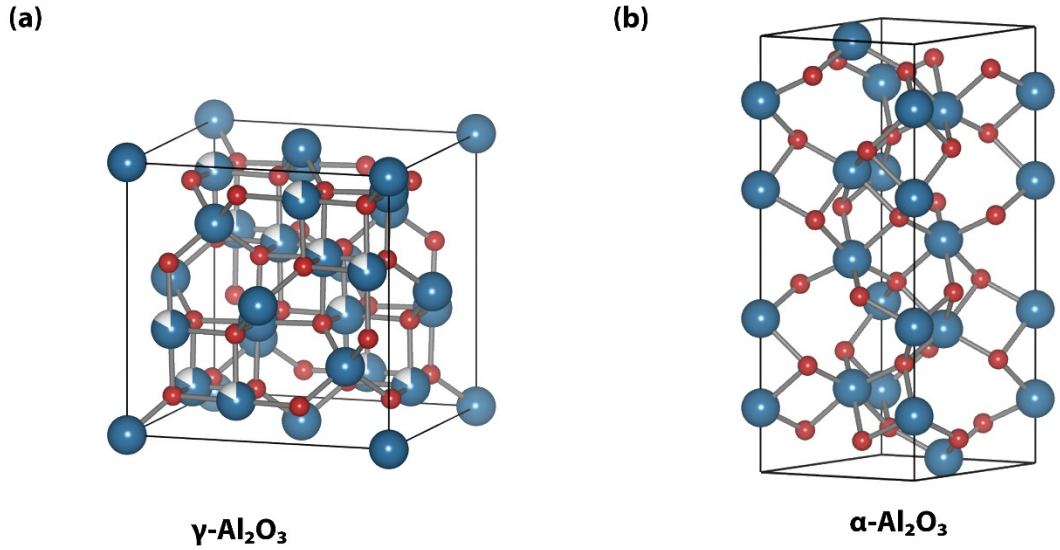

Figure 6: Unit cell of (a) γ- and (b) α-Al_2O_3. Only 83 % of the atom-sites that are not fully colored are occupied [120].

The deposition of alumina with PVD can be achieved at much lower temperatures in a cost-effective process, but the required technological conditions delayed their development until the 90s [143-146]. PVD not only offers a possibility to deposit alumina thin films at low temperatures, but the sputtering process also introduces a compressive stress into the coating that allows for long-lasting sharp edges and reduced crack formation. The major downside to PVD alumina is that the deposited thin films are based on metastable transition alumina structures (predominantly γ-Al_2O_3). The formation of α-Al_2O_3, deposited with pulsed magnetron sputtering was first reported at 750 °C by *Zywitzki* [145, 147]. The formation of alumina thin films is also influenced by the substrate, whereat CrN precoated substrates or Cr_2O_3 substrates assist the formation of α-Al_2O_3, based on a template effect, while the same process with a Si-substrate forms γ-Al_2O_3 [148-151]. Due to the difference in thermal expansion between substrates and the α-Al_2O_3 thin film, the high deposition temperatures, needed for production of PVD α-Al_2O_3, usually lead to cracking of the coating [142, 148, 149].

For many applications, the deposition of α-Al_2O_3 would be appreciated, but is not necessary as γ-Al_2O_3 thin films reach almost equivalent mechanical properties at deposition temperatures as low as 350 °C . At the same time, they offer minimal grain growth up to 1000 °C, a good biocompatibility and due to their high specific surface are of interest as catalyst carriers. As already described above, the main problem with γ-Al_2O_3 thin films is their transformation to α-Al_2O_3 and the coherent shrinking. At the same time, the grain size increases drastically during the phase transformation and the hardness decreases [152]. Chapter 7 will offer some additional insight into the mechanism of the transformation and what can be done to influence the onset-temperature.

Properties of magnetron sputtered alumina thin films (e.g. hardness, structure, crystallinity, chemical composition) are influenced by more than the deposition temperature. Factors like sputter power, bias potential or the oxygen content of the sputter-atmosphere are major influencers as well. In general, they can be summarized by the surface diffusion and the diffusion range x_d of deposited atoms. It is a function of the deposition rate d_s as well as the surface diffusion coefficient, D_s [153, 154]:

$$x_d = \sqrt{2D_s \frac{a}{d_s}} \tag{2.3}$$

$$D_s = D_0 e^{(\frac{-Q}{kT})} \tag{2.4}$$

with the lattice spacing a, the maximal diffusion coefficient, D_0, Q the diffusion activation energy, k the Boltzmann constant and T the substrate temperature. Only if the diffusion length of particles is equivalent to or surpasses the lattice spacing of aluminium oxide ($a = 0.78$ nm) crystalline structures are formed during deposition. At lower diffusion levels amorphous thin films grow.

3 Methodical Approach: From Synthesis to Analytics

Thin films have strongly impacted modern machining applications, the transportation sector and microelectronics. However, many of those innovations owe parts of their success to the immense progress in analytical techniques that facilitated their discovery. Over the past fifty years, science has made a huge leap forward, not just in instrumentation to better understand physical and chemical processes that are involved in thin film deposition, but also to predict them. At the same time instrumentation and methods of thin film deposition have evolved from small scale laboratory approaches to massive industrial applications.

3.1 Thin Films: Deposition and Growth

Thin films are booming, and that, not just in tooling applications, where they are the most visible to people. Over the last decades, they have reached every part of our life. From food packaging, to electronics, our cars, watches and even our glasses, include coated parts [155-158]. As the markets continue to grow, so does the field of research and the wide array of different methods for thin film production. Excluding all solute based methods (which are predominantly used to produce thick coatings), all thin film deposition techniques are vapor-based processes and can be broken down to two groups: chemical vapor deposition (CVD) and physical vapor deposition (PVD) [157-159].

In CVD the underlying principle is a thermally (or otherwise) triggered chemical reaction of at least one precursor that releases the depositing species at the substrate. In some cases the reaction is a simple thermal decomposition at the substrate, in others it is a complex reaction between gaseous metal containing precursors (e.g. $TiCl_4$) and corresponding gaseous reactants like H_2O, NH_3, N_2, H_2 or many others. One example would be the formation of TiN based on a reaction between $TiCl_4$, N_2 and H_2 [160].

This thesis covers PVD thin films and hence we will further focus and expand on physical vapor deposition. In PVD, the reactive metal-based vapor is not provided in the form of gaseous chemicals, but is rather generated by a physical process. When the kinetic energy of target atoms exceeds the surface energy of the bulk material, evaporation is possible. The power input needed for this process divides vaporization into those methods using thermal energy and those conveying energy by impulse transfer. A PVD process takes place in three steps: a transition of target material into the gas phase, followed by a transport to the substrate, where the target species deposits and film growth occurs [155, 156]. PVD is further subdivided according to which method is used to generate the target vapor. A few examples are pulsed laser deposition, electron beam evaporation, sublimation (e.g. in molecular beam epitaxy), arc evaporation, or sputtering (as the most common technique).

The whole success story of PVD started much earlier than one would expect, with *W.R. Grove*'s sputtering in 1852 [161]. Even a sketch of PVD's development could potentially fill another PhD thesis and therefore I am glad to be able to refer anyone to J.E. Greene's extensive review of PVD history [162] while I will highlight only the evolution steps of PVD [163] that are relevant to this thesis.

3.1.1 Sputtering

For a better understanding of the sputtering process, I will first discuss the generation of a plasma and the different stages of a plasma discharge. Sputtering is realized in an argon atmosphere at a pressure of roughly 0.1 to 10 Pa. The selection of Ar arises not only from its chemical inertness, but also from its mass, as the momentum transfer depends on the colliding particles mass, marking heavy Ar as an efficient sputter gas. If a negative potential is applied to the cathode (**Figure 7**) that exceeds the breakdown voltage (**Figure 8**) of the process gas, an electron from the Ar atom is emitted, leaving an Ar^+ ion behind. In the electric field, the ion and electron are being accelerated and collisions with other gas particles build up to a chain reaction, igniting the plasma. The current-voltage characteristic of a plasma in **Figure 8** exhibit three discharge regimes:

- Dark discharge, in which no emission of visible light occurs (except for possible corona and breakdown discharge). Due to background ionization (e.g. as a result of natural radiation), an ionization is measurable (voltage not zero). As a potential is applied, the current increases due to attraction of aforementioned background ions until a saturation regime is reached. In the following Townsend regime, the voltage is high enough to accelerate electrons, which themselves cause collision and a not self-sustainable ionization.
- Glow discharge is reached, when the voltage surpasses the already described breakdown voltage. The recombination and relaxation of excited ions emits light, giving the plasma its characteristic glow. The self-sustaining glow discharge is defined by a characteristic voltage drop to a stable level. At this plateau (also called normal glow) the increase of current is facilitated by an expansion of the plasma over the whole cathode surface. Once the full cathode contributes to the current, a further voltage increase is necessary to surpass the natural current density limit. PVD sputter processes are being operated in this

section, as the cathode potential and current can both be considered for process control. The sputtering plasma is described as a 'cold plasma' with a constant state of thermal non-equilibrium with ions at a temperature of about 300 K and electrons at an energy level associated with much higher temperatures [156].

- Arc discharge occurs, when the plasma-current heats the target surface to a level at which the emission of electrons from the metallic surface is possible and an electric arc is formed. This is characterized by a low voltage and high current state of the plasma. Self-extinction and re-ignition of the arc in nearby spots guides it over the target surface, leading to local temperatures of up to 15000 K, providing the basis for arc evaporation PVD. Arc evaporation is also defined by a high degree of ionization (>90 %) [164, 165] and high deposition rates.

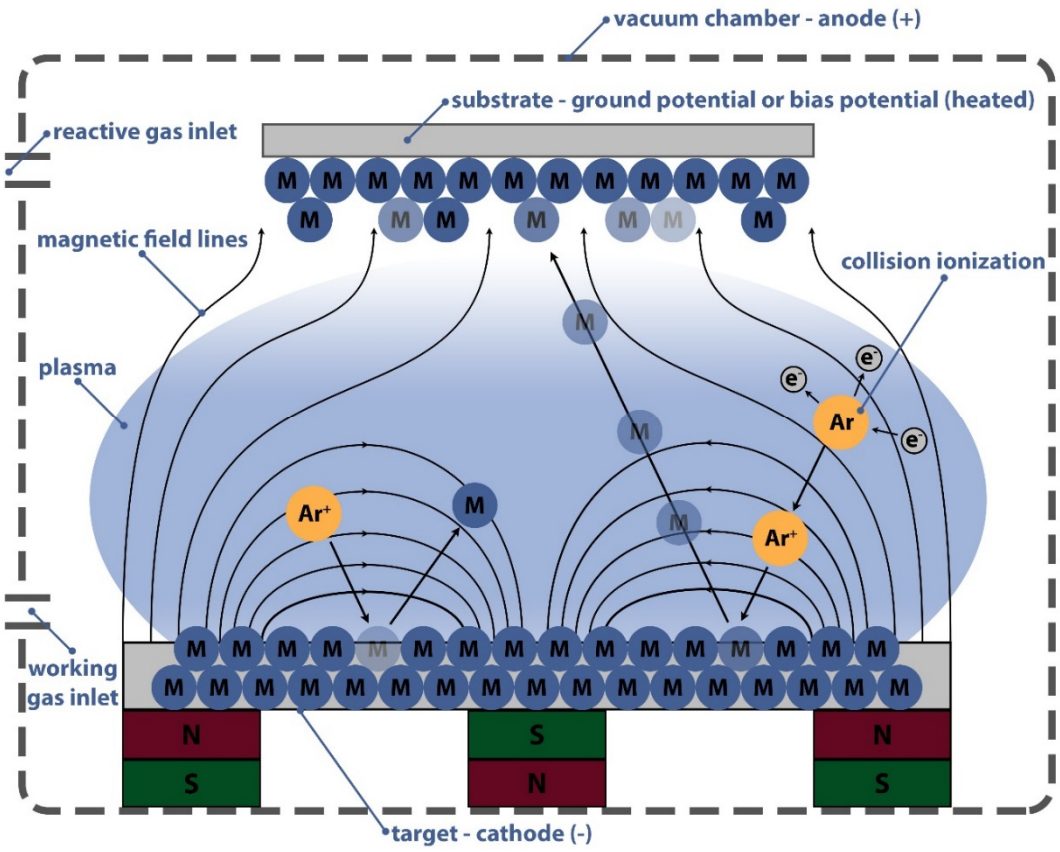

Figure 7: Arrangement of a magnetron sputtering system that allows for the use of reactive gases. The magnetic field-lines trap electrons close to the target to allow for sputtering at lower pressures and lead to the formation of the race track.

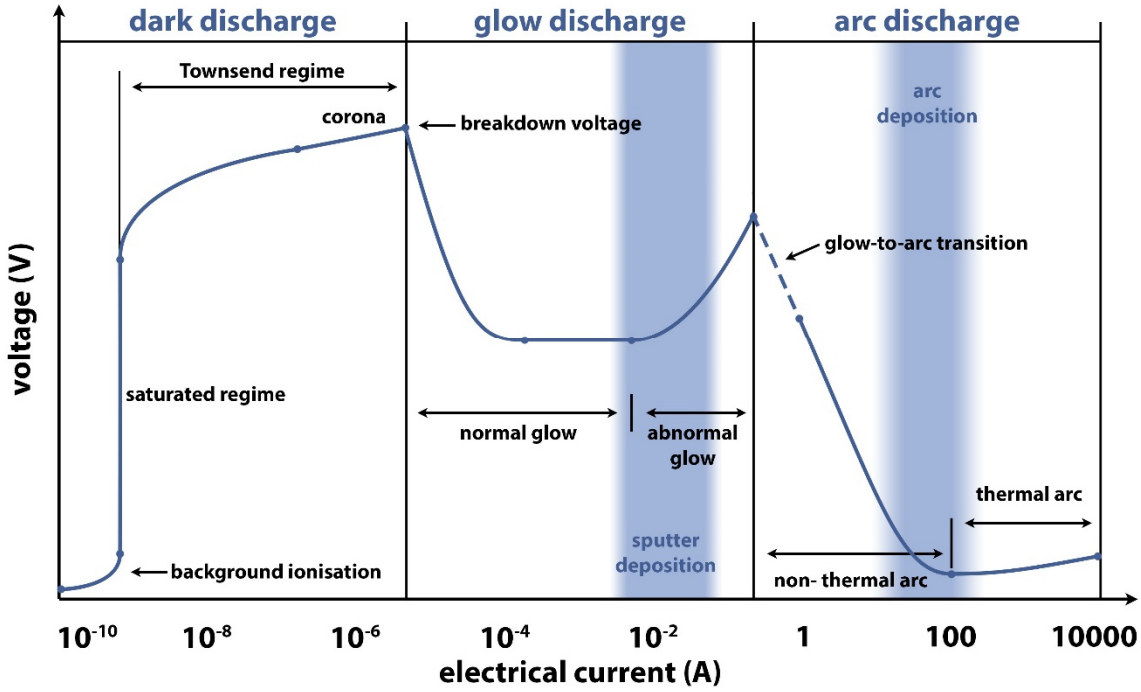

Figure 8: Schematic of a voltage-current characteristic for different regimes in plasma discharges adapted from [42]

Returning to the glow discharge in sputtering, in particular to the ions of the self-sustaining plasma, the positive Ar^+ ions are attracted by the electric field and accelerated towards the cathode, as shown in **Figure 7**. Upon collision with the target surface, the impinging Ar ions initiate a collision cascade with many competing interactions, that are further presented in **Figure 9**. The most important event is sputtering, in which the momentum of the impinging ion is transferred to target atoms and during the collision cascade the impulse is sequentially turned around and hence, target material is ejected that can further on deposit on the substrate. Sputtered particles leave the target surface with a cosine distribution and are primarily neutral with only a small fraction of about 1 % ionized species [158]. A second essential interaction is the generation of secondary electrons that are indispensable for sustaining

the Ar ionization in the plasma. Most of the energy that is introduced to the target surface is unfortunately converted into heat, making it necessary to water-cool cathodes despite the obvious headaches that arise from having high vacuum, high temperature, high currents and water in close proximity [156, 158, 166].

To achieve high deposition rates, it is essential to minimize scattering of sputtered particles and hence, maximize their mean free path. This can only be achieved by reducing the pressure of the deposition atmosphere. At the same time, decreased pressure implies reduced plasma density and at even lower pressures a collapse of the self-sustaining plasma, unfolding a catch-22 situation.

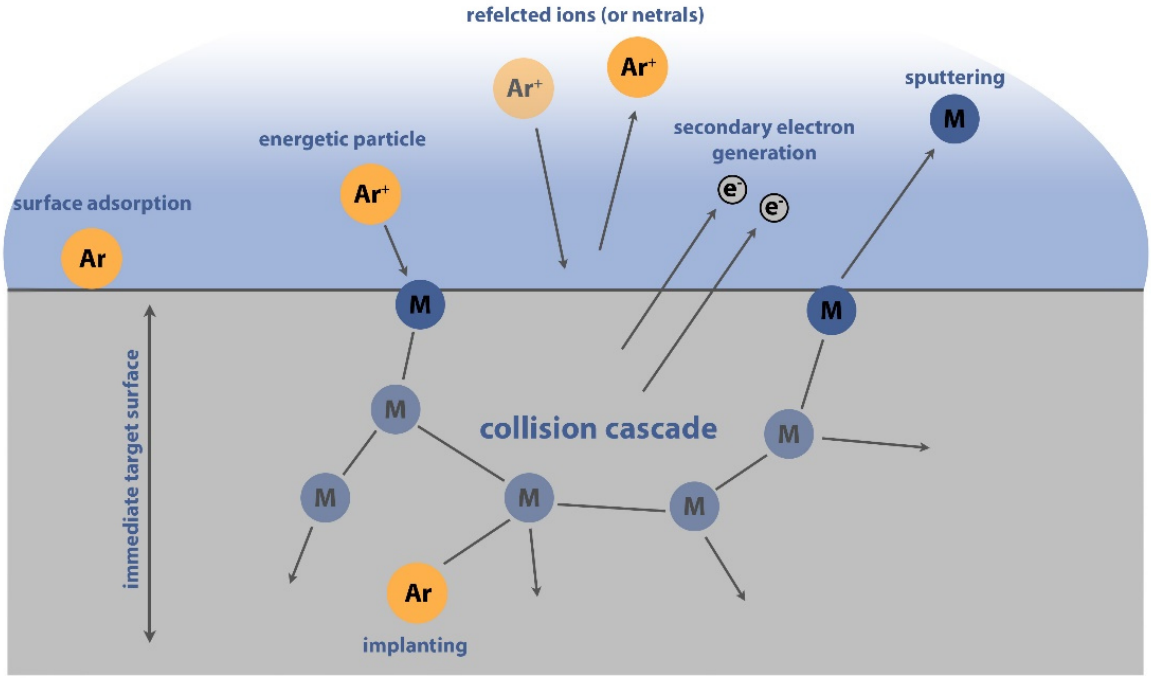

Figure 9: Common events after ion impact on a surface, highlighting the collision cascade [166].

3.1.2 Magnetron Sputtering

One evolution of sputtering, magnetron sputtering, addresses these abovementioned mean free path-length problems by superimposing the electric field with a magnetic field. This results in an additional Lorentz force on accelerated charged particles in the plasma that affects light electrons much more than heavy ions. The Lorentz force can be described by:

$$F = q(E + v \times B) \tag{3.1}$$

with the particle's charge q and velocity v in the electric field E and magnetic field B. A correct placement of magnets traps electrons on a gyrating trajectory and significantly increases the number of collisions per electron [166, 167]. In magnetron sputtering the plasma therefore remains self-sustaining at low deposition pressures in the range of 10^{-4} mbar. The circular trajectory of electrons also results in the formation of a circular erosion trench, called racetrack.

The magnetron can be realized in two setups: In balanced magnetron sputtering, all magnets are adjusted in strength, to terminate all magnetic field lines in a center magnet, leading to a confinement of the plasma close to the target. For many techniques it is beneficial to have some activation of the gas phase close to the substrate, influencing the film growth [168]. To gain an activation of the gas at the substrate, an unbalanced magnetron with a weaker central magnet and a stronger annular outer magnet can be applied. The unbalanced strength of the magnets means that not all magnetic field lines can terminate in the center magnet and results in a cone-shaped up-folding of the magnetic field lines with a 'leak' at the tip, extending the plasma close to the substrate (as displayed in **Figure 7**).

Every process can be quantified according to its efficiency. In sputtering the high amount of individual process steps is summarized in the sputter yield. It is a very complex result that is affected by many factors: bond energy E_b of the target material, impact ion energy E_i, the angle at which the ion impinges, as well as the mass m_i and m_t of the impacting ion and a target atom, respectively. The sputter yield was described by *Sigmund* [169] with the following formula:

$$Y = \frac{3 * \varepsilon}{4 * \pi^2} * \frac{4 * m_i * m_t}{(m_i + m_t)} * \frac{E_i}{E_b} \tag{3.2}$$

It is limited for ion energies E_i lower than 1 keV, as at higher energies the ion implantation increases and reduces the overall sputter yield. The sputter yield also has an angular dependence:

$$Y' = \frac{Y}{\cos \delta} \tag{3.3}$$

whereas δ is measured from the perpendicular to the target surface.

3.1.3 Reactive Sputtering

With magnetron sputtering, we can now deposit many different metallic materials, but if the deposition of metal-based compounds like oxides or nitrides is desired instead, things get a bit trickier. It is possible to produce the corresponding compound targets, but due to (in most cases) higher bond energies sputter rates are much lower than for metals. At the same time, many of those compounds are not conductive and prevent sputtering. While it is possible to overcome these problems with modulating the direct current (DC) power input by pulsing or radio frequency (RF) sputtering, a much more elegant approach is to form the compounds during the deposition in a reactive sputtering process.

In reactive sputtering, the process gas consists of Ar and a reactive gas like oxygen, nitrogen or acetylene for the formation of oxides, nitrides and carbides, respectively. In any case, the low mass of reactive gases would not allow for sufficient deposition rates without the addition of Ar. During deposition, the reaction of the sputtered species with the gaseous reaction partner can occur during the transport from the target to the substrate or directly at the substrate surface [170]. As already mentioned, the unbalanced magnetron allows the plasma to extend to the substrate, where it activates the reactive gas and supports the reactive compound forming process [168].

The main problem of reactive sputtering, is similar to what was already mentioned as limitations for nonreactive sputtering: the formation of isolating compound at the target surface [171]. In order to reduce this effect, many reactive sputtering systems have separate inlets for Ar (close to the target or in the cathode) and reactive gas (close to the substrate, **Figure 7**). Reactive gas is consumed by either the pumping system, or the formation of compound with the sputtered metal. If the concentration of reactive gas is low, the reaction is confined to inlet near regions (around the substrate). At this stage, the target surface is free from compound and the target is operated in what is called the metallic mode. Sputter rates are high, and the thin film quality is mainly limited by kinetic effects (e.g. surface diffusion) and the availability of reactive gas at the substrate. Inarguably, a reactive gas deficiency leads to the formation of sub-stoichiometric or even metallic thin films.

With an increasing reactive gas flow, the reactive gas reaches further into the plasma, before it reacts with the sputtered metal, until it reaches the target surface. At this point, the formation of a compound layer at the target surface initiates an unstable transition region. Islands of compound form and inevitably locally change the surfaces' electrical and thermal conductivity. In many systems (e.g. Al-O) this leads to sever arcing event and a process instability. Sputter- and deposition rates start to decline

and in consequence, the amount of consumed reactive gas decreases, quickly tipping the scale in favor of a complete compound coverage of the target surface.

The target now operates in the poisoned mode. Sputter rates are extremely low and most of the energy is lost to competing effects like secondary electron generation [171]. As shown in **Figure 10** for the Al-O system, this significantly changes the electrical behavior of the plasma, as the increase in charged particle allows for the transport of a higher current (in a sputter power controlled process this means a reduction of the voltage). It is necessary to mention that different material systems can demonstrate completely different behaviors when the target surface poisons. In the poisoned mode, the thin film quality often suffers as well [153]. Instead of metallic atoms (or clusters), compound fragments are sputtered and once deposited, the energetic barrier for surface diffusion to form crystalline structures is very high. As a result, thin films deposited in poisoned mode often are amorphous with weak mechanical properties.

Once a target is poisoned, the simple reduction of the reactive gas (back to levels of the transition region) is often not enough. As the surface is already covered with compound and the sputter rate is low, a much more significant drop of the reaction gas concentration is required to remove the compound layer and keeping it from re-covering the surface. This effect can be seen in **Figure 10** and is called the hysteresis effect [172, 173]. The easiest way to reduce the hysteresis effect would be to reduce the reactive gas concentration and accomplish reactant sufficiency by high flow rates. At industrially relevant deposition rates, this would unfortunately require unachievable pumping speeds. Other approaches suggest the reduction of the erosion area [174], the use of segmented targets [175] or rely on technology intense feedback control in which the state of the plasma or gas composition is measured and the reactive gas flow rate is adjusted in a feedback loop [176]. Further details on the stabilization of the transition region and a new approach via micro-alloyed Al targets will be given in chapter 6.

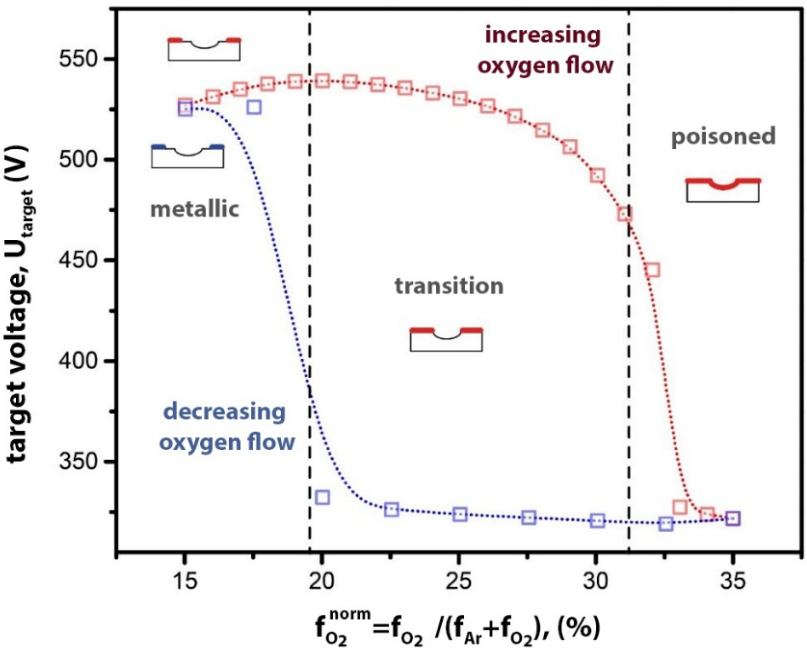

Figure 10: Poisoning behavior of an Al target in Ar/O_2 mixture, demonstrating the three operation modes in reactive sputtering.

3.1.4 Film Growth

The growth of thin films is highly dependent on the deposition parameters and has a huge impact on its mechanical, thermal and chemical properties. When a sputtered species hits the substrate, it can either be reflected, or condensed as 'adatom' under transmission of energy to the substrate. PVD is characterized by an extreme cooling rate when the evaporated species comes in contact with the substrate. As a result PVD is able to deposit metastable phases, sometimes even limited to metastable phases as the energetic barrier for formation of stable phases might be too high for the rapidly cooled species. Depending on substrate temperatures and energy input via ion bombardment (tunable by the bias potential) a certain amount of surface diffusion is possible, resulting in the formation of clusters followed by nucleation and thin film growth [23, 156].

Three types of growth can be differentiated:

- Frank-van der Merwe growth (2D layer by layer): The adatom to adatom binding energy is lower or equal than the binding energy to the substrate [177].
- Volmer-Weber growth (3D island growth): The adatoms to adatoms bond is energetically favorable over bonds with the substrate atoms [177].
- Stranski-Krastanov growth: Is a mix between the 2D layer and the 3D island growth. Initially, the deposition is layer by layer based until it becomes unfavorable after a few layers leading to island growth on top [177].

Compiled data of the influence of different sputter parameters on coating morphology led to the development of structure zone models (SZM). Based on initial work by *Movchan* and *Demchyshyn* [178], *Thornton* [179], and *Messier* [180], *Anders* developed the most widely used SZM [181]. In his model, pictured in **Figure 11**, the film thickness t^* as well as the coating morphology can be predicted by a generalized temperature T^* and the normalized energy E^*. The generalized temperature is defined as the ratio between the deposition temperature and the melting point, which has been shifted to account for the energy input by ion bombardment due to applying bias. The normalized energy E^* can be calculated according to:

$$E^* = \sum_{\alpha} \frac{E_{kin,\alpha}}{E_c} * \frac{m_\alpha}{m_s} * J_\alpha \Big/ \sum_{\alpha} J_\alpha \tag{3.4}$$

with E_c being the cohesive energy, m_s the mass of surface atoms and J the energetic flux [181].

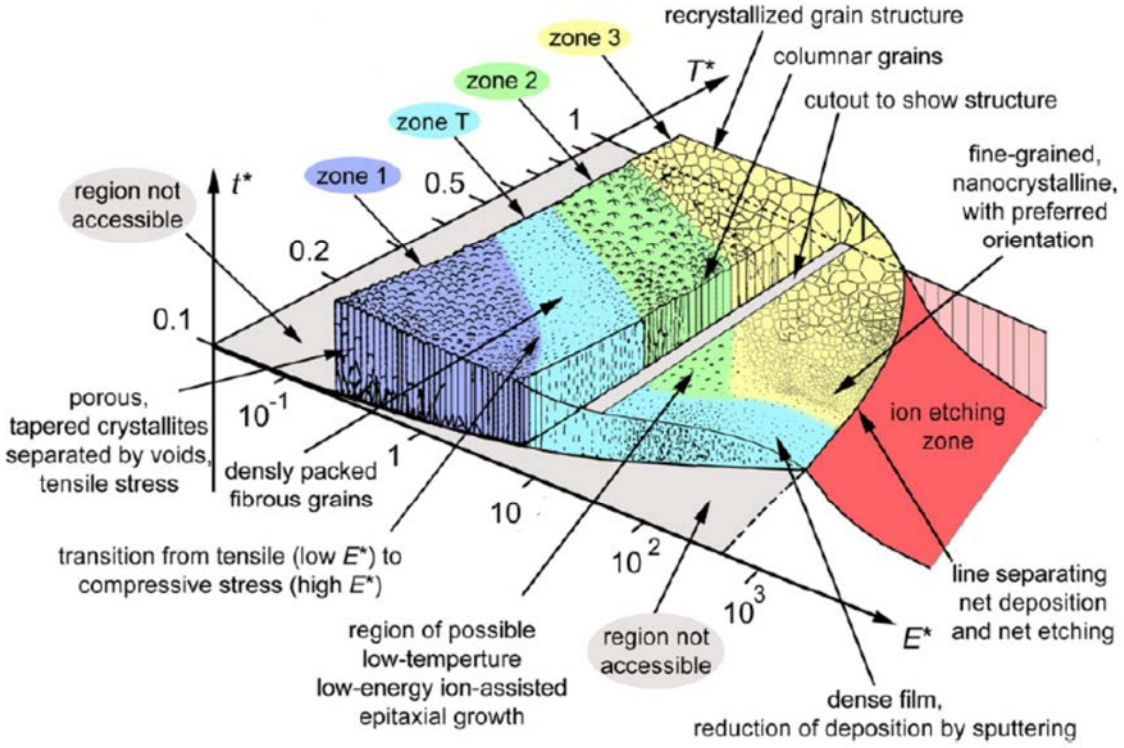

Figure 11: The structure zone model, as proposed by A. Anders [181], provides information about the influence of the deposition parameters on the morphology of coatings.

Zone 1 films are characterized by low adatom mobility and a 'hit and stick' growth of amorphous thin films with a high surface roughness. Closer to the transition zone T adatoms are becoming increasingly mobile which allows for small crystallites can develop and form a columnar structure [182]. In the transition zone T, surface diffusion reaches a range that facilitates diffusion between grains, resulting in competitive crystal growth with a slightly V-shape columnar structure and preferred crystallographic orientations. If the Energy is further increased, recrystallization occurs to minimize the grain surface and therefore the interface energy. In zone 2, thin films have straight columns with dome-shaped tops, little shadowing effects and almost no angular dependence [182]. At even higher temperatures in zone 3, surface diffusion is higher than the formation of defects by ion bombardment and renucleation, resulting in a recrystallized grain structure. Increasing temperature leads to significant grain growth.

So far, I primarily discussed the changes with increasing T^*. If we increase the energy normalized energy E^* we increase the films density, which can have positive influence on their mechanical properties. Above a certain E^*, the impinging particles reduce the deposition rate to a point where sputtering at the substrate occurs at a higher rate than the deposition (ion etching zone) [181].

3.2 Tribofilm Analysis and its Difficulties

In this segment, an insight into the possible analytical methods will be given, whereat the focus is set on specific difficulties of this work rather than a general method introduction. While the analysis of thin films with a few µm of thickness already requires high technological expenses, the investigation of tribofilms with sometimes only a few atom layers thickness is even more complicated. With sample volumes this small, even the most modern and sensitive methods of surface analyses reach their limits.

One general issue that needs to be addressed is energy transfer to the tribofilm. Tribofilms are chemically and structurally very complex and often without a precise composition or structure. Due to the almost unquantifiable conditions in friction contacts, the products of a tribochemical reaction often are non-stoichiometric and vary in exact chemical composition or structure. As a result, the films are not in their thermodynamic equilibrium state and although non-destructive analytical methods are applied, the energy input by the chosen method might be enough to trigger phase transitions. This might be the degradation of organic species or a simple crystallization of originally amorphous compounds. To avoid flawed analysis, the chosen methods as well as their consecutive order must be chosen with particular attention to detail and if needed must be reflected with reference measurements.

3.2.1 Scanning Electron Microscopy and Focused Ion Beam

Scanning electron microscopy (SEM) is often used to investigate the wear scar of tribological tests. Electrons are extracted from a hot W filament or a field emission gun and accelerated towards the sample. An array of lenses and deflectors focuses the electron beam, guides it and is responsible for corrections, magnification and the scanning motion. The electron beam interacts with the sample and among other processes emits secondary/back-scattered electrons and characteristic X-ray radiation. Secondary electrons have a much lower energy and are siphoned off towards a detection unit by attracting them with an electric field. This provides nice topography images of the wear scar, but not much information on the tribofilm. In order to determine in which regions a tribofilm has formed, the SEM's backscattered mode can be used. A fraction of the incoming electron beam is reflected due to elastic scattering and can be detected with a circular backscattered electron detector around the pole shoe. The elastic scattering process correlates with the sample's atomic number. Therefore, tribofilms that often contain low atomic number elements like carbon, oxygen, or in our case sulfur, appear darker than the metallic surfaces.

For transmission electron microscopy (TEM) the only reliable method to produce cross section samples of the tribofilm is focused ion beam (FIB). FIB is coupled with SEM and allows the imaging with a Ga^+ ion beam. The ion beam acceleration and intensity can be increased up to levels allowing the sputtering and cutting of samples. It is self-explanatory that if the tribofilm is just a few nm thick, a single image (taken with the ion beam) alters or destroys the tribofilm. To protect samples, in FIB usually a protective Pt layer is deposited on the sample area. In order to conserve the tribofilm it is essential that the first section of the protective Pt film is deposited as gentle as possible.

Unfortunately, soft tribofilms are easily sputtered out of the narrow gap between the protective Pt and the sample surface. This can be avoided by thinning the TEM sample in a wedge form at lower ion beam intensities than usual. Additional thinning with a precision ion polishing system or similar, as well as plasma cleaning should be avoided.

3.2.2 Energy-Dispersive X-ray Spectroscopy

Energy-dispersive X-ray Spectroscopy (EDX) is an ad-on for SEM or TEM. As the electron beam interacts with the sample collisions occur resulting in the generation of electron holes in the sample atoms' inner shell. These vacant orbital positions are energetically favorable over the outer shell. Electrons from the outer atom shell transit to these (lower energy) positions and emit the difference of energy as either X-ray radiation or Auger electrons (light electrons favor Auger electron emission). Which transitions are allowed is specified by the quantum mechanical selection rule. Each element emits a distinctive pattern of discrete lines [183].

In SEM, the activation volume of the electron beam resembles a teardrop shape with a few µm in size. Low energy secondary electrons can only escape from the narrow activation region directly at the surface, resulting in a high spatial resolution for imaging. While generated secondary electrons in the lower majority of the activation volume are trapped there, the produced characteristic X-ray radiation has no problem emerging from this sampling depth. This limits the achievable spatial resolution of EDX coupled with SEM drastically. Very thin tribofilms are lost in signal noise and thicker tribofilms or debris can be detected, but the quantification is unreliable due to the interfering substrate.

The spatial resolution of EDX in TEM is much higher because the thin lamella (≤150 nm) results in a very small activation volume. TEM EDX line scans and imaging therefore is a useful tool for tribofilm investigations, but only if the sample preparation did not alter the tribofilm.

While EDX performs well in the investigation of WS_2 based tribofilms, it cannot analyze MoS_2 based tribofilms because S-K lines (2.307 keV) and Mo-L lines (2.293 keV) overlap. While Mo offers the Mo-K line for quantification, S has no additional lines in EDX and cannot be quantified. In order to quantify Mo and S contents in TEM samples, we applied electron energy loss spectroscopy (EELS).

3.2.3 X-ray Photoelectron Spectroscopy

Based on the findings of *Hertz* [184] and *Einstein* [185], discovering and explaining the photoelectric effect, *Siegbahn* developed the surface analytical method of X-ray photoelectron spectroscopy (XPS). The sample material is irradiated with a focused X-ray beam in an ultra-high vacuum (UHV). The radiation interacts with atoms and is able to induce the emission of photo electrons from the top 10-20 nm of the sample. The electrons are detected and provide a spectra in dependence of their kinetic energy, E_{kin}. Because the energy E_{phot} of the applied X-ray radiation is known, the electron binding energy E_{bind} can be calculated as such:

$$E_{bind} = E_{phot} - (E_{kin} + \phi) \tag{3.5}$$

Whereat the work function term ϕ corrects energy losses at the detector. This method not only allows to investigate the elemental composition of the sample, it also allows to determine the electron configuration of these elements and therefore allows to draw conclusions about the atom's bonding. The capabilities of XPS make it an extremely valuable tool for the analysis of tribological contacts and tribofilms.

Unfortunately, in the detection of WS_2 or MoS_2 based tribofilms its possibilities are limited due to the similar electron configuration of the involved molecules. **Figure 12** outlines those problems on the example of the generation of a WS_2 based tribofilm on a WC containing surface. Although the peak position of WS_x peaks allow for a distinction from other bonding signals, the S 2p peaks are often of very weak intensity in tribofilm (barely above noise), making elaborate peek fitting and complex peek convolution essential for accurate conclusions. A better signal can be obtained by investigating the W 4f orbital. Unfortunately the binding energies for and therefore the peak positions of WO_2 and WS_2 are very similar. With the small sample concentrations (the tribofilm contains mostly oil-derived C-based debris) and the low signal/noise ration it is not possible to reach a certain conclusion about the formation of WS_2.

Because XPS is extremely surface sensitive, it is usual to sputter clean the sample (from oxides and gaseous adsorbents) before measuring. For the investigation of tribofilms it is highly recommended to measure depth profiles (at very low sputter rates), with the first measurement being carried out prior to any first sputtering. This allows to determine, if the investigated tribofilm is altered or damaged during the measurement.

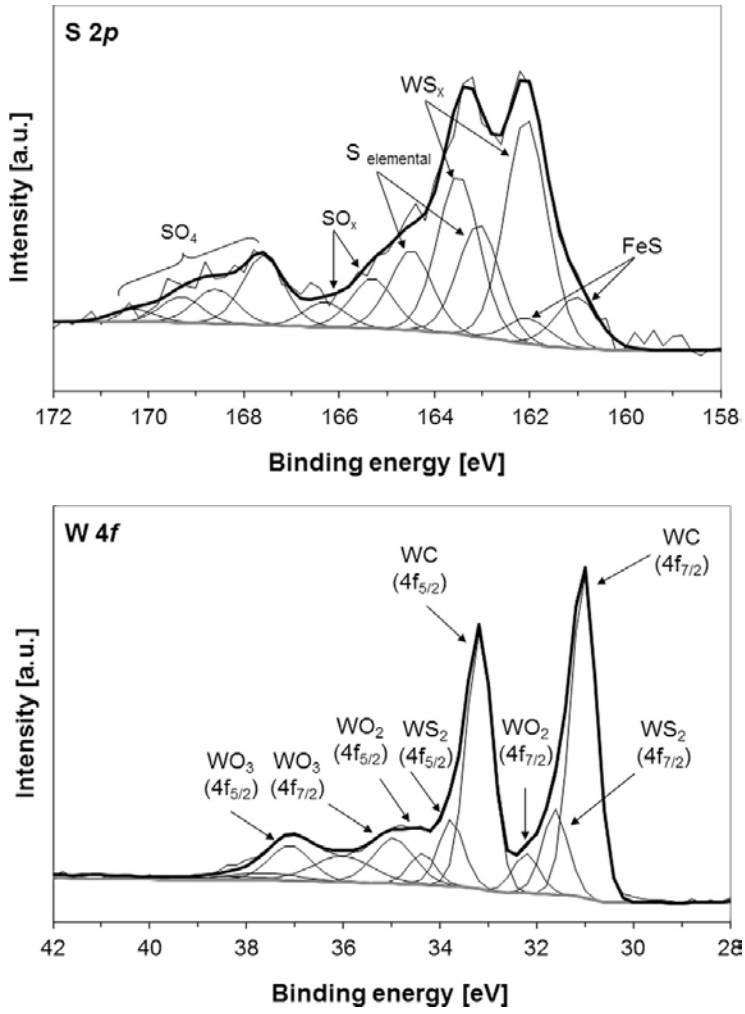

Figure 12: High-resolution XPS fitted spectra of S 2p (top) and W 4f (bottom) for a WC hammer peened surface with 1.5% EP additive, tested at 10 N load [186].

3.2.4 Secondary Ion Mass Spectroscopy

Another very surface sensitive method with detection limits below 1 ppm is secondary ion mass spectroscopy (SIMS). The technique was developed by *Herzog* and *Viehböck* at the University of Vienna [187]. The sample is probed by scanning with a focused pulsed ion beam. A signal enhancement can be achieved by sputtering with O_2^+ for positive ions and with Cs^+ for negative ions, due to reactions with the sample surface [188]. Upon impact of the primary ions on the sample surface, neutrals and secondary ions that represent the samples surface chemistry are generated. Secondary ions are

being extracted and analyzed with mass spectroscopy (usually time of flight mass spectroscopy, TOF-SIMS [189]). By intermitting measurements with sputtering sequences that ablate the investigated sample area, allows to record depth profiles with a high depth resolution [190, 191]. At increasing depth, the depth profile resolution is limited by a momentum transfer from the primary ions to the sample material, which causes atomic mixing. Roughening of the sputter crater bottom, due to differences in sputter rates (chemistry, orientation,…) limit the resolution at high sputter depths as well. While the qualitative information of SIMS is highly accurate, the quantification is more difficult. The sputter rate varies for different elements, crystallographic orientation and densities. Especially in complex samples, due matrix effects, the use of very intensive standards, that reflect the sample accurately is required [192]. Due to the different sputter yields of components, enrichment and depletion of some elements can occur.

Like XPS, SIMS is a very powerful tool in the investigation of tribofilms and gives information about the molecular composition of a tribofilm due to the generation of molecule fragment ions like $(MO_x)^{y-}$. Due to the high impact energy, thin tribofilms are completely ablated after only a few measurements (without additional sputtering). Depth-profiling is therefore hardly possible and even in thick tribofilms, the typical roughness of the contact surface and tribofilm reduce depth resolution drastically.

Unfortunately for our TMD based tribofilms, the resolution of TOF SIMS struggles with differentiating between WO_2^- (M = 215.84 u) and WS^- (M = 215.91 u), typical fragments of tungsten oxide and tungsten sulfide, respectively. The same applies for all Transition metal sulfides and oxides and hence, it is not possible to differentiate between tribochemically formed sulfides and commonly formed oxides (which also cover every metallic surface). A simple demonstration in **Figure 13** show a SIMS image of WS_2 containing debris on the side of the wear track on a tungsten nitride based coating.

WO_2^- and WS^- are recorded as a single signal. At first glance, one would think that the tribofilm does not contain any tungsten oxide or sulfide at all. Yet, this is simply an imaging problem as the surface oxide scale on the coating with a high intensity superimposes the weak intensities of the tribofilm (that also contains a substantial amount of carbon-based species). If we take a look at the signals of elemental S^- in **Figure 18**(which can be differentiated from O_2^- due to increased resolution at low overall fragment mass) it is visible that S based species are present in the debris.

SIMS can offer an insight into many tribofilms, but when it comes to the differentiation between transition metal sulfides and oxides, the gained information is not sufficient and only offers hints about the formation of transition metal disulfides.

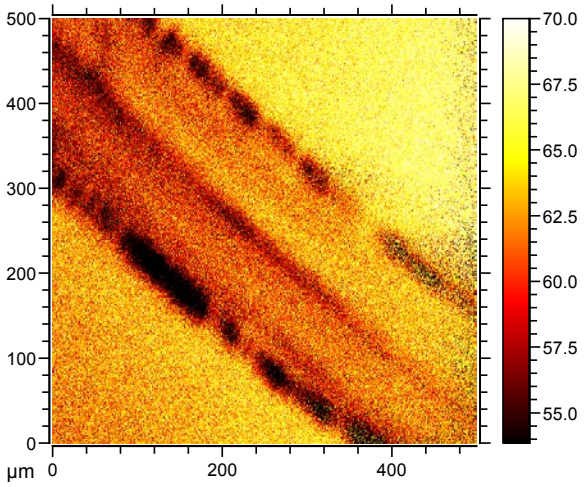

Figure 13: SIMS image (WO^{2-}/WS^- signal) of a WS_2 containing tribofilm.

3.2.5 Raman Spectroscopy

Studies of a young Indian scientist, *C.V. Raman* [193], were the first to discover that when light is scattered by materials not all scattered photons are of the same wavelength as the incident beam. Light can be scattered without the transfer of energy to the scattering material at the same wavelength (Rayleigh scattering), or by

transferring or absorbing discrete quanta of energy to or from the material (Stokes Raman- and Anti Stokes Raman scattering, respectively). This leads to a Raman shift of the scattered photon wavelength and leaves the scattering atom in a changed excitation state. As for other optical spectroscopy methods, in Raman spectroscopy primarily vibrations and excitations of similar energy levels are induced according to strict selection rules.

The big breakthrough of Raman was the development of lasers that allowed for high intensity monochromatic light sources that could also be coupled with microscopes. This gives Raman a high surface sensitivity, as the microscope can be focused directly on the tribofilm. In case of our TMD tribofilm, Raman spectroscopy is the perfect tool for differentiating between the formation of oxides and the formation of sulfides, both with different Raman signals. While this is a huge upside for this work, the downside of Raman spectra is the lack of comprehensive databases to identify unknown substances. Raman signals are very sensitive to crystal defects and crystallite defects, leading to the unlocking of originally inactive Raman modes and significant peak shifts. In case of e.g. MoS_2, the peaks of a single S-Mo-S sandwich can be shifted by up to 25 cm^{-1} in comparison to bulk MoS_2. It is therefore necessary to measure reference spectra wherever possible. A more detailed explanation of MoS_2 peak shifts can be found in chapter 5.

4 In-situ formation of high performance low-friction tribofilms

Despite growing environmental concern, combustion engines are projected to stick around for some time, so will unpopular S- and P- containing additives in lubricating oils. Therefore, it is essential to maximize efficiency and minimize the harmful impacts of these additives in the meantime. Coatings based on Mo and W hold great promise as they can chemically interact with S-bearing additives and form low friction tribofilms like MoS_2 and in particular WS_2.

Twenty-two percent, that is the shockingly low energy fraction of an internal combustion engine that actually moves our cars in relation to the chemical energy we pour into them in the form of fuel [2]. The energy we allocate to simply overcome the friction of engine and transmission alone is roughly 17 % [2]. Environmental concerns and the resulting legislative pressure (to reduce emissions) are mounting and pushing manufacturers to offer more efficient engine designs. While it is unlikely, that we will soon fully substitute internal combustion engines with electric vehicles, the necessity for increased mobility is unabated. Even a complete substitution with electric motors only predicts to cut the losses due to friction approximately in half [1, 4]. Two strategies have been pursued in the control and reduction of friction and wear on machine elements: (i) the optimization of lubricants and (ii) the improvement of the contact interface by increasing the surface quality or functionality, i.e. by surface texturing or

by the application of coatings like DLC on selected component surfaces [5].

On the lubrication side, low viscosity and ultra-low viscosity lubricants (like 0W16 or 0W8) can reduce viscous losses, but at the expense of wear protection due to much increased metal-to-metal contacts. To compensate for the reduced surface separation by such oils, and increase service life in general, additives have to take on wear protection. Early discoveries highlight that lubrication and wear protection are not solely reliant on a hydrodynamic oil film between two counteracting surfaces. Under mixed friction and particularly under boundary lubrication thin reaction layers, called tribofilms, which originate from interactions between exposed surface material and lubricant molecules or additives, avert any direct contact between the components' surfaces [66]. In engines (with constant changes of the sliding speed and direction), the whole range of the Stribeck-curve is utilized and modern cars' automatic start-stop mechanisms highlight the necessity to protect surfaces with a tribofilm in boundary lubrication and even in the initial motion, when the stiction of direct surface contact has to be overcome.

The most common additive in lubrication is ZDDP [73], which under the influence of shear stresses decomposes [71, 194] and (due to the entropy gain driven tribochemical reaction) [72] forms protective phosphate based tribofilms. With its high S and P content, ZDDP is under scrutiny for environmental concerns and negative effects on a car's after treatment catalysts and exhaust filters. Current oils are highly refined to provide not only low friction and wear, but also to maintain good viscosity over broad temperature ranges, as well as to inhibit oxidation and corrosion at the same time [73]. A combination of ZDDP and Mo and S containing additives, i.e. molybdenum dithiocarbamate, reduce friction based on the formation of MoS_2 [195]. So far, it is not possible to completely eliminate S and P from our lubricants, as no direct substitutes for those additives are available. Wear protection of the future engines will rely on a

complex range of additive technologies [74]. Some of the most promising candidates include layered transition metal dichalcogenides like MoS_2 or WS_2. Their unique 2D structure consists of a layer of metal atoms, that is covalently sandwiched between two layers of chalcogen atoms, which can provide exceptional mechanical and tribological performances in addition to impressive optical [107] and electrical [105, 106] properties. In bulk TMD structures, the individual sandwich sheets are stacked on top of each other while being only weakly bound by Van der Waals interaction, creating an easy shear plane, predestined for solid lubrication. TMDs, in form of nanoparticles [79, 84, 196] (in lubricants) or coatings (unlubricated) have attracted particular attention due to their chemical stability, which in comparison to ZDDP reduces the negative effects of S and does not pose environmental concerns [61, 75, 80, 82].

Nanoparticles based on TMDs are troubled with high production costs, and once blended with lubricants, can agglomerate especially in the absence of dispersants (which in return reduces their lubricating effect [79, 81]). On top of that, nanoparticles pose potential health risks, leading us to our goal of generating TMD, particularly WS_2 in-situ (due to its better thermal stability and load bearing ability compared to MoS_2). Conventional lubricants have been developed to operate on ferrous surfaces and cannot reach their full potential in combination with the increased application of coatings. Pioneering studies demonstrated that a reaction between S from lubricant additives or H_2S [53, 54] and W or Mo containing surfaces is in principle possible [88, 186, 197], but so far only modest improvements were achieved or the tested surfaces were of lower technological relevance. In order to enable this in-situ formation on all types of materials, and at the same time protect the surfaces from wear and excessive consumption, our approach relies on W containing hard coatings.

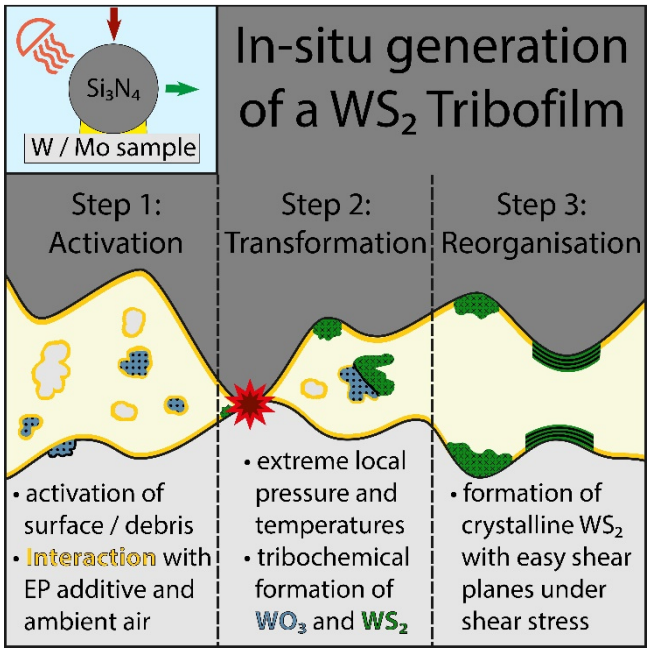

Figure 14: The proposed tribochemical reaction is separated into three steps (and works for W and Mo analogically). In the 3rd step, the initially amorphous WS_2 undergoes a shear stress induced self-organization [88, 131, 198].

We envision a new take on much needed [90] coating–lubricant synergies, slightly tailoring the coatings to boost their interaction with commercially available additives rather than developing new additives at great expenses. The friction reduction and wear protection is to be achieved via the in-operando tribochemical reactions as presented in **Figure 14**, which illustrates our concept on targeted tribofilm formation based on most desirable solid lubricants like MoS_2 or WS_2. To achieve these goals we investigate the fundamental mechanisms of the in-situ formation of these solid lubricants in rotating ball on disk tribological tests, as the point contact easily allows to reach high contact pressures as they often arise in non-conformal contacts and e.g. in geared wheels and rolling contact bearings. Applying this new knowledge enables us to tailor a Mo or W containing coating for an optimal in-situ lubrication. The S delivery system is based on an extreme pressure additive (40 at.-% S) in poly-alpha-olefin 8 (PAO 8) base oil (a synthetic oil for engines, transmissions, gears and pulleys). As a

reaction partner, transition metals are popular dopants for commercial coatings, but especially Mo and W also form interesting hard nitride coatings on their own. While Mo based systems proved crucial for uncovering the mechanism behind the reaction, due to the superior tribological properties of WS_2 in applications, our efforts in tailoring coatings are concentrated on tungsten nitride based hard coatings.

4.1 Following Breadcrumbs towards In-situ Solid Lubrication

Our investigations into the mechanism behind the in-situ formation started with unidirectional ball on disk tests (contact pressure: 0.5 GPa) of polished commercial Mo samples at 100 °C. To avoid any chemical interactions or analytical interferences of the counter body, all tests were performed with inert Si_3N_4 balls. Without the S-containing additive (pure PAO 8), the coefficient of friction on the Mo sample in **Figure 15a**, starts at around 0.18, slightly decreases to 0.14 in the run-in phase but stays well above the steel flat (AISI 52100) vs. Si_3N_4 ball reference (same COF for all S concentrations). The addition of 2 at.-% S in form of the sulfurized additive drastically changes the tribological behavior, lowering the COF to just below 0.05 after a run-in period, also contributing to a smoother and more stable run. The corresponding Raman Spectroscopy in **Figure 15b** can link the highly improved performance on Mo to the in-situ formation of the solid lubricant MoS_2 (see red line for 2 at.-% S).

In order to determine whether we can translate the results of a Mo surface to a chemically similar W surface we conducted similar tests with stepwise increased S content in the oil. While the friction is reduced to 0.1 by adding 0.6 to 2.0 at.-% S additive (no trend within this concentration-window), it does not reach the low friction level we would expect from a WS_2 lubricated contact. As evidenced by Raman Spectroscopy (**Figure 15b**) the W surface with its low chemical reactivity (compared

to Mo) does not facilitate the in-situ formation of dichalcogenides. Interestingly, X-ray photoelectron spectroscopy revealed that the Mo contact contained high amounts of oxides in the contact zone. For W, in comparison, the test conditions are not severe enough for oxidative attack on the surface. The absence of oxides in the W contact lead us to believe that the in-situ formation of both, MoS_2 and WS_2, is dominated by an oxidation pathway, in which the transition metal is first oxidized in a first step (Activation, **Figure 14**) and the oxide subsequently reacts with the S of the additive to form the respective disulfide (Step 2, **Figure 14**). A repetition of the tests on Mo surfaces in an O_2-free dry nitrogen atmosphere (**Figure 15a**) supports this suggested formation pathway, as the friction is significantly higher.

For verification of the reaction pathway, another set of W samples have been thermally annealed in air prior to testing. They provide a hex. WO_3 (P6/mmm) surface and were tested under the same conditions as the metallic samples. The COF for the oxidized W surface (**Figure 15a**) slightly decreases as the S content in the oil increases and shows a drastic drop to 0.05 as a certain threshold concentration is exceeded and in-situ WS_2 formation was enabled (confirmed by Raman in **Figure 15b**). The Raman investigations in both cases (Mo and W) also demonstrate that the lubricating effect is solely based on the formation of TMD and no oil derived lubricating carbon structures [91] are present. While the COF on the Mo sample experiences an exponential decrease due to an initial shortage of oxides, the pre-applied oxide educts are at instantaneous disposal on the annealed W surfaces, reducing the running in period to only a few cycles. The relationship between the availability of oxides and S is also highlighted by the run in period with 0.6 at.-% S and the significant rise in friction at the end of the test with 2 at.-% S. In both cases WS_2 was initially formed, but the unbalanced availability of educts lead to deprivation of one reaction partner and resulted in the termination of a sustained in-situ lubrication. Therefore, the in-situ lubrication relies on a competing process whereby the oxidation rate of the transition metal source and the availability of S need to be well balanced.

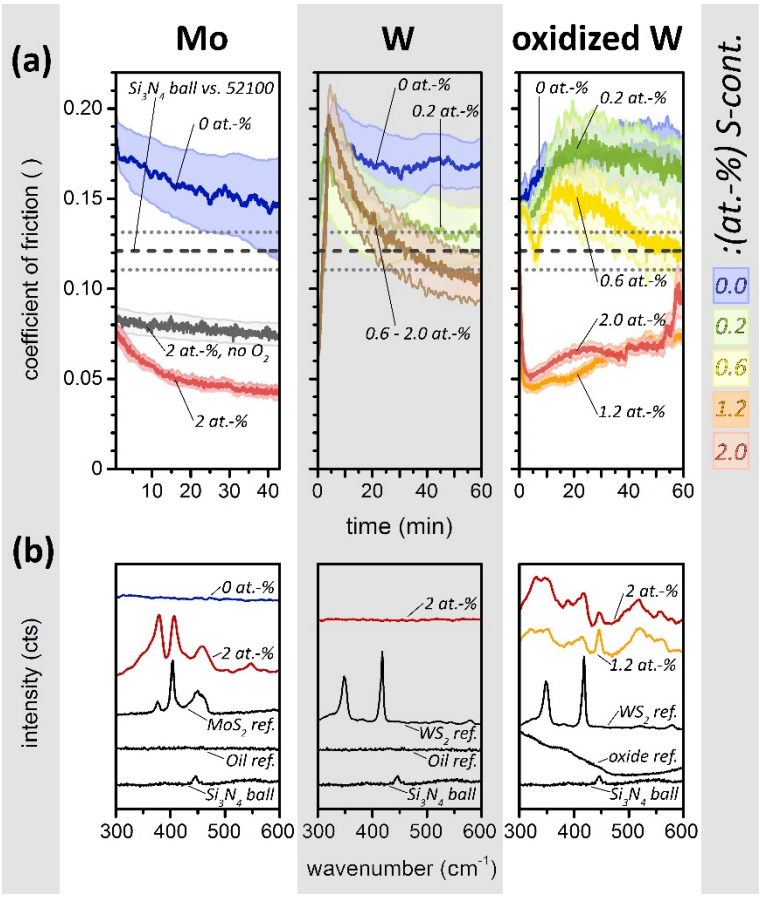

Figure 15: (a) Interactions of the Mo surface with 2 at.-% S in the oil lead to a drastic reduction of the COF. While metallic W surfaces do not follow this low friction behavior, a thermally annealed tungsten oxide surface demonstrate an immediate drop in friction at sufficient S concentrations in the lubricant. (b) The low COF for S-containing tests on Mo and oxidized W can be directly linked to the formation of MoS_2 and WS_2 respectively, via Raman spectroscopy of the wear scar on the counter body while on W no sulfide is formed.

For any application, low friction on its own is not the whole success story and might be easily achieved otherwise. The true value of WS_2 lies in its combination with excellent wear protection. As the tested bulk materials possess different mechanical properties, compatibility of the wear behavior is limited to investigations of the ball as counter-body. Tests without the S containing additive and tests in which no TMD

formation was sustained, present high abrasive wear on the ball (**Figure 16b**, **c** and **f**). The systems involving a Mo surface (**Figure 16a** and **e**) or an oxidized W surface (**Figure 16d and g**) in combination with the S additive on the other hand only experienced slight changes in the surface morphology (noticeable shining finish), without any measurable wear. This demonstrates the excellent wear protection properties of the in-situ formed MoS_2 and WS_2 tribofilm.

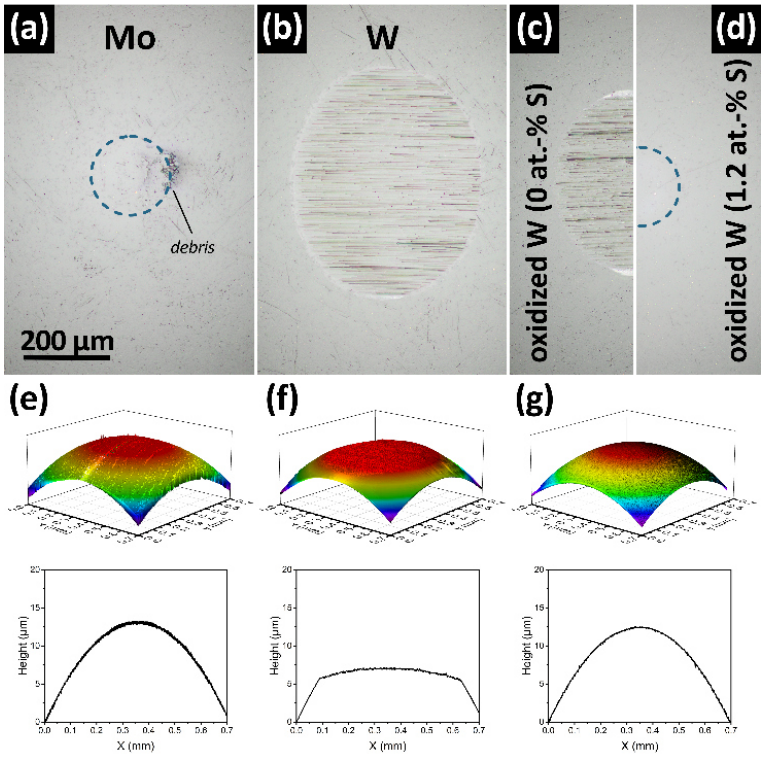

Figure 16: (a) The in-situ formation of MoS_2 offers excellent wear protection (e). (b) Tests on W surfaces lead to the formation of abrasive particles and (f) result in high wear on the ball. (c) A similar wear mechanism can be noticed on oxidized W surfaces without the presence of S. (d) The addition of 1.2 at.-% S to the contact sustains the formation of WS_2, leading to the same polishing as with Mo and averting any measurable wear (g).

4.2 Tungsten Nitride Coatings – the Key to In-situ WS_2 Formation

While MoS_2 was easily formed on metallic Mo surfaces, the generally more stable and better performing WS_2 needs additional modification of the W-delivery system to work. Therefore, tungsten nitride based coatings were applied to modify the surface oxidation rate (as the Gibbs free energy is less negative) and at the same time to benefit from synergetic protection of the surface by enhanced mechanical properties. This coating was produced with high power impulse magnetron sputtering, leading to a nano-crystalline morphology. It obtains a hexagonal sub-stoichiometric -WN structure (P63/mmc), a chemical composition of roughly 60 at.-% N and exhibits a hardness of 31 GPa (compared to 22 GPa of a metallic W coating). Further coating details are given in the supplemental information.

Putting the coating to the (tribological) test, **Figure 17a** shows that, unlike metallic W, the coating supports the in-situ formation of WS_2 (under the same conditions) and that the COF is lowered to a stable level between 0.04 and 0.05. Increasing the load and thereby the contact pressure initially demonstrates similar low friction behavior, but after the run in period the COF starts rising again until it levels out at 0.08. Raman spectroscopy of the contact area, **Figure 17b**, suggests that this is the result of the WS_2 tribofilm being worn away. The tribofilm is increasingly mechanically removed from the contact while the reaction constantly replenishes the WS_2 on the exposed surface. This leads to an accumulation of WS_2 based debris around the wear track, delivering a stronger Raman signal.

Without the S-additive, the contact is subjected to high wear of the ball (increasing with the contact pressure, **Figure 17c**), whereas any coating wear is below the detection limit. In presence of 2 at.-% S in the contact, tests that exhibit low friction also experience no wear. Unexpectedly, despite the elevated COF (0.08, at this level

tests with metallic W experienced high wear on the ball), the increased contact pressure does not lead to any measurable wear on coating or ball at all. The 3D images of the associated balls, **Figure 17d**, prove that although the removal of the tribofilm from the contact might hinder excellent lubricating properties at high loads, the wear protection of the in-situ formed WS_2 is still intact, preventing any measurable wear. The wear protection of the tribofilm and the coating at a contact pressure of 0.5 GPa also proves to be very reliable in long term tests, exhibiting no wear on either ball or coating after 100 hours of testing (see supplemental data in section 0).

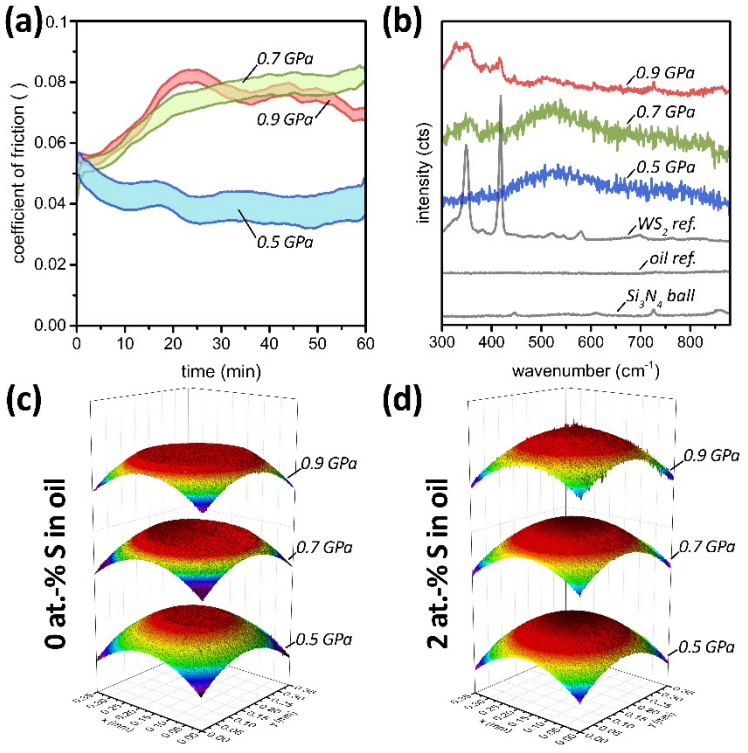

Figure 17: (a) Low friction via the in-situ generation of WS_2 can also be achieved by applying coatings in the presence of S containing additives. The evolution of the COF depends on the contact pressure, as the tribofilm suffers from higher loads. Raman spectroscopy (b) demonstrates that WS_2 has formed in higher amounts as the contact pressure increases. (c) Without any additive to react and form the WS_2 based tribofilm, the wear is quite severe and increases proportionally. (d) Although (despite the presence of the S containing additive), the COF increases for higher contact pressures, the wear protection capabilities are still excellent pushing the amount of wear below detectable levels.

The Si_3N_4 ball (**Figure 18a**) presents a small contact interface with a surrounding rim of relatively thick tribofilm at areas of lower contact pressure. Around the contact, accumulated debris (containing WS_2 and oil derived by-products) adheres to the ball surface. These deposits of debris also form outside of the wear track on the coated flat sample (**Figure 18b**), whereas the tribofilm itself is predominantly developing on the ball. Although no wear was measurable, the increased load leads to a rising buildup of debris as more tribofilm is worn away and continuously regenerated. This build-up also supports the concept of the in-situ formation of WS_2 as secondary ion mass spectroscopy investigations reveal that the tribofilm debris is rich in S (**Figure 18c**) while being oxygen-depleted (in respect of the surrounding surface oxidation, **Figure 18d**). The investigations also uncovered the WS_2 generation area in the center of the wear track where local oxidation generates the required tungsten oxides and the conditions are severe enough to facilitate the subsequent WS_2 formation.

The lubricating and protective effect of WS_2 requires the formation of easy slide planes, more precisely crystalline WS_2 sheets, emerging from the initially unaligned or amorphous reaction products. The main fraction of the tribofilm has an amorphous appearance in TEM (**Figure 19a**) and selected area diffraction (SAED).

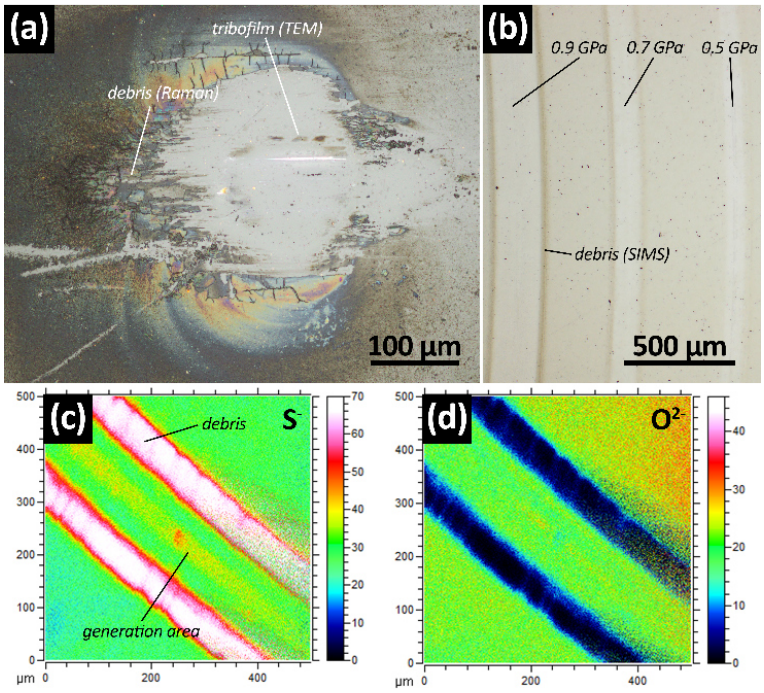

Figure 18: (a) The contact area of a ball at 0.9 GPa with 2 at.-% S exhibits no measurable wear and presents areas of accumulated debris (investigated by Raman spectroscopy, contains WS_2) and tribofilm, that has been investigated with TEM. (b) The coated flat does not show any measurable wear as well, but illustrates the formation of a debris zone around the wear track (intensifying with the contact pressure). This area was investigated with secondary ion mass spectroscopy (c) revealing a high concentration of S in the debris, while (d) oxygen species are absent from the debris.

Detailed high-resolution (HR) studies (**Figure 19b**) reveal that the lubrication, as envisioned, is in fact supported by the formation of crystalline WS_2 regions. Those nanocrystallites are only few nanometers in diameter and are roughly aligned in parallel to the interface. These regions are too small for SAED, but the spacing between the planes can be calculated (by Fourier transformation of HR image sections), which matches the distance between the easy shear planes of WS_2. Although the major part of the tribofilm is not crystalline, it still contains W and S in the ratio 1:2 according to EDX line scans (**Figure 19c**), ready to self-organize under shear forces in order to form a few nm thick easy-glide top-layer on the tribofilm.

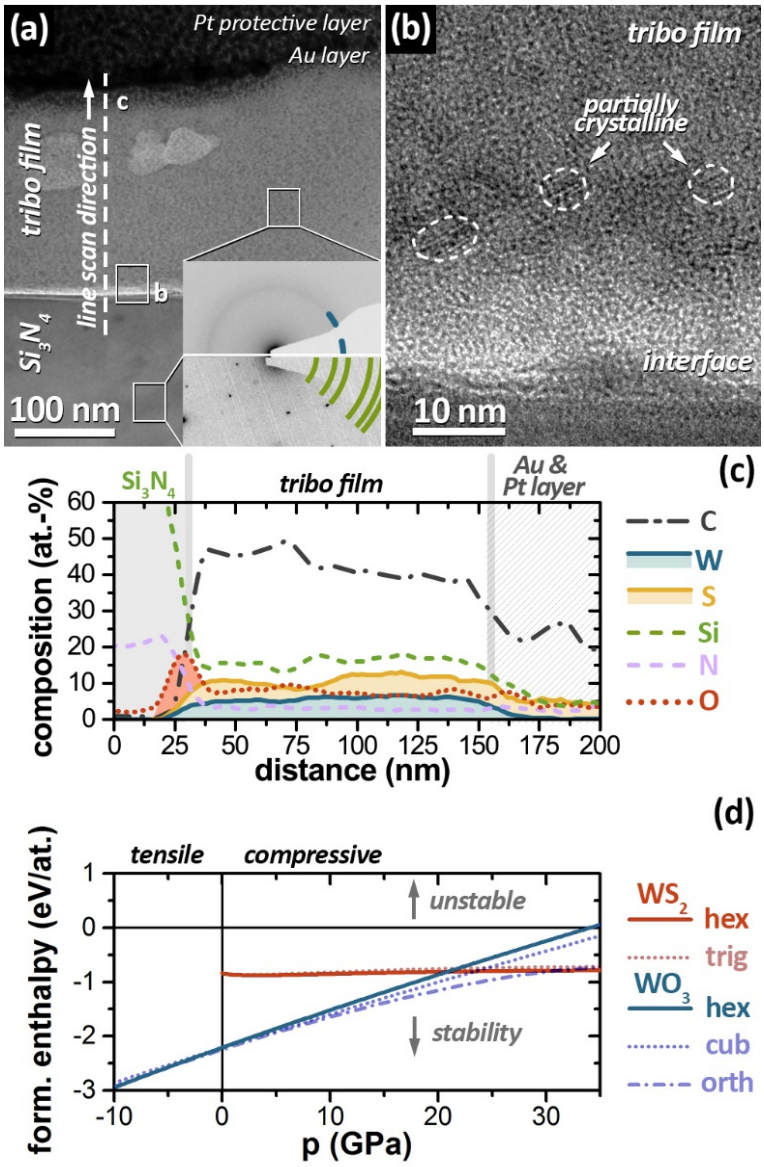

Figure 19: (a) The tribofilm (protected by an Au and Pt layer), that formed on the Si_3N_4 ball, was investigated with TEM and exhibits a mostly amorphous appearance. (b) In the tribofilm crystalline WS_2 nanoparticles are embedded. (c) The chemical composition (determined by EDX) across the tribofilm is dominated by amorphous carbon (from decomposed oil) and W as well as S in a 1:2 ratio. (d) The in-situ formation is also suggested by density functional theory calculations, which suggest that at increasing contact pressure the WS_2 becomes energetically more favorable than WO_3 which has formed in the contact.

The in-situ reaction undoubtedly produces WS_2, but it is unexpected that oxides are the key trigger to the formation. Considering normal atmospheric conditions, we would imagine the metal oxide to be the most stable compound. However, in tribological contacts the conditions tend to be more extreme and in order to truly understand a tribochemical reaction we need to investigate behavior of materials under these borderline conditions. From an energetic point of view, the formation of WS_2, with a standard Gibbs energy $\Delta_f G_m^\circ(293.15\ K)$ of $-232.1 \pm 3.1\ \mathrm{kJ \cdot mol^{-1}}$, is feasible [199] but in experiments it seems to be kinetically inhibited. While an oxidative environment in tribocontacts is common, it is surprising that stable oxides in combination with S compounds react further to form a less stable disulfide. First of all, the energy of formation for WO_3 increases with temperature until it becomes positive and decomposes. The free Gibbs energies for potential variations of in-situ reaction mechanism on the other hand decrease with rising temperature. Only the thermal decomposition of WS_2 hinders a pure thermodynamic explanation. Neglecting these phase transformations, high temperatures would energetically favor the WS_2 formation. As reported by *Polcar* et al., our experimental data confirms that a sufficiently high contact pressure is a major condition for the formation of crystalline WS_2 [131, 198]. Therefore, we studied the influence of pressure on the formation enthalpy with ab-initio density functional theory calculations (**Figure 19d**, details in the supplemental information in section 0). Much like high temperatures, the high pressure in single asperity contacts destabilizes tungsten oxides and in combination with local temperature bursts tips the scale in favor of the WS_2 formation.

4.3 Summary (Chapter IV)

The formation of WS_2 is a delicately balanced system between the availability of S and the oxidation rate of the W-supply, as the reaction predominantly takes the path of an initial oxidation and subsequent sulfide generation. Both, temperature and pressure, in the contact region of single asperities are severely higher than in the rest of the contact. These conditions enable the formation of WS_2 in the center of the wear track, which under these conditions becomes energetically more favorable than the oxide.

WN coatings play an important role, as they are applicable on all technologically relevant surfaces, add increased wear protection, and in comparison to metallic W facilitate the formation of WS_2.

The WS_2 is incorporated in the tribofilm on the counter face (ball) of the coating and self organizes under shear stress, forming lubricating nanocrystals. These nanocrystalline regions are reducing the COF significantly and offer excellent wear protection, with no measurable wear on either ball or disk after 100 hours.

While the tribofilm is continuously worn away under higher loads, leading to a COF only slightly below the reference, the formation of new WS_2 in the generation area is sufficient enough to sustain the wear protection. The in-situ formation of WS_2 allows to harmonize coatings and lubricants, and offers a synergetic and novel approach on long term wear protection.

4.4 Additional Information

The Following section provides additional information on the specific methods, used for this chapter as well as supporting additional data. It is not required for the understanding of this thesis. If no further details on the methods and additional prove for the statements of chapter 4 are required, it can be skipped and reading resumed with chapter 5 on page 77.

4.4.1 Specific Methods

This additional methods section gives detailed parameters (applied in chapter 4) in addition to the general overview in chapter 3.

4.4.1.1 Ball on disk tribological test

The tests were performed in an unidirectional rotating ball on disk setup and were carried out with a Nanovea T50 tribometer. All specimens were ultrasonically cleaned in two steps with acetone and n-heptane. They were tested against a 9.5 mm diameter Si_3N_4 ball, to avoid any chemical contamination with other transition metals or any catalytic effects of additional metal surfaces. The surface roughness (R_a) of the Si_3N_4 balls was 0.015 µm. The test temperature was 90 °C, which was controlled with a radiant heater and the relative humidity was measured at 40 %. The contact was lubricated with a PAO 8 mixture, who's S-content was adjusted between 0 to 2 at.-% with the extreme pressure additive Lubrizol LZ 5340 MW. 0.05 ml of oil were sufficient to cover the surface of the samples. At a constant sliding speed of 0.1 ms^{-1} (boundary lubrication), the elevated temperature and a contact pressures of 0.5 GPa, the parameters mimic conditions in common applications. The tests were carried out with 3 repetitions at different radii (0.5 mm apart), while the revolutions per minute were adapted to allow for a constant sample speed and test distance (360 m).

The Mo and W samples were polished to a roughness of R_a = 20 nm, while the coated samples were tested as deposited. The annealing of tungsten samples for the testing of a pre-oxidized surface was carried out in ambient air at 600 °C for 15 min and yielded an even WO_3 thermally grown oxide layer.

After the test, ball and disk were separated immediately and allowed to cool before the oil was removed with n-heptane. In order to conserve the tribofilm, the samples were cleaned only by submersing without any additional agitating or ultrasonic procedures. All samples were surveyed with optical microscopy (Olympus STM6) and an optical profilometer (Bruker, Contour GT).

4.4.1.2 Raman Spectroscopy of the Tribofilm

The n-heptane-cleaned samples were investigated, with a confocal Raman microscope (inVia Reflex, Renishaw) at a 50-fold magnification, directly after the tribological tests. The 633 nm laser was reduced to 30 % of its power, to avoid any heat induced reactions during the measurement. The Raman instrument was calibrated with an internal silicon standard, and commercial MoS_2 and WS_2 powders (99 %, Sigma-Aldrich) were used as a reference. The spectra were averaged over three individual measurements and recorded in a range of 150-2,200 cm^{-1}. In order to investigate the formation of lubricating carbon films, some measurements reached up to 3,200 cm^{-1}.

4.4.1.3 Deposition of the WN_x coating

In preparation for the coating process, polished AISI 5200 steel flats were cleaned in an ultrasonic bath with Acetone and subsequently with Ethanol. All coatings were prepared in a CemeCon coating chamber with a twofold rotating sample holder (giving the coating a multilayered look due to shadowing effects). To eliminate surface contamination an Ar ion-etching step was implemented directly before coating. The coatings were deposited from a W target (>99.5 %) in a high-power impulse magnetron

sputtering (HIPIMS) process by applying 4,000 W (9 W/cm²). The deposition was carried out at constant 270 °C and a total pressure of 0.4 Pa in an Ar/N_2 mixture (130/55 scccm, respectively).

4.4.1.4 SIMS Investigations of the Wear Scar

The SIMS measurements were performed on a TOF-SIMS5 (ION-TOF GmbH) equipped with a bismuth liquid metal ion gun (LMIG, primary gun), a dual source column (secondary gun) and a low energy flood gun.

The samples were measured in the high current bunched mode (HCBU) with approximately 16 nA target current in the non-pulsed state. This measurement mode provides the best mass resolution and maximum count rate. Bi_1^+ was used as the primary projectile. The region of interest (ROI) was set to 500 * 500 µm² at a resolution of 512 * 512 Px for the overview measurements.

The measurements in positive and negative ion mode were realized with two different projectiles, dependent on the enhancement effect.[1] A 2 kV O_2^+ beam with a sputter crater of 1000 * 1000 µm² was utilized for the detection of positive ions. For negative measurements, a 1 kV Cs beam with a sputter crater of the same size was set.

The measurements were performed in the non-interlaced mode with 1 acquisition frame, 1 s of sputtering and 0.5 s pause time. This separation of the analysis and the sputter cycle leads to an improved S/N ratio and generally speaking often to a higher data quality.

The floodgun provided about 15 µA of low energy electrons to effectively prevent charging of the samples. This is highly recommended for the used materials.

The pressure in the main chamber was approximately $3 * 10^{-8}$ mbar for the negative measurements. Due to the EI gas source for O_2^+ sputtering, also the pressure of the

main chamber was slightly increased to around 7 * 10^{-8} mbar.

4.4.1.5 TEM and EDX Investigations

The lamellas for TEM investigations were prepared using a FEI Quanta 200 3D DualBeam- focused ion beam. Specimens were coated with 4 nm gold and subsequently protected with a thin Pt layer in order to conserve the fragile tribofilm on the surface. Compared to the W based coating, the tribofilm is very fragile and was difficult to conserve. Therefore, the final thinning of the lamella was achieved by a 20 min ion polishing procedure using a Gentlemill (TechnoorgLinda).

Transmission electron microscopy investigations were performed with FEI TECNAI F20 operated with an acceleration voltage of 200 kV, which was equipped with an Apollo XLTW SDD EDAX detector for chemical analyses.

4.4.1.6 Hardness Measurements of the Coating

The coating hardness was determined with a UMIS Nanoindenter, equipped with a Berkovich diamond tip. The high surface quality of the coating allowed for direct measurements on the untreated as deposited coating. Indents were placed along a line with a distance of 20 µm and a load range of 3-45 mN. The indentation depths of individual indents for evaluation were kept below 10 % of the overall film thickness to avoid substrate interference [200]. The load-displacement curves were evaluated according to Oliver and Pharr [201]. To achieve a representative hardness, three individual measurements with minimum 40 indents each were consolidated and evaluated.

4.4.1.7 XRD Investigations of the Coating

The phase structures of the coating were investigated by x-ray diffraction with a Panalytical Empyrean diffractometer in the Bragg-Brentano configuration. The

measurements were carried out with Bragg-Brentano HD mirror, a 0.04 rad soller slit, a fixed 2° Ta anti scatter slit and a divergence slit of ½°. The diffractograms where evaluated with HighScore (Panalytical) and a PDF-4+ 2018 database (ICDD).

4.4.1.8 DFT Calculations on the In-situ Formation

The calculations were performed using the Density Functional Theory (DFT) as implemented in the Vienna Ab initio simulation package (VASP) [202, 203] together with the projector augmented plane wave (PAW) pseudopotentials under the generalized gradient approximation (GGA) [204] and the Perdew-Burke-Ernzerhof (PBE) exchange correlation functional [205]. The plane-wave cutoff energy was always set to 600 eV and the reciprocal space was sampled with Γ-centered Monkhorst-Pack meshes [206] equivalent to at least 25 000 k-points atoms. All systems were converged to about 10^{-3} eV/at.

Table 1 provides structural description of the phases of WN, WC, WS_2, and WO_3 considered in our study. Equilibrium lattice parameters of all systems were obtained by fitting the minimum of the energy vs. volume curve with the Murnaghan equation of state [207]

$$E(V) = E_0 + \frac{B_0 V}{B_0'}\left(\frac{(V_0/V)^{B_0'}}{B_0' - 1} + 1\right) - \frac{B_0 V_0}{B_0' - 1} \tag{10.1}$$

where the parameter E_0 denotes the total energy of the system at equilibrium volume V_0, while $B_0$and B_0' are the corresponding bulk modulus and its pressure derivative at the reference state of zero pressure.

In order to analyze the pressure effect on the stabilities of WN, WC, WS_2, and WO_3 polymorphs, we calculate their formation enthalpies

$$H_f(p) = \frac{1}{\sum_s n_s}\left(H_{tot}(p) - \sum_x n_s \mu_s\right) \tag{10.2}$$

where $H_{tot}(p)$ is the enthalpy of the system, n_s and μ_s are the number of atoms and the chemical potential, respectively, of a species s. The reference chemical potentials for C, S, and W are conventionally set to the enthalpy per atom of graphite-C, μ_C, orth-S, μ_S, and bcc-W, μ_W, while the N_2 and O_2 molecules, represent the chemical potential of N, μ_N and O, μ_O. The total enthalpy in the above Eq. 2 reads

$$H_{tot}(p) = E(p) + pV(p) \tag{10.3}$$

Using the definition of pressure, $p = \partial E/\partial V$, formulas for $V(p)$ and $E(p)$ can be derrived from Eq. 1 and plugged in Eq. 4, therefore,

$$H_{tot}(p) = E_0 + \frac{B_0 V_0}{B_0' - 1}\left(\frac{(p/B_0) + 1}{\sqrt[B_0']{(B_0'/B_0)p + 1}} - 1\right) + p\frac{V_0}{\sqrt[B_0']{(B_0'/B_0)p + 1}} \tag{10.4}$$

Since the reference chemical potentials for C, S, and W are related to the enthalpies of their

crystalline phases which do depend on pressure through the Murnaghan equation 1, we also consider μ_C, μ_S, and μ_W in Eq. 2 to vary with pressure, analogically to the binary systems. Following the argumentation of Reuter and Scheffler [208], the μ_N and μ_O chemical potentials are kept constant irrespectively of the pressure, due to the fact that our DFT calculations are performed at 0 K.

Table 1: Crystal symmetry classes and space goups of the here considered phases of WN, WC, WS_2, and WO_3 together with the calculated lattice parameters, a and c.

System	Symmetry	Space group	a(Å)	a^{ref}(Å)	c (Å)	c^{ref}(Å)
WN	cubic	$Fm\bar{3}m$	4.369	4.357 [96], 4.362 [209]		
WN	cubic	$Pm\bar{3}m$	4.133	4.120 [210], 4.125 [96]		
WN	hexagonal	P_6m2	2.877	2.865 [209]	2.912	2.912 [209]
WC	cubic	$Fm\bar{3}m$	4.394	4.398 [209]		
WC	hexagonal	$P\bar{6}m2$	2.931	2.926 [209]	2.853	2.849 [209]
WS_2	hexagonal	$P6_3/mmc$	3.201	3.153 [211]	14.349	12.323 [211]
WS_2	trigonal	R3m	3.197	3.158 [211]	21.880	18.49 [211]
WO_3	cubic	$Pm\bar{3}m$	3.840	3.84 [212]		
WO_3	hexagonal	P6/mmm	7.475	7.298 [213]	3.840	3.899 [213]
WO_3	tetragonal	P6/nmm	5.368	5.36 [212]	3.996	4.01 [212]

4.4.2 Supplemental Information

Additional information on the applied tungsten nitride can be found in **Figure 20** (structural) and **Figure 21** (mechanical properties). The full results of the DFT calculations are summarized in **Figure 22** and the long-term test of the tungsten nitride coating is displayed in **Figure 23**.

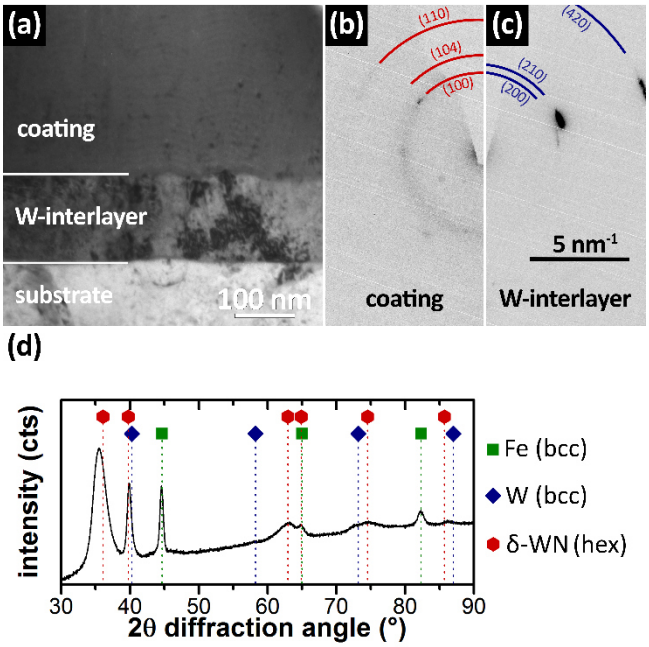

Figure 20: (a) The HIPIMS sputtered coating is comprised of a W interlayer and a tungsten nitride based nanocrystalline topcoat. The metallic interlayer acts as bond coat and compensates the dissimilar mechanical properties of substrate and coating. Due to the biaxial sample rotation while sputtering (with one cathode) the growth rate fluctuates periodically giving the coating a multilayer-like appearance in transmission electron microscopy (TEM) images. While the actual coating appears to be of nanocrystalline to amorphous structure in images, selected area diffraction (SAED) in (b) reveals its hexagonal δ-WN structure (with a N content of roughly 60 at.-%). (c) The interlayer predominantly grows with a 100 orientation. (d) X-ray diffraction confirms the hexagonal δ-WN structure of the coating on top of the steel substrate and the W interlayer. The overall phase fraction of metallic W was obtained by Rietveld refinement and is in agreement with the amount of W we were expecting from an interlayer of this thickness. Concluding, that the topcoat is free of a metallic phase fraction.

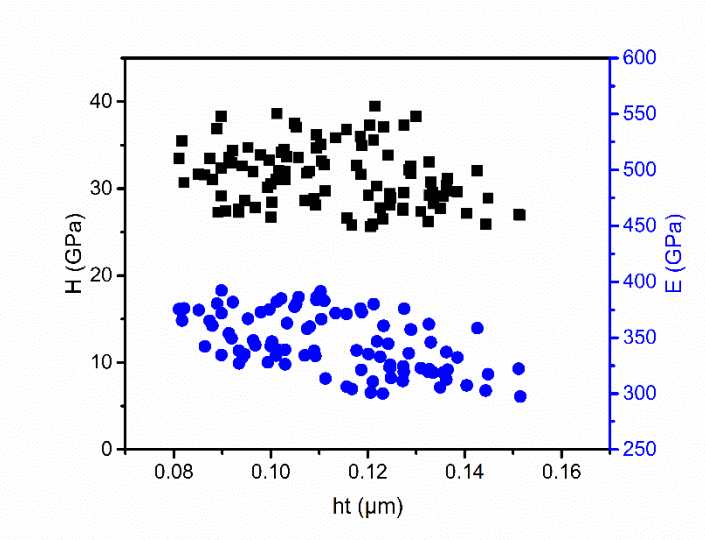

Figure 21: The hardness H of the coating did not decrease with the penetration depth ht and was 31 ± 3 GPa, whereas the indentation modulus E was 350 ± 25 GPa.

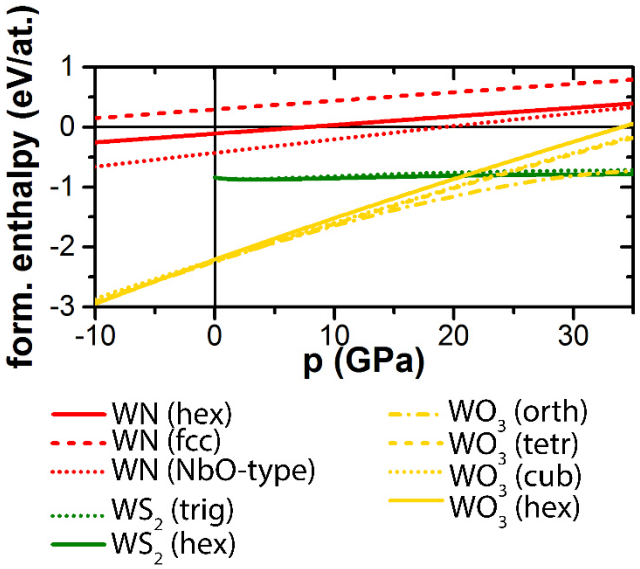

Figure 22: DFT calculations (VASP) demonstrate the increasing formation enthalpy for WN and WO_3 with increasing pressure, whereas the formation enthalpy of WS_2 remains constant, making it energetically more favorable at high pressures. At the same time, the formation enthalpy of WN also highlights why the coating is so beneficial to the formation of WS_2.

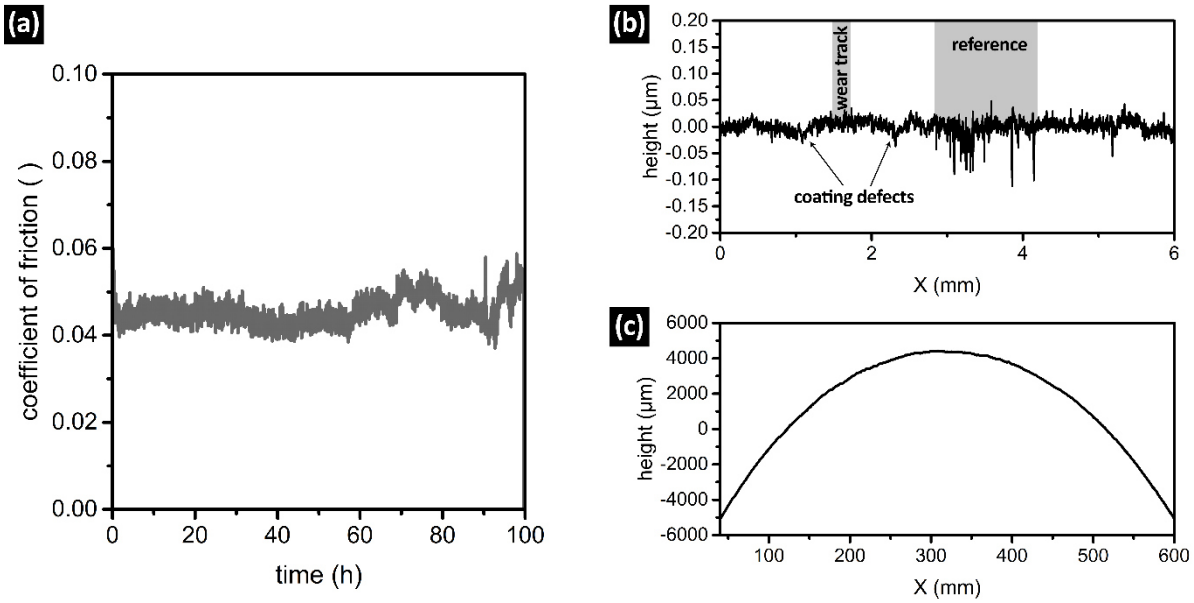

Figure 23: The long term performance of the coating in combination with the S-containing lubricant at 100 °C and a contact pressure of 0.5 GPa is excellent. For verification of the results long term tests have been performed with a second Nanovea micro tribometer at another institution. (a) The COF remains at very low levels around 0.05 even after 100 h. (b) Even after 100 h of testing, no wear on the coating can be detected in a radial line scan or with microscopy. It is important to mention that the two areas with reduced height can clearly be linked to preexisting coating and sample defects. As a comparison, for the appearance of a worn coating and to reference the location of the undetectable wear track, an additional track with excessive force was introduced. (c) The ball shows no measureable wear after 100 h of testing as well.

5 Reactive Self-assembly of MoS_2 for Low Friction

In modern engineering, synergies between coatings and lubricants are getting increasingly important. To reach environmental goals, a maximal reduction of friction and wear is imperative and leads to the use of ultra-low viscosity oils. Especially in these boundary-lubricated regimes, the formation of protective tribofilms is a key aspect of long duty periods. Commercially prevailing additives for tribofilm formation are subjected to heavy scrutiny due to environmental concerns, and 2D materials like MoS_2 and Graphite are closing in as potential replacements.

The importance of tribofilms in boundary lubrication has long been understood and lead to the development of conventional lubricant additives like zinc dialkyldithiophosphates [73]. Although ZDDP offers good wear protection in boundary lubrication [68, 72] and many other beneficial characteristic to lubricants, it is earmarked for replacement due to negative environmental concerns [74]. Adding to the necessity, to develop new tribofilm formation methods, is the trend towards lightweight materials and partially coated machine elements, rendering many established additives inefficient due to their reliance on ferrous surfaces.

Over the last years, new approaches started focusing on active surface as the key to low friction and good wear protection. Instead of additives, surfaces themselves are essential to the tribofilm formation and the lubricant is reduced to a more passive role.

These surfaces are often thin films and, for instance, are capable to catalytically modify [214] the surrounding medium in order to produce oil derived diamond like carbon types of tribofilms during application [91, 93]. Other specialized surfaces are designed to chemically react with additives in order to generate lubricating species, mostly based on 2D materials like transition metal disulfides or graphene [92] (chapter 4). One of the tribological most relevant 2D materials is MoS_2, with its S-Mo-S sandwich structure that allows for low friction shear between its lattice planes [121, 123, 215] or single MoS_2 sheets [77]. While lubrication with MoS_2 (or also WS_2 [88])can be based on various coatings [130, 131, 133], it is also possible to add it to lubricants in form of nanoparticles [79, 81, 84, 196, 215, 216] or generate lower concentrations in-situ with the molybdenum dithiocarbamate or similar additives [76-78, 217]. In the 90ies, first studies with Mo surfaces in H_2S containing atmospheres suggested lubricating interactions with S species [53, 54, 218, 219]. Later on, with the commercial success of W doped DLC coatings, their synergies with S containing additives were investigated and uncovered the formation of protective W and S containing tribofilms [197, 220-223]. Based on these studies, we were able to demonstrate the formation of WS_2 on W containing coatings and highlight the importance of oxygen availability for this tribochemical reaction (chapter 4). While this study focuses on commercially available extreme pressure additives as S delivery system, the in-situ formation of MoS_2 or WS_2 can also be achieved with more ecofriendly S containing molecules such as allyl disulfide or the amino acids cysteine and methionine [12, 89]. The in-situ formed MoS_2 in the tribofilm is most likely initially of an amorphous structure. Investigations of sputtered amorphous MoS_2 thin films have shown that under shear stress and at elevated temperatures MoS_2 can self-assemble to form lubricating sheets [88, 198].

Although W and Mo behave very similar from a chemical point of view, the MoS_2 formation on metallic Mo occurs at much milder conditions than the equivalent

reaction on W (chapter 4). Therefore, to gain a better understanding of the impact of different system temperatures and additive concentrations on the tribochemical formation, metallic Mo disks were selected as reactive surfaces. Here, the potential reactivity of the counter body is addressed as well, by comparing a potentially reactive counter body (iron based) to an inert Si_3N_4 ceramic.

The reaction of S with the Mo surface inevitably involves residual hydrocarbon fragments. While the formation of DLC like tribofilms was so far studied on Cu-doped coatings [91] and Pt-Au alloys [93], many more metals are suspected to possess tribocatalytical properties, including Mo.

The aim of this work is to investigate the interaction of hydrocarbon oil and EP additives on Mo surface for understanding the kinetics of the tribochemical reaction as well as the structure of the tribofilm, with the goal of exploiting the knowledge in engineering relevant systems.

5.1 Methods

A forged molybdenum rod with a purity of 99.97 % (Plansee AG, Austria) and a 25 mm diameter was cut into discs of 7 mm thickness. The Mo samples had a hardness of 230 HV 10 and a Young's modulus of 330 GPa. Bearing steel balls (AISI 52100) with a diameter of 10 mm and a hardness of 63 HRC were used as counter body. Selected samples were investigated against Si_3N_4 balls (grade 5) with a diameter of 10.3 mm.

The lubricant used was poly-alpha-olefin oil 8 with a viscosity of 45.5 and 7.9 mm^2s^{-1} at 40 and 100 °C, respectively. In order to promote the formation of MoS_2 during rubbing, the oil contained different concentrations of sulfurized olefin polysulfide (Lukoil Lubricants Europe, Austria), ranging from 0 to 5 wt.-%. This organic

compound with a S content of 40 at.-% is typically used as extreme pressure additive in formulated lubricants.

The tribological experiments were performed under a reciprocating sliding contact using an SRV tribometer (Optimol, Germany). The reciprocating frequency was set to 10 Hz and the oscillation amplitude to 1 mm. Throughout the experiment, the normal force was set to 10 N resulting in an initial contact pressure of 0.7 GPa and 8.5 GPa for the steel and ceramic ball, respectively. The reference tests were performed isothermally at 100 °C. Additional tests at temperatures ranging from room temperature up to 130 °C were performed in order to investigate the role of the system temperature on the formed tribofilm chemistry. For each combination, three independent measurements were conducted and averaged.

The tested samples were gently rinsed with n-heptane before the Raman analyses to remove residual lubricant without damaging the tribofilm. The presence of C and MoS_2 was investigated using a LabRam ARAMIS (Horiba, Japan) Micro-Raman spectrometer. The samples were excited with a 532 nm wavelength laser, set to a laser power of 2 mW. The spectra were acquired over a spectral range from 100 to 3200 cm^{-1} with a 1200 gmm^{-1} grid.

High resolution analyses were performed using a TECNAI F20 field emission transmission electron microscope (FEI, USA) with an acceleration voltage of 200 kV in imaging, diffraction and scanning mode. Prior to the analyses, the samples were protected with a Pt layer and subsequently, a lamella was milled perpendicular to the sliding direction using a Quanta 200 3D DualBeam focused ion beam (FEI, USA). Since S-K lines overlap with Mo-L lines in EDX spectra, electron energy loss spectroscopy was used to determine the chemical composition of interesting sample areas. The loss spectra were obtained on a GIF Tridiem (Gatan, USA) and quantified on the core losses at energies of 165 eV and 227 eV for the S-L2,3 edge and the Mo-M4,5 edge, respectively.

5.2 Results and Discussion

Reciprocating sliding ball on disk test with Mo surfaces against AISI 52100 balls at 100 °C, in **Figure 24a**, show a drastic reduction of the coefficient of friction for lubricants with the EP additive. The general levels of friction are consistent with previous tests under similar load (chapter 4). Raman spectroscopy in **Figure 24b** can clearly link the reduced friction to the in-situ formation of lubricating MoS_2. For MoS_2, a Raman shift of 383 cm^{-1} (for the in-plane E^1_{2g} mode) and 408 cm^{-1} (for the A_{1g} mode) are expected [224], whereat the absence of a shift of those peaks to lower and higher wavenumbers, respectively, suggests a low number of stacked layers. Nanoparticles of MoS_2 (which we are expecting) have been reported [225, 226] to yield broader peaks with a higher full width at half maximum (FWHM), but this would also be connected with a general downshift of the signals, which cannot be noticed in our spectra. At the same time, partially overlapping signals from FeS_2 (342, 378 and 429 cm^{-1}) [227] cannot be responsible either, since the absence of a peak at 342 cm^{-1} suggests that only insignificant amounts of FeS_2 are present (FeS neither). As a result, we contribute the broad peaks to reduced crystalline order. In highly oriented MoS_2 thin films a broad peak emerges around 445 cm^{-1}, which is not the case for our tribofilm [228]. This defected crystalline order can also be seen in the peak structures at low wavenumbers around 227 cm^{-1}, where the broken crystal symmetry can activate (due to the Raman selection rules) Raman-inactive modes, giving this distinct pattern [225, 226]. A similar behavior can also be found in graphitic carbon materials [229, 230].

In addition to the lower friction level, the MoS_2 containing tribofilm also leads to a slightly smother run with a lower standard deviation (**Figure 24a**). The increasing intensity of the MoS_2 Raman signals with increasing EP additive content demonstrates that more disulfide is formed. At the same time, the initial run-in period (until a stable low friction is reached) decreases proportionally, as reaction rates are concentration

dependent. Molybdenum oxide, which is formed in tests without the EP additive are consumed by the in-situ MoS_2 formation in tests with EP additive, as the dominant reaction pathway relies on oxide intermediates (chapter 4).

Interestingly, the contact area of tests without the addition of EP additive showed a dark discoloration. Peaks at 1379 and 1587 cm^{-1} in the Raman spectra (**Figure 24b**) unmistakably prove the dark substance to be carbon based with its characteristic D and G band, respectively. The position of the G band and the I_D/I_G ratio suggest that the amorphization lies in stage 1 (graphite to nanocrystalline graphite) or stage 2 (nanocrystalline graphite to hydrogenated amorphous carbons) according to Ferrari and Robertson [231]. The absence of a G' band around 2700 cm^{-1} places the dark C based substance [231] clearly in stage 1 and therefore is based on sp^2-bonded carbon. A small fraction of C-H bonds can be noticed at 2900 cm^{-1}. The Raman spectra of the black debris matches spectra of typical DLC coatings and are in high agreement with the results of tribofilms, produced on MoN_x–Cu coatings by *Erdemir* et al.[91]. It is evident that the metallic Mo surface in the tribocontact is catalytically active and enables the formation of oil derived C-based tribofilms.

Low levels of C-based structures can also be detected in tribofilms with S containing EP additives. The intensity ratios of MoS_2 to C-based compounds suggest that the formation of MoS_2 and graphite are competing effects, with MoS_2 having the upper hand. It is noticeable that the intensity of the G band of tribofilms with EP additive increase with the EP additive concentration. We contribute this to the fact, that during decomposition of higher additive concentrations for the reaction between S and the Mo surface, increased amounts of carbon based residual fragments are produced, which can further be broken down and reassembled at lower energy input than whole hydrocarbons. The formation of MoS_2 accomplishes conditions which do not allow for a high significant breakdown of hydrocarbons.

In comparison to hard coatings, that have been studied in other works, the ductile Mo sample has a low hardness and the wear is considerable, leading to the formation of groves and micro-plowing. The ductile metallic surfaces of either steel or Mo most likely do not provide a stable base to support the formed C-based tribofilm, which cannot unfold its lubricating capabilities. Most of the tribofilm is buried in surface faults or worn away and deposited in the surrounding debris. This debris deposition can also be seen in the Raman of different areas in and around the contact zone of a test with 3% EP additive (**Figure 24c**). **Figure 24d** displays the wear track of the corresponding Mo sample and shows the generation of these deposits in the axial extension of the wear track, which itself can be segmented into darker tribofilm-covered and brighter metallic regions. Accordingly, the Raman signals display a higher intensity for the debris and tribofilm area. The adhesion to the surface appears to be better for MoS_2 based tribofilms as it, in contrast to the C-based tribofilm (which is mostly worn away and deposited outside the wear track), can still be detected on metallic areas of the immediate contact zone.

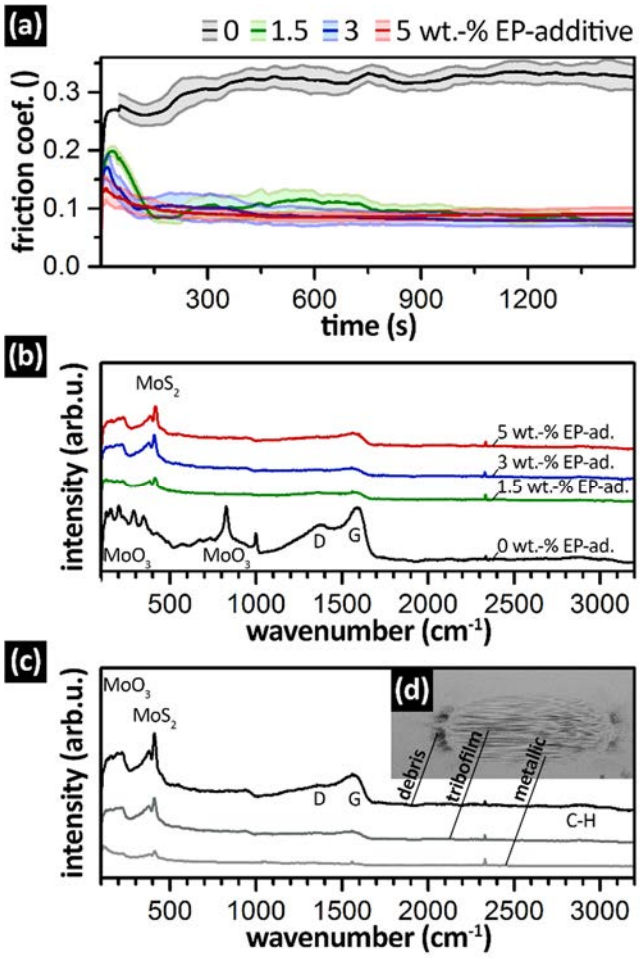

Figure 24: Influence of the EP additive concentration. (a) Development of the coefficient of friction over time with a steel ball at 100 °C (b) Raman spectra of the corresponding tribofilms (c) comparison of Raman peak intensities according to the position of the (d) measured region

An elevated reaction temperature has a huge beneficial influence on many (not necessarily endothermal) chemical reactions. Thermal energy helps to reach activation energies and overcome kinetic inhibitions. In case of the MoS_2 formation, the sample temperature has a clear influence on the tribological properties of the tribofilm, as evidenced by **Figure 25a**. Tests at 130 °C (3 % EP additive) exhibit an extraordinary stable and reproducible low coefficient of friction around 0.08. Although the coefficient of friction for tests at 23 and 40 °C is considerably higher than at higher temperatures, the consistent intensities of the MoS_2 peaks in the tribofilm's Raman shift (**Figure**

25b) suggest that there is no considerable difference in the formation of MoS_2. A difference of this extent however cannot be explained by oil viscosity differences as well. We suppose that the increased temperature and therefore higher diffusivity enhances the self-assembly of the initially amorphous MoS_2 [198]. During sliding, MoS_2 sheets are being detached and defects will be introduced into the sandwich structure. Hence, the elevated temperature is key to the self-mending process, which allows for very stable and reproducible low friction.

Unlike for the formation of MoS_2, increasing temperature appears to promote the formation of graphite like structures and contribute the necessary activation energy despite the reduced general energy input due to MoS_2 lubrication. It should be noted that reduced oil viscosity at elevated temperatures increases single asperity contact and therefore most likely leads to localized intensified conditions, supporting tribochemical reactions as well.

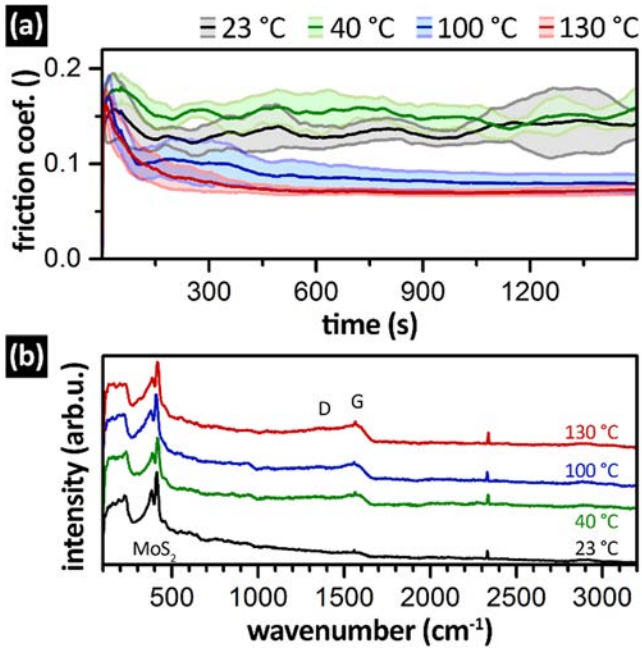

Figure 25: Influence of the contact temperature at 3 % EP additive. (a) High temperatures lead to lower friction and (b) stronger C-based signals in Raman spectroscopy.

To re-create more severe conditions in the direct contact zone we chose to repeat selected tests with a ceramic Si_3N_4 ball. This not only eliminates any possible catalytic effects from the iron surface, but at the same time also provides a counter body with superior mechanical properties that will experience much less wear and hence allow a higher contact pressure over a longer period. As a result, (with Si_3N_4 balls) low friction is achieved after only a few cycles of testing and the coefficient of friction remains much more stable and reproducible once it has reached its steady state, see **Figure 26a**. Even lower temperatures result in a stable low friction regime. In case of high temperatures with a Si_3N_4 ball, the combination of a ductile Mo sample and the higher contact pressure lead to increased wear of the sample with sever micro-pitting. Over time, this surface damage leads to a coefficient of friction around 0.1 although it initially started at 0.05.

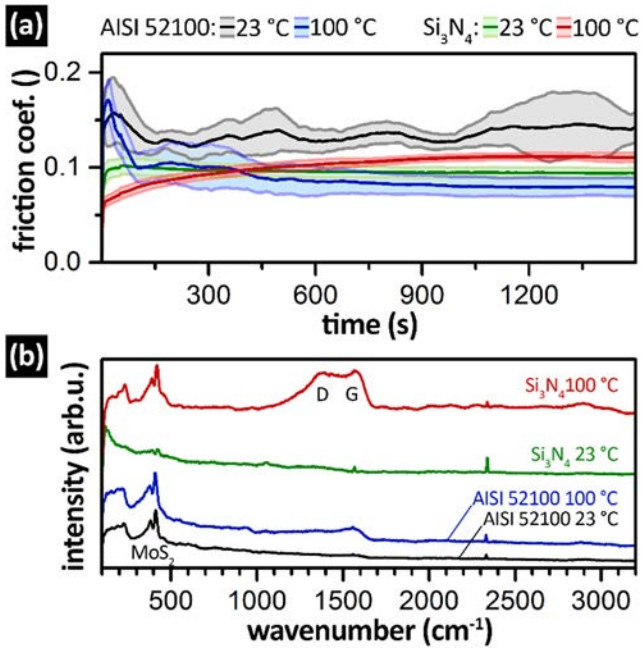

Figure 26: Influence of the counter body at 3 % EP additive. (a) Si_3N_4 counter bodies lead to very stable runs at low friction. (b) At 100 °C with Si_3N_4 ball, high amounts of carbon are formed.

As already mentioned, elevated temperatures boost the formation and self-assembly of MoS_2 significantly. Interestingly, Raman spectra show that the MoS_2 formation at room temperature with a Si_3N_4 ball is significantly lower than for steel balls (**Figure 26b**). Yet, the friction for the Si_3N_4 ball is well below the levels of the steel ball. We contribute this to the harder Si_3N_4 counter body, which experiences significantly less wear than steel balls and therefore produces a much smaller wear scar without grove formation on the Mo surface. On top of that, the Si_3N_4 ball offers a much more stable substrate to the tribofilm. As a result, much less MoS_2 is needed to efficiently lubricate the smaller contact and in return, under these well-lubricated conditions less MoS_2 is being formed to replenish the tribofilm.

Higher contact temperatures, resulting in: higher reaction rates, lower oil viscosity and higher single asperity contact, overall increase tribofilm removal and hence a heightened MoS_2 reproduction (even for a Si_3N_4 ball). These conditions at the same time are severe enough to increase the formation of oil derived C-based phases again. At this point it is not certain, what role the coverage of the Mo surface with MoS_2 plays. Further research would be required in order to determine whether the formation of C-based phases is simply a result of the higher energy input, or if the increased wear leads to a higher area of exposed Mo surface and therefore, to a higher catalytically activity. Although MoS_2/graphene heterostructures have previously been investigated for superlubricity [115] we suspected, that the self-assembly and recovery of MoS_2 sandwiches is obstructed by the presence of the *sp*2-bonded C structures. Consequently, the peak at 227 cm^{-1} in the Raman spectrum (**Figure 3b**, red line) is significantly higher and more defined. Whether this mechanism or the aforementioned micro-pitting are responsible for the increasing friction with the Si_3N_4 ball at 100 °C cannot be differentiated at this point.

The structure of the tribofilm, formed with 3 % EP additive and a steel ball at 100 °C can be investigated in **Figure 27** and **Figure 28**. A scanning TEM survey image of the cross-section (perpendicular to the sliding direction) in **Figure 27a** shows the accumulation of wear debris and tribofilm in groves on the Mo flat. The grooved surface exhibits stress induced grain refinement of the interface-near bulk material. A significant amount of micro-plowing leads to the buildup of thick-layered Mo structures next to the groves. Individual layers are separated by tribofilm inclusions. On top of the exposed Mo surface a tribofilm of up to 50 nm (**Figure 27b**) is formed. An EELS line-scan across the tribofilm (**Figure 27b**) shows that the tribofilm is predominantly based on carbon residue with embedded Mo particles. While some of the Mo particles are purely metallic, most of them coincide with rising S concentrations, suggesting that they partially reacted with the S from the EP additive. A further clue about the reaction is given by the C-rich areas of the tribofilm that do not contain any S and therefore rule out residual oil. While a rather newer tribofilm on top of the surface is predominantly C and Mo with only up to 5 at.-% of S, older tribofilm debris that experienced more sliding before being worn away and deposited in groves have a much higher S content (**Figure 27c**) and therefore a significant amount of formed MoS_2.

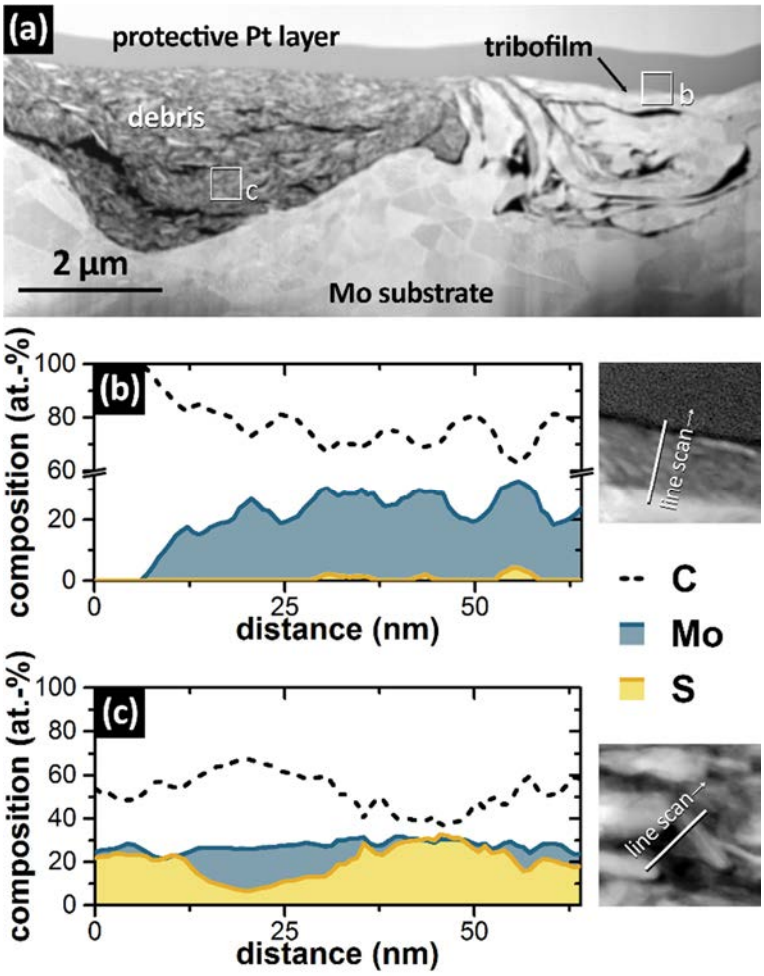

Figure 27: Chemical composition of the tribofilm in a Mo Vs steel contact at 100 °C with 3 % EP additive. (a) Scanning TEM overview of the FIB cross-section (b) chemical composition of a young surface near tribofilm obtained by EELS (c) chemical composition of older tribofilm debris.

To investigate the structure of the tribofilm in general and the generated MoS_2 in particular, HR TEM investigations (**Figure 28**) were carried out in the region of the debris accumulation and fold inclusions. A selected area diffraction pattern in **Figure 28a** uncovers that the debris consists of three crystalline phases: Mo debris from the sample, Fe debris from the counter body and a strong MoS_2 fraction. The latter, is of nanocyrystalline appearance with diffraction rings, compared to the macro-crystalline metallic debris with well-defined diffraction spots. Only few Fe crystallites could be detected and although S based EP additives are known for their interaction with Fe

surfaces, no measurable amounts of iron sulfides can be found in the tribofilm debris. It appears that the affinity of Mo for a tribochemical reaction with the EP additive prevents the formation of high friction iron sulfides.

HR images of the tribofilm inclusion between micro plowing layers in **Figure 28b** show an initially amorphous appearing young tribofilm, but detailed studies uncover a formation of small crystallites (with a lattice spacing of 2.66 Å) that can be associated with MoS_2 (2.73 Å). Fourier transformations of tribofilm image segments also exhibit a MoS_2 diffraction pattern.

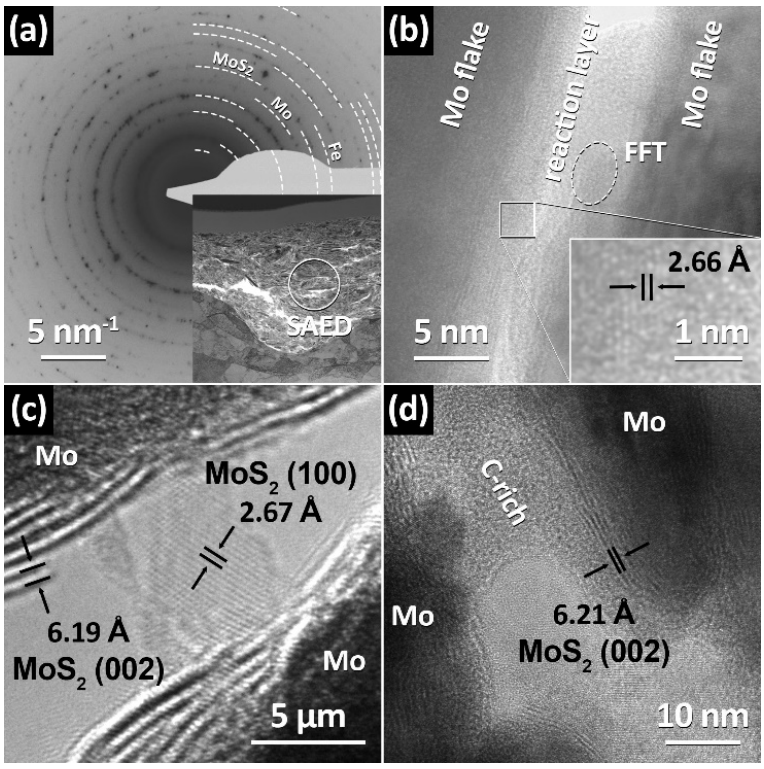

Figure 28: HR TEM images of the tribofilm (Mo vs. steel, 100 °C, 3 % EP additive). (a) SAED pattern of the debris area (b) HR image of a young tribofilm (c) MoS_2 sheets formed on top of Mo debris (d) MoS_2 sheets are covered by a layer of residual carbon.

We now understand, that MoS_2 is in fact formed within the contact, but to better understand the lubricating effects it is necessary to better understand the detailed structure of the in-situ formed MoS_2, as the self-assembly to parallel oriented sheets is essential. We found the answer to that question in HR images, back in the debris area, in **Figure 28c**. A few atom layer thin flake of MoS_2 allows for a precise measurement of the lattice spacing (2.67 Å) which coincides with the expected 2.73 Å. It is clearly noticeable that Mo surfaces have reacted with S from the additive and formed stacked S-Mo-S sheets with their (002) basal plane parallel to the underlying Mo. These MoS_2 structures can also be discovered in annealed initially amorphous thin films [228] and are perfectly aligned to allow easy slippage between contacting bodies. With 6.19 Å, the sandwiches match the theoretical lattice spacing of 6.15 Å perfectly. These MoS_2 sheets are located directly at the Mo to tribofilm interface, with the C-rich amorphous residue forming a layer on top of them. **Figure 28d** demonstrates the MoS_2 sandwiches following the form of the particle, perfectly aligned to allow for low friction.

5.3 Summary (Chapter V)

Molybdenum surfaces can facilitate the in-situ formation of lubricating MoS_2 and at the same time are able to catalytically decompose base oil molecules in order to form *sp*2-bonded C-based tribofilms. Although Mo samples are of poor mechanical properties in comparison to potential Mo based hard coatings, they offer a great possibility to learn which parameters influence those tribochemical reactions.

Both reactions are competing effects, whereat the formation of MoS_2 is favored. It is not yet clear whether this the result of the lower energy input unto the contact area due to MoS_2 lubrication or a sort of catalyst poisoning by MoS_2 covering the metallic Mo surface. Although small amounts of C-based phases are formed even in the presence

of the S containing EP additive, the C-based tribofilm formation is strongest, when no EP additive is present or the MoS_2 tribofilm is worn away at elevated rates with a Si_3N_4 ball at a temperature of 100 °C. Higher temperatures increase the formation of C-based tribofilm while the formation of MoS_2 already occurs at room temperature. For the most stable low friction conditions, an EP additive concentration of 3 % is sufficient. Molybdenum contacts with steel counter bodies greatly benefit from elevated temperatures up to 130 °C, while contacts with Si_3N_4 counter bodies suffer above room temperature due to micro-pitting and potential blocking of MoS_2 assembly by C-based species.

The S from the EP additive has a high affinity towards Molybdenum and although both Mo and Fe debris can be found in the tribofilm, only MoS_2 was detected by either Raman spectroscopy or TEM analysis. The MoS_2 tribofilm is formed at the Mo sample and debris surface and forms several protective 2D sheets of the characteristic S-Mo-S sandwich with a covering top-layer of amorphous C residue. The MoS_2 structures of the tribofilm are perfectly aligned with their easy shear plane in parallel orientation to the surface and provide the tribofilm with its low coefficient of friction.

6 Rebound Sputtering and the Mechanical Properties of Transition Metal doped Alumina Thin Films

The outstanding thermo-mechanical stability and chemical inertness of Al_2O_3 thin films attracts particular attention in academia and industry. While the thermodynamically stable α-Al_2O_3 (corundum) is limited to high deposition temperatures, the cubic γ-Al_2O_3 can be deposited by DC (pulsed) or RF reactive sputtering at more workable temperatures. Reactive DC sputtering yields moderately higher deposition rates, but struggles with non-stable deposition conditions due to the formation of isolating Al_2O_3 at the target surface.

Alumina thin films have spread to many fields of application, ranging from optical applications [232], corrosion protection [143], diffusion barriers [17, 18] to machining tools [142, 233]. They are in demand because of their electronic structure, high hardness (even at high temperatures), thermal as well as chemical stability, and their low interaction with working materials [142, 153, 234]. Initially, alumina thin films were predominantly produced via chemical vapor deposition (CVD), as the high process temperatures allowed the formation of the most stable structure, α-Al_2O_3. Since early achievements with reactive magnetron sputtering in the 90s [144-146], physical vapor deposition (PVD) has come a long way and is able to produce high quality crystalline γ-Al_2O_3 thin films. Although it is possible to deposit PVD α-Al_2O_3 by sputtering at

high deposition temperatures [145, 149, 235], PVD deposited γ-Al_2O_3 is a reasonably good alternative prepared at lower temperatures (thus suitable for a larger variation of substrate materials). At high deposition temperatures, especially during CVD, the low thermal expansion of α-Al_2O_3 often leads to severe crack formation during cooling after the process [142]. PVD coatings on the other side can be prepared at much lower temperatures [236], reducing the thermally induced strain and they often exhibit even compressive stresses due to ion bombardment. This gives PVD Al_2O_3 thin films an enhanced fatigue and thermal shock resistance [148], making them attractive for machining applications [142]. However, in order to form hard crystalline films by PVD, a threshold energy at the substrate surface has to be surpassed, allowing for sufficient surface diffusion [153]. This is reflected by the influence of the substrate temperature as well as the applied bias voltage on the thin film crystallinity [234]. So far, no commercially viable solution to form PVD α-Al_2O_3 at low deposition temperatures has been found and research focuses on the improvement of γ-Al_2O_3 thin films for industry.

Furthermore, the inherently unstable reactive deposition process of alumina is another extremely important research task. Reactive magnetron sputtering of Al in Ar/O_2 gas mixtures can be divided into three regimes [153, 237]. First, the metallic mode at low oxygen partial pressures, where typically no aluminum oxide island or continuous film is formed at the target surface. Under these conditions, often metallic to sub-stoichiometric oxide thin films are produced with high deposition rates. In the so-called poisoned mode, at higher oxygen partial pressures, non-conductive Al_2O_3 based islands and even a continuous film may form at the target surface. This immediately changes the electric conductivity of the target surface, secondary electron emission, as well as the sputter yield of the target. Aside from very low deposition rates (even lower than what would be expected according to the sputter yields [171]) the resulting thin films are typically amorphous and exhibit weak mechanical properties [153]. In between these

regimes lies a transition zone, which allows the deposition of γ-Al_2O_3 coatings with good mechanical properties but typically at low deposition rates. Unfortunately, the transition zone is characterized by generally unstable conditions due to arcing as a result of competing insulating Al_2O_3 formation as well as re-sputtering [238] and the hysteresis effect [173]. Many strategies to overcome the unwanted process instability due to the hysteresis effect rely on complex feedback controls to adjust the availability of oxygen [174, 176, 239, 240]. Furthermore, high gas flows coupled with increased pumping speeds or specific target designs can influence the sputter erosion areas [174, 175]. Most of those strategies ignore some even enhance the main problem of reactively sputtered oxide coatings: very low deposition rates caused through poisoning effects [176].

A very promising approach to stabilize the transition region for Al targets was outlined by *Berg* et al. and relies on the doping of the target surface with heavy elements (e.g. Pt) utilizing a serial secondary sputter source [241]. This doping effect enhances the collision cascade of impinging Ar ions at the target surface and reflects the cascading light Al atoms back towards the surface [242] in a kind of rebound effect. Monte Carlo based modeling studies (TRIDYN) by *Kubart* et al. have shown that these effects can also be achieved with further elements such as W [243]. Simulations of serial co-sputtering processes (with W being sputtered onto a rotating Al target before the doped Al is reactively sputtered onto the substrate) promise a theoretical increase of the deposition rate of up to 80 % [244], which also has been confirmed experimentally [245]. Similar theoretical studies also suggest that the amplification of the sputter yield occurs if Al targets are doped with heavy elements [246].

In order to reduce the complexity of the equipment, and consequently make this sputter yield amplification more application-friendly, we investigated the influence of Cr, Mo, W, and Nb dopants of powder metallurgical produced Al targets on the process stability

and phase formation. For the use of Al_2O_3 coatings beyond the scope of optical applications this work highlights not just the deposition rate enhancement of the W micro-alloyed Al-targets but also investigates the structure, chemical composition, and enhanced mechanical properties of the obtained thin films.

6.1 Experimental

The sputtering process was realized in an ultra-high vacuum (UHV) laboratory scale unbalanced magnetron sputtering chamber (Orion 5, AJA) equipped with 3-inch targets (Plansee Composite Materials). The sputtering atmosphere was a defined Ar/O_2 mixture (with a constant flow rate of 20 sccm across all gas compositions) and the cathode DC power density was set to 9 W cm^{-2}. To enable sufficient surface diffusion for the formation of crystalline γ-Al_2O_3 thin films, the substrates were heated to 500 °C (the actual substrate temperature $T_{sub} = 300 \pm 10$ °C) and a pulsed (150 kHz, 1296 ns) bias potential of -50 V was applied. For both, sputtering and bias, RPDG 50 generators with arc control (MKS Instruments) were used. The micro-alloyed targets were produced by hot isostatic pressing of a fine-grained Al powder (particle size <63 µm), mixed with either 2 or 5 at.-% metallic dopant-powder of our selected heavy alloying elements Cr, Mo, W, or Nb. The alloying elements were selected based on their mass as well as phase stabilizing effects. Especially, Cr_2O_3 (differing from Mo and W) adapts the corundum type structure and therefore easily forms mixed crystals with alumina. The neighboring Nb on the other hand possesses a different electron structure and is in mass and density similar to Mo although the atomic radius of Nb lies slightly above that of W. All doped targets reached above 99.5 % of their theoretical density and dopant particles were evenly distributed across the target volume with the following particle sizes: Cr <80 µm, Mo <30 µm, W <10 µm, and Nb <125 µm. In order to determine the process parameters at a working gas pressure of 0.4 Pa in dependence

on the doping elements and gas composition, the poisoning behavior of the targets was recorded. The gas mixture was investigated up to 55 vol.-% O_2 in the sputtering atmosphere and for each target the ideal normalized O_2 flow, $f_{O2}^{norm}=f_{O2}/(f_{Ar}+f_{O2})$ to stay within the beginning transition regime was used, which is 31 % for all targets except the 5 at.-% W alloyed target, operated at 42 %.

Investigations of the plasma compositions were carried out by plasma analysis using a Langmuir probe (ESPion, Hiden) mounted in an adapted Z400 sputtering system (Leybold Heraeus). The plasma parameters were recorded at fixed positions above the racetrack using three different gas mixtures based on the poisoning behavior [247].

Prior to deposition all substrates were cleaned in an ultrasonic acetone and ethanol bath and subsequently Ar-ion etched for 10 min directly before the depositions (seamless transformation). All coatings were evaluated and surveyed with secondary electron microscopy (SEM, FEI Quanta 250 FEG) and of those, deposited from the 2 at.-% doped targets, also cross-sections were prepared for transition electron microscopy (TEM). The final thinning of the TEM samples was achieved by ion polishing, using a precision ion polishing system (PIPS, GATAN Inc.). TEM investigations were performed with a FEI TECNAI F20 operated at an acceleration voltage of 200 kV, equipped with an Apollo XLTW SDD EDAX detector for chemical analyses. In addition, the phase formation was characterized by selected area electron diffraction (SAED). Since energy dispersive x-ray spectroscopy (EDX) is prone to errors in measuring light elements and low elemental concentrations, the chemical composition was also determined with elastic recoil detection analysis (ERDA) using a 43 MeV Cl^{7+} ion beam. The chemical compositions were calculated out of the fitted spectra using the NDF software [248].

A better understanding of the coating structure was achieved with x-ray diffraction (XRD) utilizing a multipurpose diffractometer (Empyrean, Panalytical) in

its grazing incident diffraction (GID) setup (incident beam at 2°) with a Cu-K radiation source (equipped with a parallel beam mirror) and a scintillation detector (behind a 0.18° parallel plate collimator). To investigate any preferred orientations, the coatings were also analyzed in a Bragg-Brentano geometry with a Bragg-Brentano HD mirror and a PIXcel3D detector (Panalytical).

The mechanical properties, hardness (H) and indentation modulus (E), of the $(Al_{1-z}M_z)_2O_3$ thin films on Si substrates were obtained by nanoindentation, using an ultra-micro-indentation system (UMIS) equipped with a Berkovich tip. Each measurement contained 40 indents, whose indentation depth was kept below 10 % of the coating thickness to avoid influences from the substrate. The loading and unloading segments of the indentation curves were fitted according to Oliver and Pharr's method to obtain the hardness and indentation modulus of the coatings [249]. The residual stress was calculated via the Stoney equation from the curvature of the coated substrates (PS50, Nanovea).

6.2 Results and Discussion

The micro-alloying with Cr, Mo, and W leads to an increase in process stability, especially with respect to higher oxygen partial pressures. In general, a complete suppression of arcing events was not observed, but the doping drastically reduces the amount of severe arcing events. In contrast, Nb showed no beneficial effect concerning arc suppression. Minor arcing events, that otherwise can be overcome by the generator-built-in arc suppression are only reduced by micro-alloying with Cr. All dopants demonstrate an influence on the poisoning hysteresis of Al targets as displayed in **Figure 29**. Targets alloyed with Cr or Mo (**Figure 29a** and **b**, respectively) demonstrate a slight expansion of the transition region in comparison to pure Al

targets, retarding the coverage of the target surface with non-conductive oxides. In a similar manner, Nb (**Figure 29d**) pushes the poisoning of the target to higher levels as well, but also demonstrates a stronger dependence on the dopant concentration. The even more enhanced behavior of W-doped targets offers a first insight into the proposed rebound effect, leading to an amplification of the sputter rate. The heavy alloying element acts as a local barrier under the Al surface, which densifies the collision cascade directly at the target surface by deflecting cascading atoms back [241, 245]. This in a further consequence enhances the sputter rate above the evenly distributed W grains in the micro-alloyed target. The target poisoning is delayed to high oxygen concentrations as an increased atom flux from the target retards the oxygen from poisoning the racetrack. This opens a relatively wide process window for the deposition of $(Al_{1-z}W_z)_2O_3$ coatings and allows the formation of stoichiometric alumina based coatings at high deposition rates. In contrast to Cr, Mo, and Nb doping, an increasing W content also allows that an already poisoned target surface is cleaned from formed compound and returns earlier to the transition region upon decreasing the oxygen flow rate (**Figure 29c**, blue lines). This highlights the potential of W dopants in promoting the removal of formed Al_2O_3 compound layers and for increased stability compared to non-alloyed Al targets.

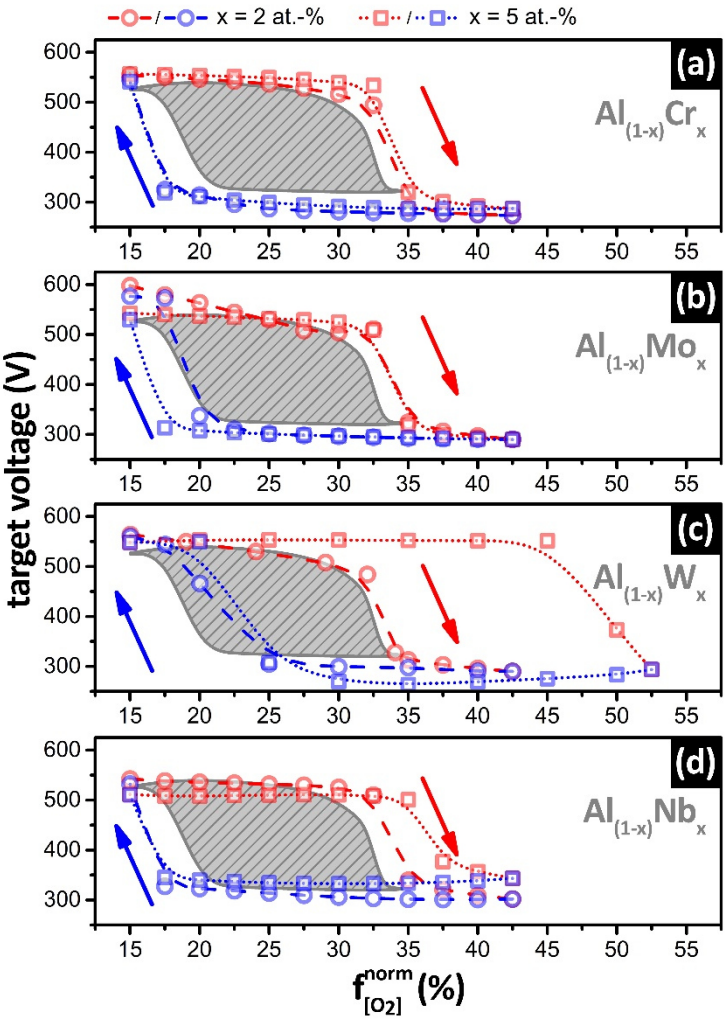

Figure 29: Poisoning behavior of the (a) Cr-, (b) Mo-, (c) W-, and (d) Nb- micro-alloyed targets with increasing oxygen contents. The gray shaded areas represent the hysteresis of a non-alloyed Al target.

In order to get a deeper insight in the plasma conditions, Langmuir probe measurements were carried out for the 2 at.-% alloyed targets for various oxygen partial pressures (3 specific points in relation to the poisoning state). In general, the addition of dopants decreases the floating potential (**Figure 30a**) and increases the ion (**Figure 30b**) and electron density (**Figure 30c**). In particular, W leads to a significant increase in ion density up to high oxygen flow rates, which suggests an increased particle, ion, and electron interaction (within the plasma). This effect is highly retarded as the

targets reach their poisoned state. For all dopants, the electron density does not drop as pronounced as compared to the ion density, demonstrating that the secondary electron emission increases in the poisoned mode. For Cr and W doped targets the decrease of ion- and electron densities correlates, whereas for Nb, Mo, and Al the electron density rises drastically as the target forms a non-conductive oxide layer. In this state, a big fraction of the energy imposed on the target is most likely lost to secondary electron generation. This is also an indication for the proposed rebound sputter effect, as W and Cr help to keep the target area free from isolating oxides.

The increased plasma density and the retardation of the target poisoning clearly indicate the positive effects of the transition metal dopants on the sputtering of Al in a reactive (oxygen containing) atmospheres. In a further consequence, the obtained changes within the target surface as well as plasma conditions are clearly reflected in the deposition rates. In **Figure 31a**, a clear enhancement of the deposition rate for Cr and W doped targets can be recognized. For Cr we observed an increase with increasing alloying content, although the overall deposition rate is lower than for non-alloyed Al targets. This might be the result of an increased crystallinity of the thin film, which forms a solid solution Al_2O_3-Cr_2O_3. In case of the 5 at.-% W doped target, the deposition rate increases by up to 80 %, being in good agreement to theoretical studies [244, 246] as well as approaches by co-sputtering [245]. The mechanism of the deposition rate-enhancing, so-called rebound sputtering effect, may be derived from a top-view SEM image of a freshly sputtered target surface, presented in **Figure 31b**. Tungsten is evenly distributed within the target (**Figure 31c**) and due to the small W particle size high density of individual rebound sputtering centers is realized. As a consequence of the enhanced collision cascade, mentioned before, Al above W grains sputters at higher rates, leading to an amplified deposition rate and an accelerated erosion in W near regions. Furthermore, sputtered tungsten atoms possibly act as a sort of “battering

ram" eroding the Al material in its vicinity (even under the W particle) at higher rates. This can be observed as W particles are lying in the center of self-induced Al craters and in some cases, the outline of the surrounding crater follows the shape of the W particle. The increased target erosion around the W particles in the Al target defines the rebound sputtering process and differentiates the effect from sputter yield amplification with implanted single dopant atoms. In comparison to W, the lighter Mo shows no amplification of the sputter yield. For Nb, which has a larger atomic radius but only the mass of Mo, no increased sputter rate could be measured, highlighting the importance of the dopant mass and density over its size to achieve the rebound sputtering effect.

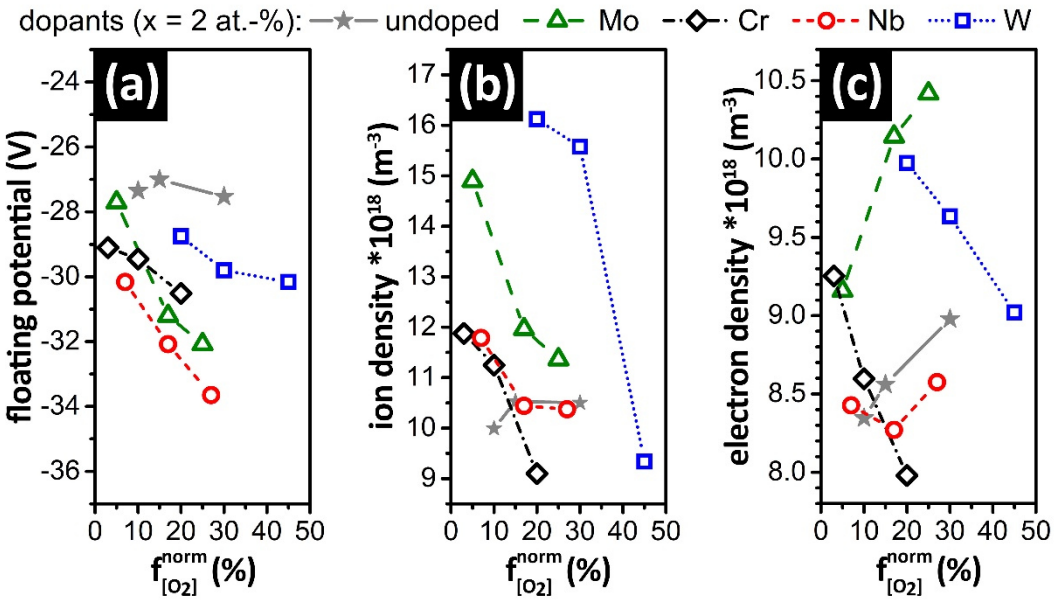

Figure 30: Plasma parameters based on Langmuir measurements: (a) floating potential, (b) ion density, and (c) electron density for gas mixtures in the metallic, transition, and poisoned mode, respectively.

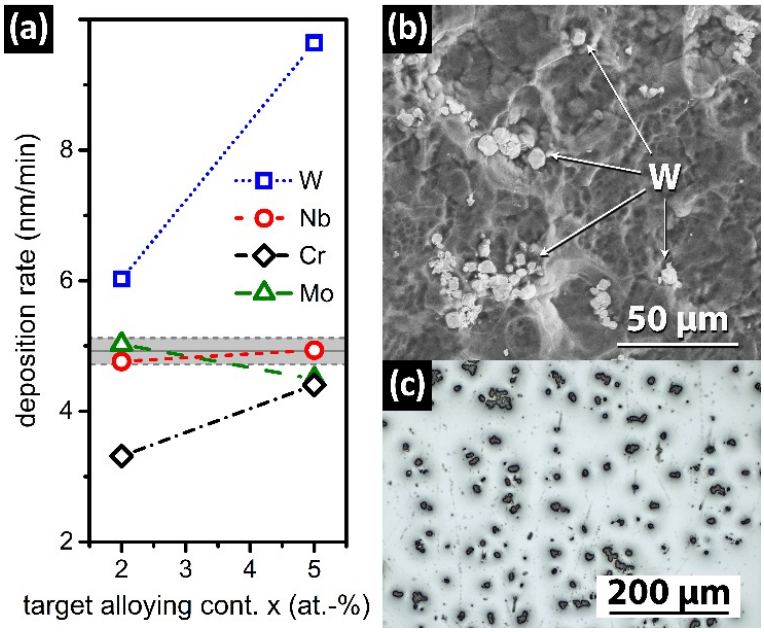

Figure 31: (a) Deposition rate depending on the transition metal content of the micro-alloyed targets. (b) SEM top-view of the 5 at.-% W alloyed Al target after a sputtering process in the transition region (especially the Al regions around W particles are sputtered at higher rates, forming characteristic craters around these particles). (c) Light optical microscopy cross-section of a virgin 5 at.-% W alloyed Al target.

The actual amount of dopant that is incorporated into the coating was measured by ERDA and is displayed in **Figure 32a**. Surprisingly, only trace amounts of Mo are being incorporated into the coating and the coating content, y, does not correlate to the Mo target concentration, x. As Mo easily forms volatile oxides it is most likely removed from the high energetic (temperature, bias, impinging sputtered species) growth zone before it can be incorporated into the coating structure. Cr concentrations are most likely reduced due to the formation of volatile oxides as well, but at a much lower rate compared to Mo. The incorporation of dopants lies at 50 % of the dopant target content for Nb and even further below for Cr. The W alloyed Al targets deviate from this trend by showing a good correlation between target content, x, and coating concentration, y. Thin films, from the 5 at.-% W micro-alloyed Al target even show a

enrichment of W above the alloying content, possibly due to the resputtering of lighter Al and O atoms. At this point, we want to note, that due to the addition of 40 at.-% oxygen during reactive sputtering, 5 at.-% dopant in the target corresponds with 2 at.-% dopant in the coating. However, all dopants are evenly distributed throughout the depth of the crystalline regions of the coating.

The influence of the dopants on the Al to O ratio is displayed in **Figure 32b**. The undoped Al_2O_3 coatings have a slight O-deficiency (around 1 at.-%). Due to the easy formation of Al_2O_3-Cr_2O_3 [250-252] mixed crystals, Cr^{3+} replaces Al^{3+} on the metal sub-lattice, the oxygen content is not significantly influenced by the addition of Cr. The minor incorporation of Mo into the coating does not influence the metal to oxygen ratio as well. It is worth mentioning that this also demonstrates the sufficiency of the oxygen, available in the coatings growth region. If the O-deficiency would be a result of O-depletion in the growth zone, the exclusion of additional oxygen from the growing surface (via the formation and evaporation of volatile Mo-oxides) would result in a more pronounced O-deficiency with increasing Mo content. Hence, the formation of vacancies is driven by the growth mechanism and not the O-availability. Interestingly a W dopant concentration of roughly 0.8 at.-% in the coating leads to an O content above the stoichiometric Al_2O_3 level, which can be explained by tungsten's favored oxidation state +VI (compared to Al: +III), possibly introducing vacancies on the metal sub-lattice to retain charge neutrality. Higher W concentrations within the coating (around 2.5 at.-%) result in a correlating reduction (2.5 at.-%) of the Al content. At the same time, for higher W concentrations again a stoichiometric Al_2O_3 composition is obtained.

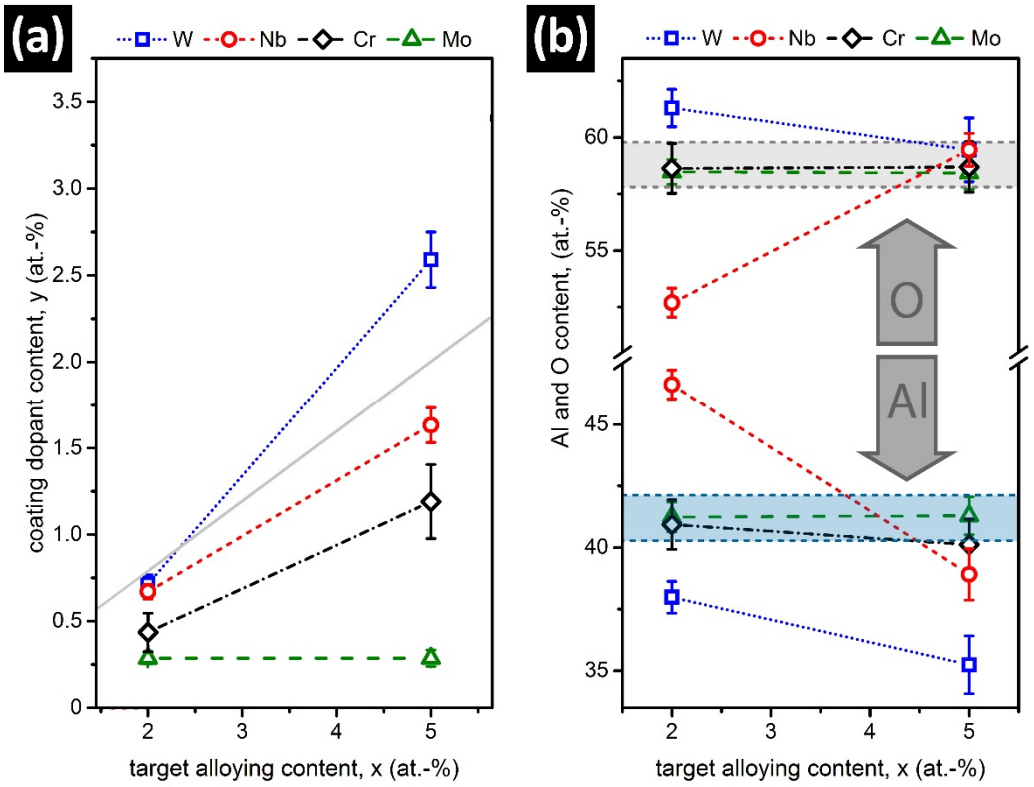

Figure 32: (a) ERDA obtained TM content within the prepared coating with respect to those of the targets. An ideal relation for the formation is given by the grey solid line. (b) Al:O ratio within the coating. The colored horizontal lines indicate the composition of the undoped alumina coating.

All crystalline coatings demonstrated a weak (100) orientation in Bragg-Brentano XRD measurements. The coating structures obtained by GID, **Figure 33**, strongly depend on the dopant and its concentration. Cr has almost no impact on the structural formation, as it nicely incorporates into the Al_2O_3 lattice. As shown in **Figure 32a**, Mo doping does not translate to the coating composition and is only incorporated into the coating in trace amounts. Therefore, no pronounced effect on the crystal structure can be observed compared to undoped Al_2O_3 thin films. W on the other hand, is incorporated into the film, leading to decreasing XRD peak intensity with increasing W content, **Figure 33**. This might be a result of its electronic structure and preferred oxidation states, but the simple fact that W has roughly seven times the weight and

six times the size of Al illustrates why concentrations below 1 at.-% already have a huge impact on nucleation and growth mechanisms. Niobium with a size comparably to W, exhibits a similar effect on the XRD patterns.

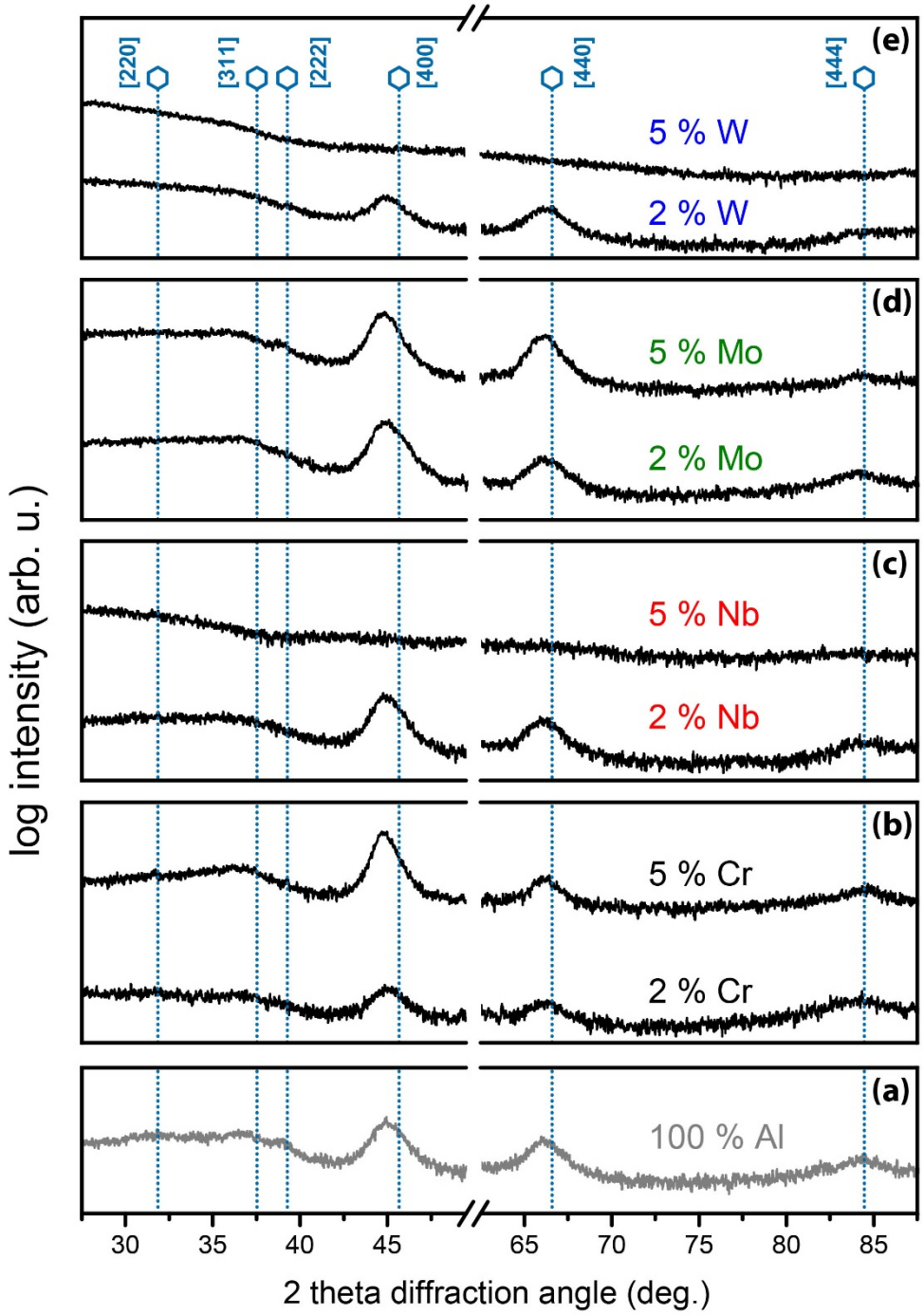

Figure 33: GID (XRD) measurements of our coatings in dependence of the chemical target composition, indicated on the right side of the graph. The peak positions of γ-Al_2O_3 are marked.

All coatings, except for the Cr doped Al_2O_3 (**Figure 34b**) exhibit a more or less pronounced amorphous coating fraction at the Si substrate interface, indicating a rather high barrier for nucleation. Mo doped (**Figure 34c**) and undoped Al_2O_3 (**Figure 34a**) clearly exhibit the development of a fine columnar structure after several nanometers of the initial amorphous region. After a few more nanometers, these coatings exhibit a nanocrystalline and dense microstructure. Contrary, the Nb and W alloyed coatings, exhibit rather wide amorphous regions that protrude far into the coating. We suspect these initial growth mechanism to be the result of substrate Si diffusing into the coating at elevated temperature as well as high energetic particle bombardment (through heavy W or Nb atoms), leading to an initially amorphous growth mode [253, 254]. Cr doped Al_2O_3 coatings do not exhibit any nucleation difficulties. It is possible, that impinging Cr species could potentially bind the Si in intermetallic phases [255] at interfaces or grain boundaries (Al cannot [256]). The effective range of Si will also be increased by the mixing effects due to bombardment of the initial Si-surface and first few nanometers of coating with heavy element dopants. The impact possibly leads to increased atomic mixing of the interface, enhancing the Si penetration into the coating which most likely is already high due to the dopant-triggered defective structure providing ample pathways for diffusion.

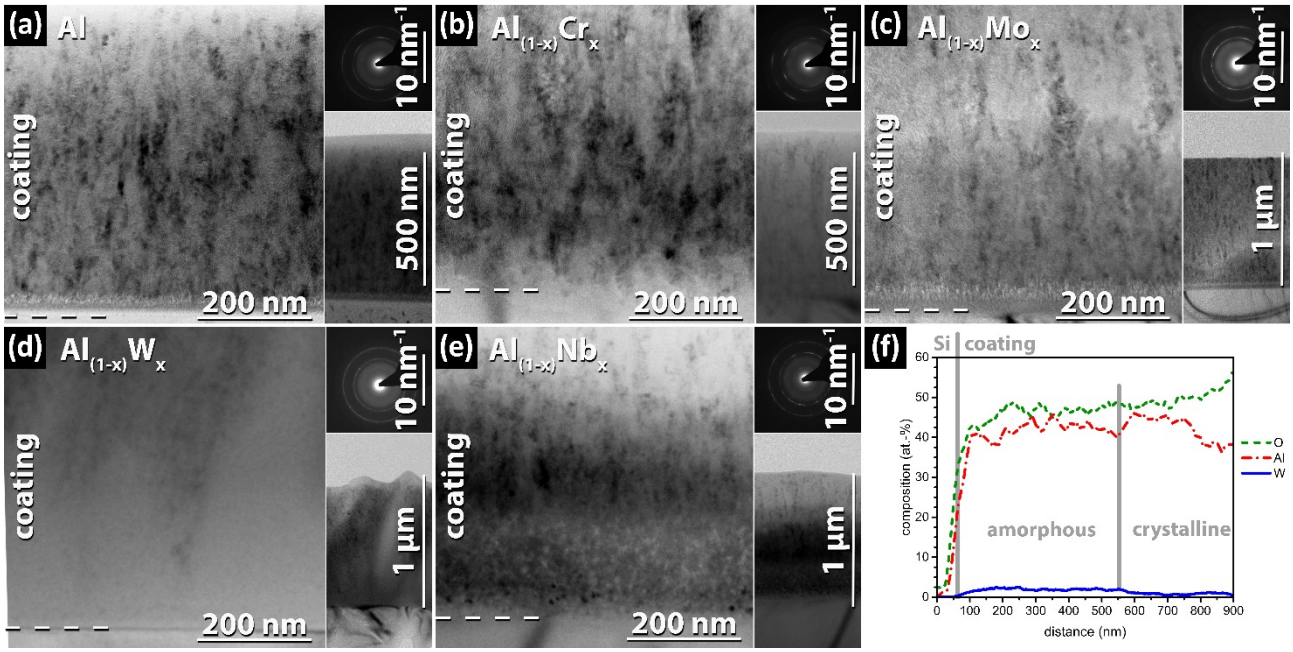

Figure 34: Cross sectional TEM BF images of the interface near region and coating structure. Every panel for each dopant (2 at.-%): (a) pure Al_2O_3, (b) Cr, (d) Mo, (e) W, and (c) Nb also includes an SAED pattern of the crystalline regions in the right upper corner and an overview across the whole sample at the bottom. (f) A line-scan through the 2 at.-% W doped coating (perpendicular to the substrate).

TEM investigations (**Figure 34d**) of the 2 at.-%W doped coatings on the other hand clearly show that W leads to an increased initial amorphous growth regime directly at the interface to the Si substrate. This is also reflected by the structural XRD analysis confirming an increased amorphous phase fraction, which is even more pronounced for the 5 at.-% W containing coatings.

Nb alloyed coatings show a similar effect, although the impact seem to be not that pronounced as for the W alloyed coatings. The TEM micrographs (**Figure 34e**) show an extended amorphous region close to the Si-substrate interface, which is followed by a crystalline region, as confirmed by SAED showing γ-Al_2O_3.

An EDX line-scan (in growth direction), **Figure 34f**, indicates that especially the amorphous interface-near region contains a higher W-content.

Despite the amorphous regions, low W-containing coatings still have a high hardness of 28 GPa (compared to 27 GPa for undoped Al_2O_3 coatings). Mo- and Nb-containing coatings have a slightly lower hardness (**Figure 35a**), when prepared from the 2 at.-% micro-alloyed targets. Contrary, the Cr-containing coatings exhibit the highest hardness of up to 30 GPa, even for the higher Cr concentrations, prepared from targets with 5 at.-% Cr. The coatings containing Mo, W, or Nb exhibit a significantly lower hardness (below 14 GPa) if they are prepared from targets containing 5 at.-% transition metals (**Figure 35a**). If we consider the hardness with respect to the actual transition metal content within the coating (**Figure 35b**), coatings prepared from the Mo containing targets need to be mentioned separately (the others exhibit an expected hardness vs. transition metal content slope). The Mo content is for the coatings prepared from 2 or 5 at.-% micro-alloyed targets very similar with roughly 0.25 at.-% (**Figure 32a**). However, their hardness is completely different with either 26 or 8 GPa. This suggests that most of the Mo (from the target) arriving at the substrate or growing film will form volatile Mo-oxides. This process significantly will influence the nucleation and growth process of the coating itself, leading to an under-dense columnar growth morphology, resulting in explicitly reduced mechanical properties.

The indentation moduli of the coatings exhibit only for the W and Mo doped materials a huge dependence on the transition metal content of the target (**Figure 35c**). Interestingly, the W doped coatings exhibit an even higher indentation moduli (than the undoped Al_2O_3 coatings) if they are prepared from the 2 at.-% W micro-alloyed targets. Again, similar to the hardness, also the indentation moduli drops for the Mo-containing targets (despite the similar Mo content in the coating), see **Figure 35d**.

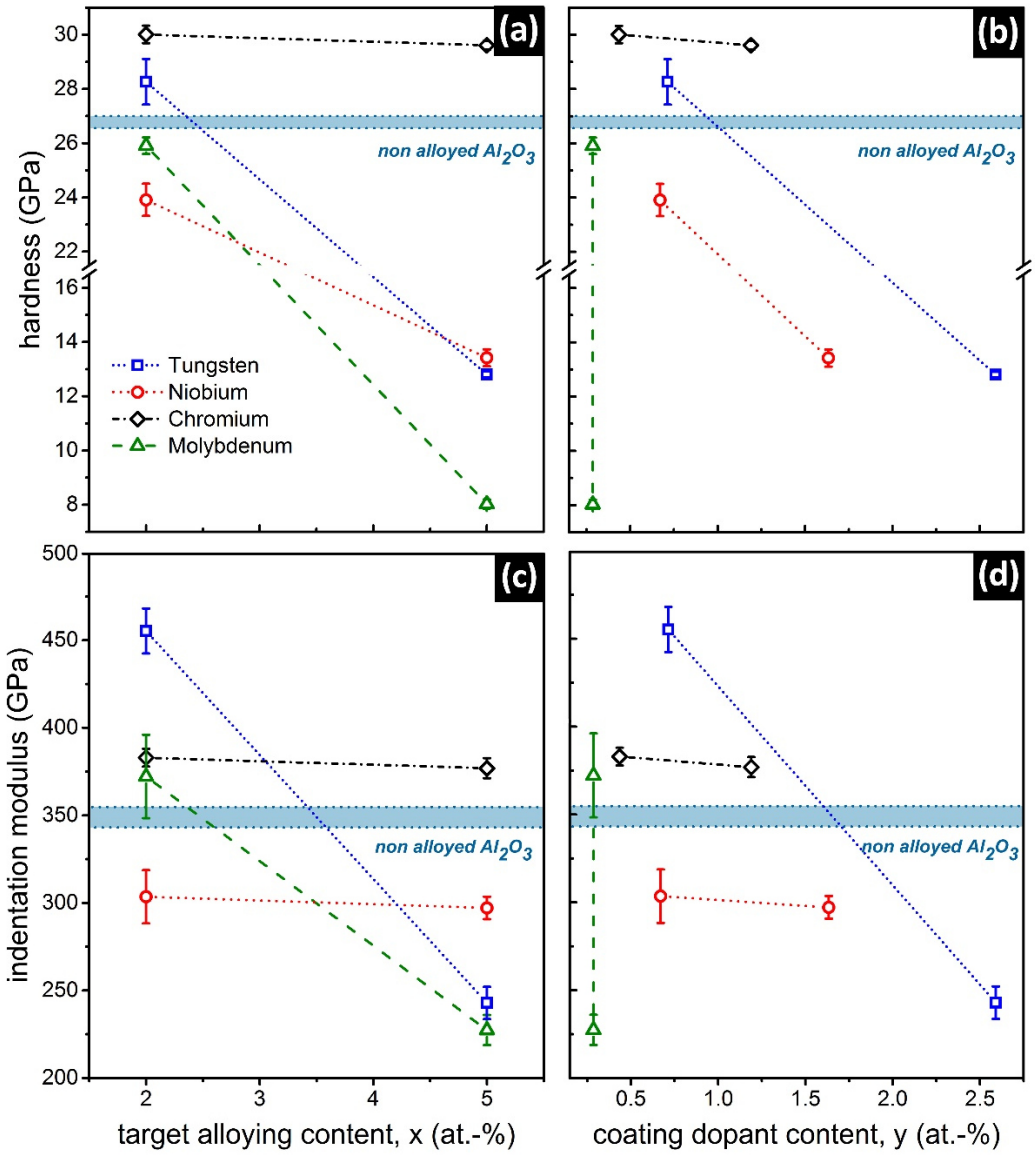

Figure 35: Hardness (a) and indentation modulus (c) of our coatings with respect to the target composition and in dependence on the chemical composition within the coating (b) and (d).

The residual stress of our Al_2O_3 coatings, being compressive with -1.6 GPa, are not influenced (within the error of measurements) when using 2 at.-% Mo, Cr, or Nb containing targets. The coatings prepared from 2 at.-% W micro-alloyed targets exhibit only -0.8 GPa stresses. When using 5 at.-% micro-alloyed targets, the compressive residual stresses increase to -3.2 GPa for Cr alloyed targets, but decrease to -0.2 GPa

for W or Nb alloyed targets, and stay at almost -1.6 GPa for Mo alloyed targets. In general, this highlights the positive effect of rather small amounts of W on the mechanical properties of Al_2O_3, as the small hardness increase (from 27 to 28 GPa) is not due to an increase in compressive stresses.

6.3 Summary (Chapter VI)

The reactive DC sputtering process of alumina coatings from Al targets in O_2 containing atmospheres can be improved by micro-alloying the target with Cr, Mo, or W, but not with Nb. These alloying elements significantly reduce severe arcing events. Most effective to reduce minor arcing events (that can be counteracted by the generators built-in arc suppression) is the alloying with Cr. Cr is also able to directly promote the formation of crystalline regions already close to the Si substrate interface, whereas Nb nut especially W lead to an extended amorphous-like growth region. Mo has a special impact on the growth morphology, as most of the arriving Mo species (at the substrate and growing film) form volatile Mo-oxides. Even with the coatings prepared from 5 at.-% Mo alloyed targets, only 0.25 at.-% Mo can be detected in the coating. The formation of these volatile Mo-oxides interrupt the growth process of these coatings, leading to the formation of a mechanically very weak (8 GPa hardness) and under-dense columnar structure.

Especially coatings prepared from 2 at.-% W alloyed targets exhibit a high hardness (28 GPa), high indentation modulus (450 GPa), low compressive stresses (-0.8 GPa), and a relatively high deposition rate (6 nm/min). The corresponding values for coatings prepared from unalloyed Al targets are a hardness of 27 GPa, an indentation modulus of 345 GPa, -1.6 GPa stress, and a deposition rate of 5 nm/min. With a higher W content (5 at.-% W in the target) the growth rate increases (slightly below 10 nm/min), but hardness and indentation modulus decrease to 14 and 250 GPa, respectively.

7 Influencing the γ- to α-Al_2O_3 Phase Transformation in Thin Films

Alumina coatings, initially produced as α-Al_2O_3 by chemical vapor deposition, have long found their way into physical vapor deposition, where metastable γ-Al_2O_3 can be deposited at much lower temperatures. These γ-Al_2O_3 coatings are increasing in popularity, despite restrictions by the thermally triggered transformation to α-Al_2O_3, leading to cracking and coating failure. Transition metal dopants, as the focus of this study, have a huge impact on the transformation onset temperatures

After decades of research, many questions about alumina are still unexplored. Many studies investigate the formation of its metastable low temperature phases (χ, κ, η, γ, δ, and θ), so-called transition aluminas, or their transformation pathway to the highly stable α-Al_2O_3. In some cases, definite answers are hard to get, as the phase transitions strongly depend on the reaction conditions and educts. This is especially true for coating technology, where Al_2O_3 thin films are of high interest for optical, electrical [257], thermal or diffusion barrier [258] and machining applications [142, 233, 259]. The formation of α-Al_2O_3 (corundum type structure) can easily be realized with chemical vapor deposition (due to high deposition temperatures). However, very often the parts to be coated require much lower deposition temperatures, which can be realized in PVD [144, 146, 260, 261], leading to the formation of the metastable crystalline structures γ-Al_2O_3 [146] and θ-Al_2O_3. Solid solutions of Al_2O_3-Cr_2O_3 in thin

films have also be reported to adapt a fcc B1-like structure, which is often favored in PVD [262-264], which is not done in this study. The fraction of the individual metastable crystalline phases can be modified by the substrate temperature and ion bombardment [144, 265]. Due to the high cooling rates (by condensation from the vapor phase), the cubic structured γ-Al_2O_3 is typically preferred in PVD based film growth [266]. Although γ-Al_2O_3 coatings show promising results as catalyst carriers, in bio-applications, and cutting operations [267], their thermal stability is limited due to the phase transformation to α-Al_2O_3, leading to coating failure [268, 269] due to the associated volume change [270, 271]. In principal there are two strategies avoiding this problem: *(i)* a direct stabilization of α-Al_2O_3 during PVD based synthesis [150, 250, 272-275], *(ii)* or retarding the γ to α transformation (typically between 1000 °C and 1100 °C [233, 259], requiring an activation energy of about 540 kJ/mol [276]) to higher temperatures. PVD deposited Al_2O_3 generally exhibits a nanocrystalline morphology, which promotes the γ-phase due to its lower surface energy (compared to α-Al_2O_3) [277]. As by annealing also the built-in defect density decreases (due to recovery effects and even recrystallization effects), the thereby connected grain growth reverses the preference of the γ- over the α-phase. Typically between 1000 and 1100 °C the Al_2O_3 phase transforms to α-Al_2O_3, with a subsequent huge increase in grain size [233]. While Cr is widely used to stabilize the α-phase [278, 279], other elements like Si, Er, La, Sr, or Y [253, 280-284] have been reported to stabilize γ-Al_2O_3 or at least to delay the transformation. Recently, transition metals have been reported to beneficially influence the reactive sputter deposition process of Al_2O_3 thin films [241, 243, 245] (chapter 6). Here, we investigate the influence of Cr, Mo, Nb, and W on the thermal stability of PVD prepared γ-Al_2O_3 and the γ- to α-Al_2O_3 phase transformation, knowing that especially Cr should promote the phase transformation.

7.1 Results and Discussion

All necessary coating depositions were realized in an unbalanced magnetron sputtering process (Orion 5, AJA International) with 3 inch $Al_{1-x}M_x$ targets (Plansee Composite Materials). The targets were powder-metallurgically produced with a fine-grained structure and an evenly distributed fraction of Cr, Mo, Nb, or W, with x = 0, 2, and 5 at.-%. These were sputtered with a power density of 9.0 W ▪ cm^{-1} in an Ar/O_2 mixture at a deposition pressure of 0.4 Pa (between 31 and 38 % O_2 flowrate), depending on the target composition (details are given in chapter 6). To prepare substrate-free coating material, low alloyed steel foil was used as a substrate. It was necessary to protect this steel foil from oxidation, as thereby Fe-oxides would form during the initial stage of deposition, which are difficult to remove from the coating material. Therefore, a few nm thin Al layer (using an additional built-in 2 inch cathode) was deposited before oxygen was introduced to the chamber. The low alloy steel foil was subsequently (after the deposition process) chemically removed with diluted nitric acid. The residual coating powders were thoroughly washed and quality checked with XRD. Detailed chemical investigations (by ERDA, see chapter 6) show that the W content within the coatings (with 0.8 respectively 2.0 at.-%) corresponds to the target composition of 2.0 respectively 5.0 at.-% W, when considering the formation of sesquioxides (M_2O_3). When using Nb or Cr alloyed targets, their content in the corresponding coatings is with 0.7 at.-% Nb or 0.4 at.-% Cr (from targets with 2 at.-% Nb or Cr) and 1.5 at.-% Nb or 1.2 at.-% Cr (from targets with 5 at.-% Nb or Cr) significantly below the theoretical value of 0.8 and 2.0, respectively. Due to the formation of volatile molybdenum oxides during the deposition process, only ~0.25 at.-% Mo can be detected in the coatings prepared with Mo alloyed targets, regardless if the target contained 2 or 5 at.-% (**Figure 32a**).

The thermal stability of the coatings was investigated with dynamical differential scanning calorimetry (Netzsch STA 449 F1) using a heating rate of 10 K/min in synthetic air up to 1600 °C. The powdered substrate-free coating samples were investigated with XRD (XPert II, PANalytical), in a Bragg-Brentano setup, before and after the DSC measurement. Detailed XRD (**Figure 38a**) and cross-sectional TEM (**Figure 36**) investigations indicate that all as deposited coatings are composed of amorphous and crystalline γ-Al_2O_3 fractions. The crystalline phase fraction increases with increasing Cr content and decreases with increasing Nb and W content (chapter 6). Especially at the interface to the substrate, the amorphous phase fraction dominates, indicating the rather high nucleation barrier for the formation of crystalline Al_2O_3. Considering the classical nucleation theory, this basically traces back to a significant surface energy contribution. Consequently, during PVD at low substrate temperatures, the phases with the lowest surface energy and highest symmetry will prevail.

Although the coatings prepared from 2 or 5 at.-% Mo alloyed targets contain almost the same low Mo content of ~0.25 at.-%, their XRD patterns (**Figure 38a**) suggest a higher fraction of γ-Al_2O_3 when using the 5 at.-% Mo containing target. The increased volatile Mo-oxide formation (during preparation of Al_2O_3 based coatings from the higher Mo containing Al-target) leads to a higher defect density within the growing films (chapter 6), which increases the fraction of possible nucleation sites and therefore these films contain a higher crystalline phase fraction. This again indicates the difficulties of nucleating crystalline phases within the Al_2O_3 system, when using relatively low temperatures as used by PVD.

In our previous study we could show that especially the use of W alloyed Al targets leads to a stable DC sputter process even in high level O_2 containing atmospheres, high deposition rates, but an increased amorphous phase fraction. Furthermore, coatings

prepared from 2 at.-% W alloyed Al targets still exhibit a rather high hardness of 28 GPa, high indentation modulus of 450 GPa and low compressive stresses of -0.8 GPa. The 5 at.-% W containing Al targets lead to an even higher deposition rate and coatings with an even higher amorphous phase fraction, but significantly lower hardness of 14 GPa and indentation modulus of 250 GPa. Therefore, we present high-resolution TEM (FEI TECNAI G20) studies of as deposited coatings prepared from 2 at.-% W alloyed targets in more detail. In the as deposited state, the coating is characterized by a mixed structure composed of amorphous and nanocrystalline regions (**Figure 36a**). Especially at the interface to the substrate the amorphous phase fraction is significantly higher. Selected area electron diffraction (**b**) and Fast Fourier Transformation (**c**) of the HR TEM image (**d**) confirm that the crystalline regions are based on cubic γ-Al_2O_3.

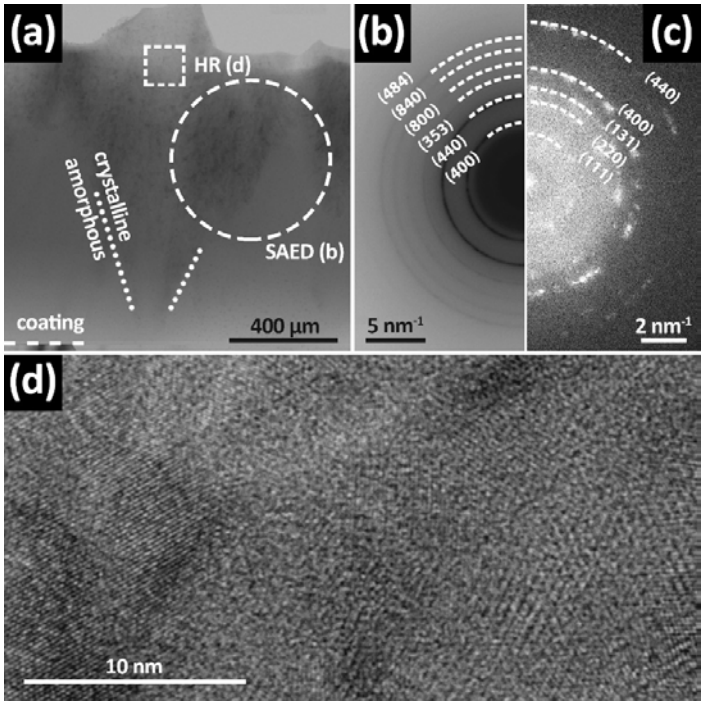

Figure 36: TEM investigation of the coating. (a) The coating is initially amorphous and exhibits cone-shaped crystalline γ-Al_2O_3 regions. (b) SAED pattern of the coating showing the reflexes of γ-Al_2O_3 and an amorphous fraction. Fourier Transformation (c) of HD TEM images (d) also confirm the nanocrystalline γ-Al_2O_3 structure of the coating.

The DSC heat flow, **Figure 37a**, shows a clear exothermal peak for the γ- to α-Al_2O_3 phase transformation. For the 2 at.-% W doped coating, the interpretation of the DSC curves and the identification of the α-Al_2O_3 formation is non-trivial as it appears to be superimposed by a exothermic reaction. The weak exothermal signal (W doped coating) at 900 °C can be contributed to the crystallization of the amorphous regions by XRD. As the exothermal heat flow signal from the γ- to α-Al_2O_3 transformation is very pronounced for all other coatings, the transformation of W doped Al_2O_3 coatings most likely occurs in the region above 1290 °C. This is also indicated by the mass loss, that occurs during the phase transformation of all coatings, see **Figure 37b**. In addition it can be noticed that for all coatings, except for those produced from the W alloyed target, the mass stabilizes after the phase transformation, indicating a formation of volatile oxides. The sublimation of common tungsten oxides can occur at temperatures above 1000 °C [285] and could explain the deviation of the heatflow (endothermal sublimation) and the additional mass loss above that temperature.

The onset temperatures of the γ- to α-Al_2O_3 transformation for all coating compositions (**Figure 37**) suggest an onset retardation for 2 at.-% W doped coatings. Like W doped coatings, the equally amorphous Nb doped coatings experience additional exothermal reaction at around 900 to 1000 °C, suspected to be an amorphous to γ-Al_2O_3 crystallization or the formation of an intermediate θ-phase, which has been reported also for amorphous Al_2O_3 coatings [286]. These peaks become more pronounced for coatings produced from 5 at.-% W or Nb alloyed targets, agreeing with the increased amorphous fraction.

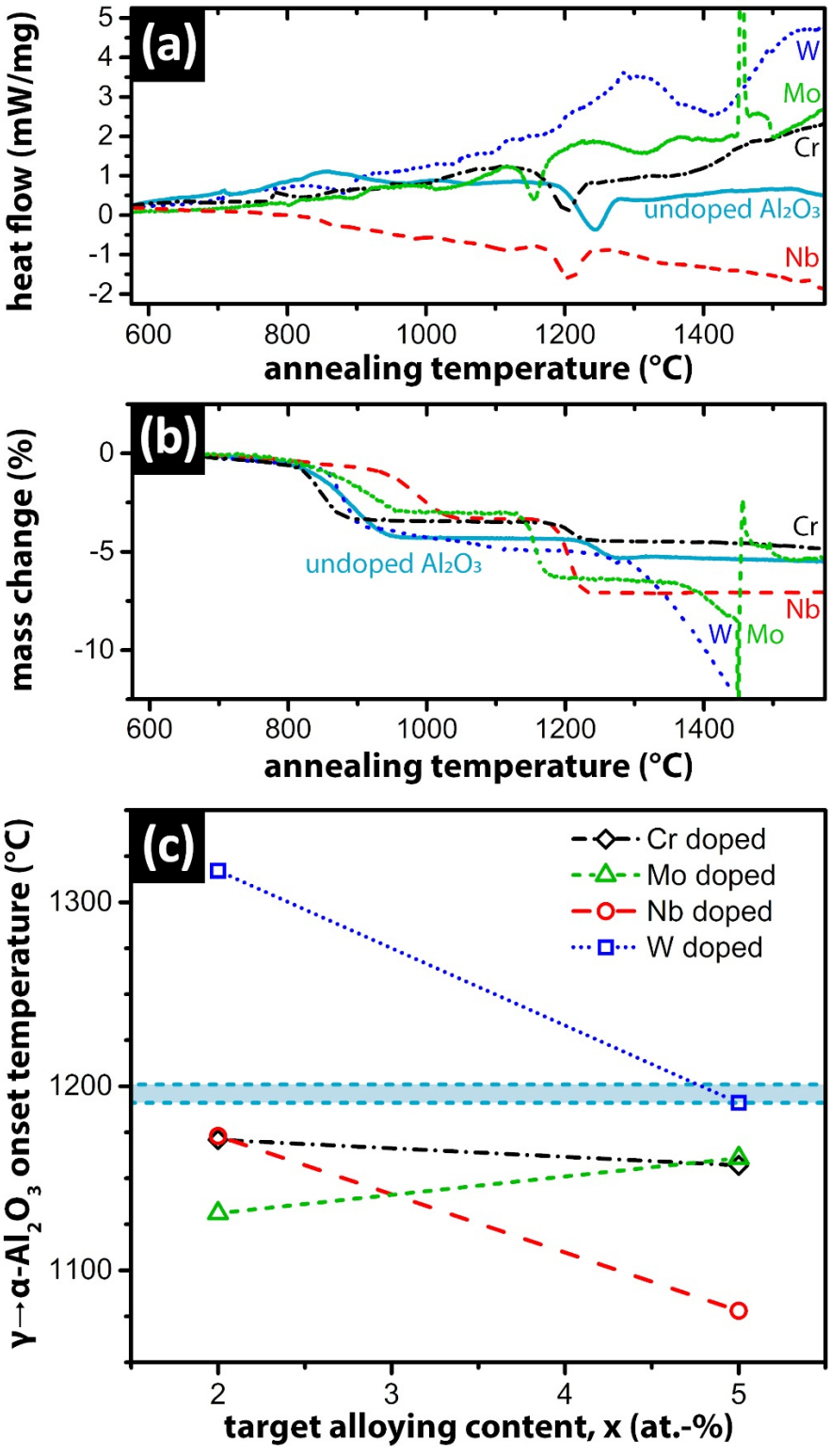

Figure 37: DSC evaluation of the doped coatings, considering the heat flow (a) and mass change (b) of the coating powders. (c) Summary of onset temperatures for the γ- to α-Al_2O_3 transformation of pure and Cr, Mo, Nb, or W doped Al_2O_3 coatings.

After the DSC measurement in O_2 containing atmosphere up to 1600 °C, pure as well as 2 at.-% Mo, W doped coatings exhibit a single crystalline α- Al_2O_3 structure (**Figure 38b**). Coatings produced from 2 at.-% Cr alloyed targets exhibit a marginal phase separation of Cr_2O_3. Coatings prepared from Nb doped coatings, exhibit separation of $AlNbO_4$ during the annealing occurs already with target doping contents of 2 at.-%. Even higher Nb concentrations within the coating (5 at.-% in the target) lead to an additional niobium oxide formation. The coatings prepared from 5 at.-% Cr alloyed targets clearly show a phase separation into α-Al_2O_3 and Cr_2O_3, and those prepared from 5 at.-% W alloyed targets exhibit a rather complex structure composed of $AlWO_4$ and other tungsten oxides phases next to α-Al_2O_3.

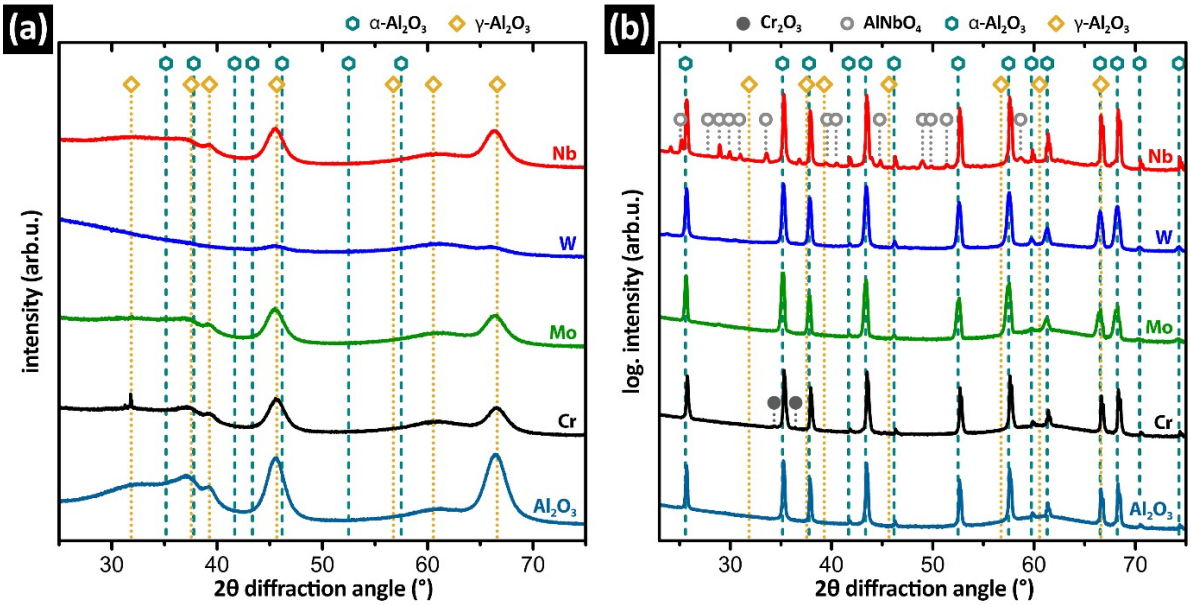

Figure 38: XRD spectra (4 h long-term data acquisition) of the coating powders from 2 at.-% alloyed targets in their as deposited state (a) and after the DSC annealing up to 1600 °C (b).

As especially the coatings prepared from 2 at.-% transition metal alloyed Al targets attracted our attention (in particular W doped targets, because of their increased growth rate, good mechanical properties), we studied these coatings in more detailed by in-situ XRD measurements during annealing in synthetic air up to 1200 °C (XPERT III, PANalytical, equipped with an Anton Paar HTK 1200 N reaction chamber). Starting at 600 °C, every 20 °C an XRD pattern was recorded (after an isothermal holding segment of 60 min, the measurement itself from 30 to 90° diffraction angles took additional 20 min). Because of the long annealing times, the phase transformations will be detected at lower temperatures as during the rather fast dynamical DSC measurements (heating rate of 10 K/min). The undoped Al_2O_3 coating exhibit a rather stable structure based on cubic γ-Al_2O_3 up to around 1050 °C, where first indicationsfor the formation of α-Al_2O_3 can be detected, see **Figure 39a** at diffraction angles of 57°. However, the phase transformation from undoped γ-Al_2O_3 to α-Al_2O_3 spans over a rather huge temperature window, especially when considering the rather long annealing times. At 1150 °C, γ-Al_2O_3 can still be detected. We contribute this to the stabilizing effect of the surface [277] within the nanocrystalline coating structure and variation in crystallite sizes. Cr containing coatings show a rather similar behavior during these in-situ XRD studies, therefore not shown in **Figure 39**. The coatings prepared from Mo containing Al targets, clearly show that a significant α-Al_2O_3 formation starts already at 1000 °C, and γ-Al_2O_3 can only be detected until 1100 °C. As mentioned above and in chapter 6, these coatings are characterized by a rather high defect density (due to the formation of volatile Mo-oxides, which influence the growth morphology of these coatings), which trigger the phase transformation in **Figure 39b**.

The coatings prepared from the 2 at.-% Nb containing Al targets exhibit at 1000 °C first indications for the formation of α-Al_2O_3 (**Figure 39c**), similar to the Al_2O_3 coatings. However, the phase transformation seems to be more homogeneous, as already

after 1100 °C almost no γ-Al_2O_3 can be detected anymore. The coatings prepared from the 2 at.-% W containing Al targets, exhibit at 800 °C the formation of γ-Al_2O_3 (**Figure 39d**), which coincides with exothermic feature between 800 and 1000 °C during DSC measurements (**Figure 37a**) . The formation of α-Al_2O_3 can only be detected at ~1100 °C, but even more important even after annealing at 1200 °C no strong XRD peaks at α-Al_2O_3 positions can be detected, contrary to the other coatings, see **Figure 39**.

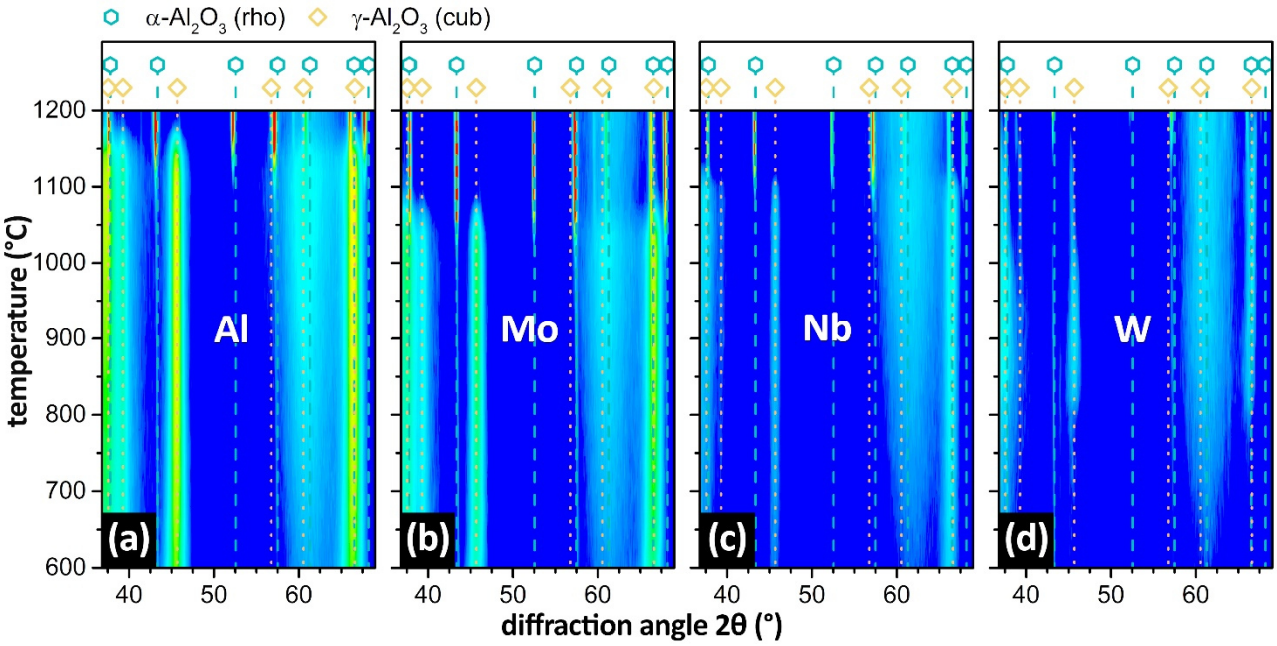

Figure 39: Stepwise non-ambient XRD measurements from 600 °C to 1200 °C with 2 at.-% target doping. The transformation from γ- to α-Al_2O_3 is clearly visible for undoped Al_2O_3 coatings (a), Mo doped (b), Nb doped (c), and W doped(d) coatings.

In order to retard the phase transformation from γ-Al_2O_3 to α-Al_2O_3, grain growth

should be inhibited, as smaller grains promote the γ-phase over the α-phase, due to the significantly larger surface energy of α [277]. Here, W can have an important impact, as their diffusivity is low allowing to activate the solute drag effect [287-289], which is based on the interaction between interfaces (here grain boundary) and the solute (here W). The solute is dragged with the migrating interface and if its diffusivity is significantly lower, it causes an effective counteracting force on that interface retarding its mobility. As a result, grain growth is reduced, until the thermal energy induced grain growth driving force overcomes the energetic barrier of the W solutes. As the phase transformation from γ-Al_2O_3 to α-Al_2O_3 is also connected with nucleation and mobility of phase boundaries into the untransformed region, the W solute influence also this process until a certain threshold phase growth velocity is reached [288]. As a result the γ-Al_2O_3 to α-Al_2O_3 transformation is retarded and even after long term annealing treatments (like in our in-situ XRD measurements) at 1200 °C still the XRD reflexes for α-Al_2O_3 are relatively broad, indicating still a small grain size.

8 Conclusion

The reported studies provide a detailed insight into the protective effects that can derive from phase transformations, but also from modifying the phase transition onset-temperatures.

It has been shown that phase transitions at the coating surface can be facilitated by applying coatings with a tailored stability, that allow for a phase transition that would not be possible with less reactive compounds. At the same time, some materials like metallic Mo (that can easily be deposited as a coating) can catalytically promote transformations of hydrocarbons to lubricating graphite-based tribofilms. Wear protective coatings have reached an evolutionary step, where they are not limited to being a sacrificial hard surface, but also unfold a secondary protective effect. This secondary protective effect generates lubricating compounds out of the coatings wear debris that in return lubricates the tribological contact and reduces coating wear, initializing a protective loop. Catalytically induced phase transitions at the coating surface even have the potential to proactively prevent wear completely.

The generation mechanism for the in-situ generation of WS_2 (and MoS_2 equally) was discovered and, as demonstrated in **Figure 40**, is based on the formation of oxide intermediates. The tailored tungsten nitride coating was successfully applied to facilitate the necessary oxidation. In the severe conditions of single asperity contact, WO_3 becomes instable and a chemically induced transformation to WS_2 occurs. The initially amorphous WS_2 self-assembles under shear stress to form characteristic lubricating sandwich structures. This concept allows very low friction at extraordinary wear protection.

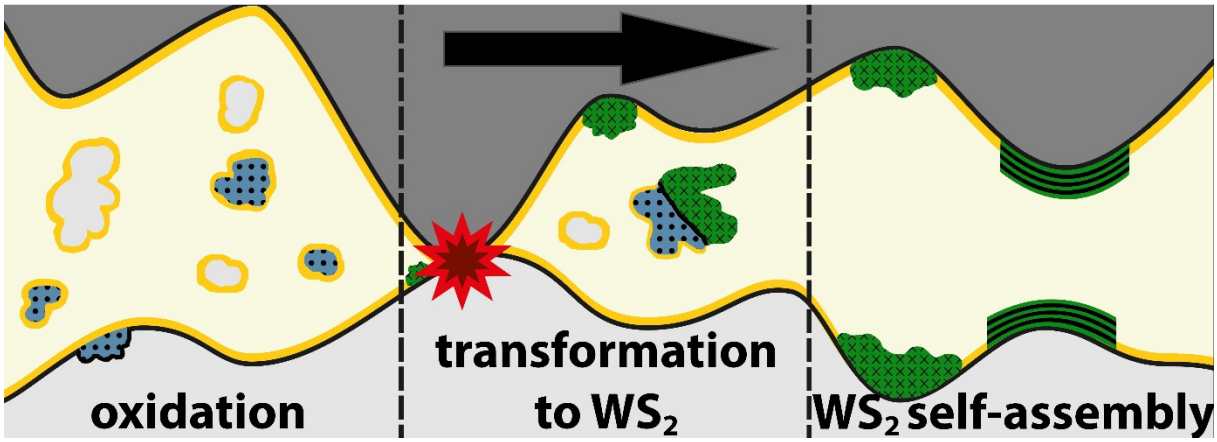

Figure 40: Highlight I, reaction pathway for the in-situ generation of WS_2

The same phase transformation is also facilitated by metallic Mo surfaces, showing clear evidence for the formation of lubricating S-Mo-S sandwich structures, see **Figure 41**. At the same time, Mo surfaces are able to catalytically break down lubricating hydrocarbons in order to form oil-derived graphite based tribofilms. Both in-situ formations (MoS_2 and Graphite) appear to be competitive effects, as the phase transformation to lubricating MoS_2 can occur at less severe conditions and prevents the formation of graphite. Nevertheless, a carbon-rich layer is formed on top of MoS_2 and the graphite formation can potentially act as a very powerful 'second stage' reaction, sustaining wear protection if the oil additives are depleted.

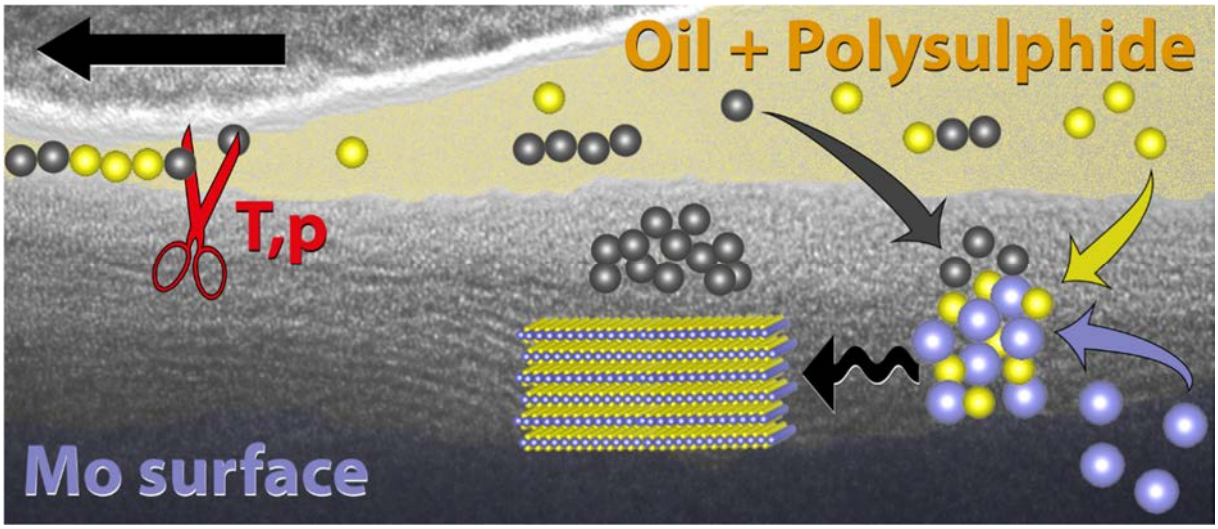

Figure 41: Highlight II, formation of MoS_2 on metallic Mo under a carbon film, produced by catalytic breaking of hydrocarbon bonds.

Focusing on phase transformations of the whole coating itself (considering the tailored phase transformation of γ-Al_2O_3) we first need to conclude on the technological benefits of transition metal doping. While the process stability can be improved with Mo, Cr, and W micro-alloyed targets only W unfolds a pronounced rebound sputtering effect (**Figure 42**) that leads to increased sputter rates and poisoning retardation. At the same time, low-level W doped coatings possess improved mechanical properties and an interesting morphology that can increase substrate adhesion due to low compressive stresses at the substrate – coating interface.

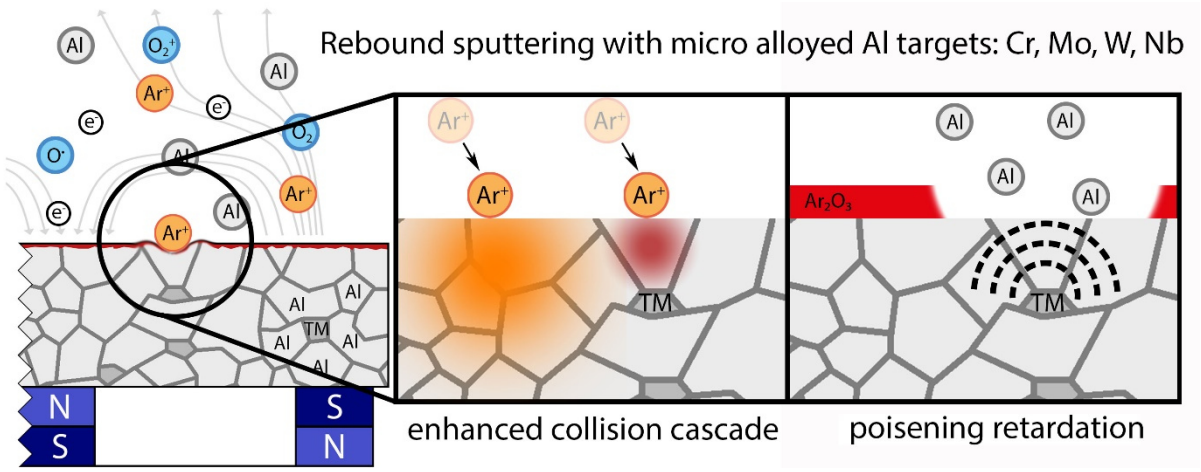

Figure 42: Highlight III, Al_2O_3 deposition rate increase and poisoning retardation by rebound sputtering with heavy element (W) micro-alloyed Al targets.

The thermal stability of the doped γ-Al_2O_3 is significantly influenced by transition metal substitutes on the metallic sublattice. It is possible to shift the γ-Al_2O_3 to α-Al_2O_3 transition up to temperatures above 1200°C by doping with W (**Figure 43**). The reason for the shift of the phase transformation lies in its high surface are (with a lower surface energy than α-Al_2O_3). W doping increases the defect density and hence the surface area, and at the same time prevents recovery and recrystallization via the solute drag effect. The solute drag also slows down moving phase transformation interfaces supporting the phase transformation retardation.

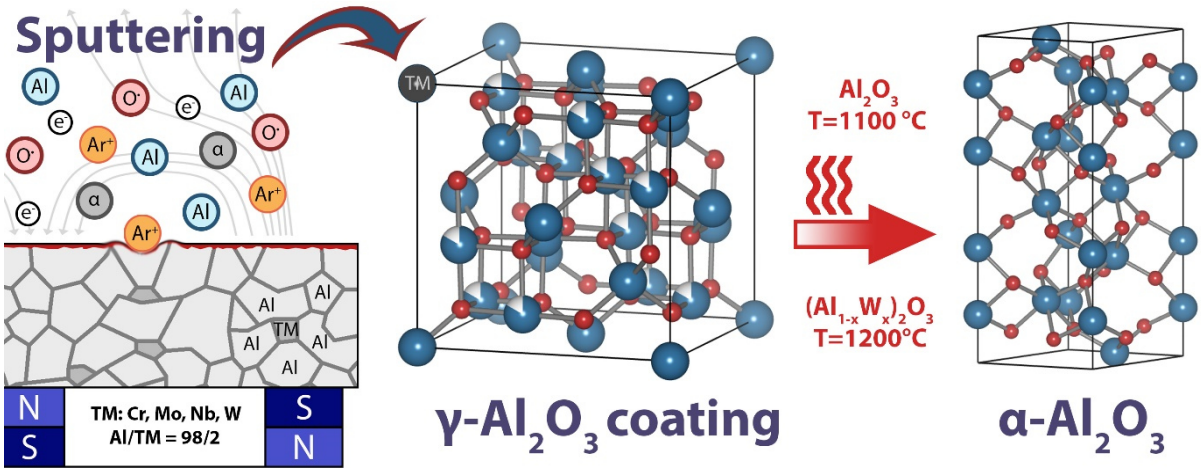

Figure 43: Highlight IV, significantly delayed γ-Al_2O_3 to α-Al_2O_3 transition due to increased surface area and the solute drag by W-dopants.

Concluding, this work highlights that phase transformations do not necessarily lead to a failure of a coating. For many applications where a phase transformations like the γ-Al_2O_3 to α-Al_2O_3 transition would imply a failure, it is possible to (within limits) push the transformation onsets above the application conditions.

9 Contribution to the Field

The material of the chapters 4 to 7 was prepared for publication in the following papers:

I

How to get noWear? – A new take on the design of in-situ formed high performing low-friction tribofilms

B. Kohlhauser[1,2], M. Rodríguez Ripoll[2], H. Riedl[1], C.M. Koller[1], N. Koutna[1], A. Amsüss[3], H. Hutter[3], G. Ramirez[4], C. Gachot[2,5], A. Erdemir[4], and P. H. Mayrhofer[1]

[1] Institute of Materials Science and Technology, TU Wien, A-1060 Vienna, Austria
[2] AC²T research GmbH, Wiener Neustadt, Austria
[3] Institute of Chemical Technologies and Analytics, TU Wien, A-1060 Vienna, Austria
[4] Argonne National Laboratory, 60439 Illinois, United States of America
[5] Institute for Engineering Design and Logistics Engineering, TU Wien, A-1060 Vienna, Austria

Submitted to Scientific report on the 10.12.2018

II

Reactive self assembly of MoS_2-based nanoclusters for low friction

Bernhard Kohlhauser[1,2], Sara Spiller[2], Carmen I. Vladu[3], Carsten Gachot[4], Paul H. Mayrhofer[1], Manel Rodríguez Ripoll[1]

[1] Institute of Materials Science and Technology, TU Wien, A-1060, Austria
[2] AC2T research GmbH, Wiener Neustadt, Austria
[3] CEST GmbH, Wiener Neustadt, Austria
[4] Institute of Engineering Design and Logistics Engineering, TU Wien, A-1060 Vienna, Austria

In final preparation for submission to Nanoscale (8.12.2018)

III

Enhancing the reactive deposition and phase formation of PVD Al_2O_3 thin films with transition metal dopants

B. Kohlhauser[1,2], H. Riedl[1], C.M. Koller[1], V. Paneta[3], D. Primetzhofer[3], S. Kolozsvári[4], and P. H. Mayrhofer[1]

[1] Institute of Materials Science and Technology, TU Wien, A-1060 Vienna, Austria
[2] AC2T research GmbH, A-2700, Wiener Neustadt, Austria
[3] Department of Physics and Astronomy, Uppsala University, SE-75120 Uppsala, Sweden
[4] Plansee Composite Materials GmbH, D-86983 Lechbruck am See, Germany

In final preparation for submission to Surface & Coating Technology (10.12.2018)

IV

Thermal stability of transition metal doped γ-Al_2O_3 thin films

B. Kohlhauser[1,2], H. Riedl[1], T. Wojcik[1], S. Kolozsvári[3], C. Gachot[2,4], and P. H. Mayrhofer[1]

[1] Institute of Materials Science and Technology, TU Wien, A-1060 Vienna, Austria
[2] AC2T research GmbH, A-2700 Wiener Neustadt, Austria
[3] Plansee Composite Materials GmbH, D-86983 Lechbruck am See, Germany
[4] Institute for Engineering Design and Logistics Engineering, TU Wien, A-1060 Vienna, Austria

In final preparation for submission to Scripta Materialia (10.12.2018)

10 Financial and Experimental Support

This work was funded by the Austrian COMET-Program (Project K2 X-Tribology, Grant no. 849109) and has been carried out within the TU Wien, Argonne Laboratory (USA), and the Excellence Centre for Tribology AC2T research GmbH. TEM and SEM investigations were carried out using the USTEM facilities at the TU Wien, Austria. Thanks is also due to the X-ray center (XRC) and the Institute of Chemical Technologies and Analytics at the TU Wien, Austria, for evaluating structure and chemical compositions.

The author would also like to thank the Austrian Marshall Plan Foundation for their financial support, making the research fellowship at Argonne National Laboratory possible.

11 References

[1] S. Chu, A. Majumdar, Opportunities and challenges for a sustainable energy future, Nature, 488 (2012) 294.

[2] K. Holmberg, P. Andersson, A. Erdemir, Global energy consumption due to friction in passenger cars, Tribology International, 47 (2012) 221-234.

[3] K. Holmberg, A. Erdemir, Influence of tribology on global energy consumption, costs and emissions, Friction, 5 (2017) 263-284.

[4] World Energy Council, Global Transport Scenarios 2050, World Energy Council, 2011.

[5] A. Erdemir, C. Donnet, Tribology of diamond-like carbon films: recent progress and future prospects, Journal of Physics D: Applied Physics, 39 (2006) R311.

[6] S.V. Johnston, S.V. Hainsworth, Effect of DLC coatings on wear in automotive applications, Surface Engineering, 21 (2005) 67-71.

[7] J. Vetter, 60 Years of DLC coatings: Historical highlights and technical review of cathodic arc processes to synthesize various DLC types, and their evolution for industrial applications, 2014.

[8] T. Haque, A. Morina, A. Neville, Influence of friction modifier and antiwear additives on the tribological performance of a non-hydrogenated DLC coating, Surface and Coatings Technology, 204 (2010) 4001-4011.

[9] B. Podgornik, J. Vizintin, S. Strnad, K. Stana-Kleinschek, Tribological interactions between DLC coatings and lubricants, Tribo Test, 14 (2008) 81-95.

[10] M. Kalin, J. Kogovšek, M. Remškar, Nanoparticles as novel lubricating additives in a green, physically based lubrication technology for DLC coatings, Wear, 303 (2013) 480-485.

[11] M. Nosonovsky, B. Bhushan, Green Tribology: Biomimetics, Energy Conservation and Sustainability, Springer2012.

[12] M. Rodríguez Ripoll, V. Totolin, C. Gabler, J. Bernardi, I. Minami, Diallyl disulphide as natural organosulphur friction modifier via the in-situ tribo-chemical formation of tungsten disulphide, Applied Surface Science, 428 (2018) 659-668.

[13] B.P. Bewlay, M. Weimer, T. Kelly, A. Suzuki, P.R. Subramanian, The Science, Technology, and Implementation of TiAl Alloys in Commercial Aircraft Engines, MRS Online Proceedings Library, 1516 (2013) 49-58.

[14] J. Aguilara, A. Schievenbuschb, O. Kättlitzc, Qualification of a casting technology for production of Titanium aluminide components for aero-engine applications, Advanced Materials Research, 2011, pp. 563-568.

[15] M.B. Thomas, M.-P., Processing and Characterization of TiAl based Alloys: Towards an Industrial Scale, AerospaceLab Journal, (2011).

[16] K. Bobzin, L. Zhao, N. Kopp, T. Warda, Feasibility study of plasma sprayed Al2O3 coatings as diffusion barrier on CFC components, Front. Mech. Eng., 7 (2012) 371-375.

[17] R. Cremer, M. Witthaut, K. Reichert, D. Neuschütz, Surface and interface analysis of PVD Al-O-N and γ-Al2O3 diffusion barriers, Fresenius' Journal of Analytical Chemistry, 365 (1999) 158-162.

[18] R. Cremer, M. Witthaut, K. Reichert, M. Schierling, D. Neuschütz, Thermal stability of Al-O-N PVD diffusion barriers, Surface and Coatings Technology, 108-109 (1998) 48-58.

[19] K.G. Schmitt-Thomas, U. Dietl, Diffusion barriers of Al2O3 to reduce the bondcoat-oxidation of MCrAlY alloys, Werkst Korros, 43 (1992) 492-495.

[20] P.H. Mayrhofer, Skriptum "Werkstoffkunde metallischer Werkstoffe", DOI (2017).

[21] D.A. Porter, K.E. Easterling, Phase transformations in Metals and Alloys, 2 ed., Springer-Science+Business Media, B.V. 1992.

[22] P.H. Mayrhofer, Skriptum " Phase transitions", 2018.

[23] D.M. Mattox, Chapter 10 - Atomistic Film Growth and Some Growth-Related Film Properties, in: D.M. Mattox (Ed.) Handbook of Physical Vapor Deposition (PVD) Processing (Second Edition), William Andrew Publishing, Boston, 2010, pp. 333-398.

[24] Y. Mnyukh, Mechanism and Kinetics of Phase Transitions and Other Reactions in Solids American Journal of Condensed M atter Physics, DOI (2013).

[25] C.B. Carter, M.G. Norton, Ceramic Materials, Springer, New York, NY2007.

[26] H.K.D.H. Bhadeshia, C.M. Wayman, Phase Transformations: Nondiffusive, in: D.E. Laughlin, K. Hono (Eds.) Physical Metallurgy (Fifth Edition), Elsevier, Oxford, 2014, pp. 1021-1072.

[27] F. Balima, A. Largeteau, Phase transformation of alumina induced by high pressure spark plasma sintering (HP-SPS), Scripta Materialia, 158 (2019) 20-23.

[28] W. Duan, R.M. Wentzcovitch, K.T. Thomson, First-principles study of high-pressure alumina polymorphs, Physical Review B, 57 (1998) 10363-10369.

[29] A. Jayaraman, Influence of Pressure on Phase Transitions, Annual Review of Materials Science, 2 (1972) 121-142.

[30] Q. Li, Y. Guo, M. Zhang, X. Ge, Pressure-induced structural phase transformation and superconducting properties of titanium mononitride, Solid State Communications, 271 (2018) 16-20.

[31] P. Jost, Lubrication (Tribology) - A report on the present position and industry's needs, Department of Education and Science, London, UK, 1966.

[32] I.M. Hutchings, Leonardo da Vinci′s studies of friction, Wear, 360-361 (2016) 51-66.

[33] Z. Deng, A. Smolyanitsky, Q. Li, X.-Q. Feng, R.J. Cannara, Adhesion-dependent negative friction coefficient on chemically modified graphite at the nanoscale, Nature Materials, 11 (2012) 1032.

[34] S.C. Lim, M.F. Ashby, Overview no. 55 Wear-Mechanism maps, Acta Metallurgica, 35 (1987) 1-24.

[35] P.-R. Cha, D.J. Srolovitz, T. Kyle Vanderlick, Molecular dynamics simulation of single asperity contact, Acta Materialia, 52 (2004) 3983-3996.

[36] A. Megalingam, M.M. Mayuram, A Comprehensive Elastic-Plastic Single-Asperity Contact Model, Tribology Transactions, 57 (2014) 324-335.

[37] O. Reynolds, On the Theory of Lubrication and Its Application to Mr. Beauchamp Tower's Experiments, Including an Experimental Determination of the Viscosity of Olive Oil, Philosophical Transactions of the Royal Society, DOI (1886).

[38] B. Jacobson, The Stribeck memorial lecture, Tribology International, 36 (2003) 781-789.

[39] C. Gachot, A. Rosenkranz, S.M. Hsu, H.L. Costa, A critical assessment of surface texturing for friction and wear improvement, Wear, 372-373 (2017) 21-41.

[40] M. Kalin, Influence of flash temperatures on the tribological behaviour in low-speed sliding: a review, Materials Science and Engineering: A, 374 (2004) 390-397.

[41] B. Bhushan, Modern Tribology Handbook, CRC Press2001.

[42] P.H. Mayrhofer, Skriptum "Oberflächentechnik".

[43] D.R. Milner, G.W. Rowe, Fundamentals of Solid-Phase Welding, Metallurgical Reviews, 7 (1962) 433-480.

[44] S. Eder, Simulation of Wear Processes Using Molecular Dynamics (MD) Simulations, OeTG Symposium, 2007.

[45] N. Fang, P.S. Pai, S. Mosquea, The effect of built-up edge on the cutting vibrations in machining 2024-T351 aluminum alloy, The International Journal of Advanced Manufacturing Technology, 49 (2010) 63-71.

[46] H. Riedl, J. Zálešák, M. Arndt, P. Polcik, D. Holec, P.H. Mayrhofer, Ab initio studies on the adsorption and implantation of Al and Fe to nitride materials, Journal of Applied Physics, 118 (2015).

[47] M. Berger, S. Hogmark, Tribological properties of selected PVD coatings when slid against ductile materials, Wear, 252 (2002) 557-565.

[48] M. Berger, S. Hogmark, Evaluation of TiB2 coatings in sliding contact against aluminium, Surface and Coatings Technology, 149 (2002) 14-20.

[49] A. Ghiotti, S. Bruschi, Tribological behaviour of DLC coatings for sheet metal forming tools, Wear, 271 (2011) 2454-2458.

[50] M. Lahres, P. Müller-Hummel, O. Doerfel, Applicability of different hard coatings in dry milling aluminium alloys, Surface and Coatings Technology, 91 (1997) 116-121.

[51] A. Blomberg, M. Olsson, S. Hogmark, Wear mechanisms and tribo mapping of Al2O3 and SiC in dry sliding, Wear, 171 (1994) 77-89.

[52] G. Gassner, P.H. Mayrhofer, K. Kutschej, C. Mitterer, M. Kathrein, Magnéli phase formation of PVD Mo–N and W–N coatings, Surface and Coatings Technology, 201 (2006) 3335-3341.

[53] W.G. Sawyer, T.A. Blanchet, Lubrication of Mo, W, and their Alloys with H2S gas admixtures to room temperature air, Wear, 225-229 (1999) 581-586.

[54] I.L. Singer, T.L. Mogne, C. Donnet, J.M. Martin, Friction behavior and wear analysis of sic sliding against mo in so2, o2 and h2s at gas pressures between 4 and 40 pa, Tribology Transactions, 39 (1996) 950-956.

[55] H. Nyberg, J. Sundberg, E. Särhammar, T. Nyberg, U. Jansson, S. Jacobson, Tribochemical Formation of Sulphide Tribofilms from a Ti–C–S Coating Sliding Against Different Counter Surfaces, Tribology Letters, 56 (2014) 563-572.

[56] J. Sundberg, H. Nyberg, E. Särhammar, K. Kádas, L. Wang, O. Eriksson, T. Nyberg, S. Jacobson, U. Jansson, Tribochemically Active Ti–C–S Nanocomposite Coatings, Materials Research Letters, 1 (2013) 148-155.

[57] H. Riedl, High Temperature, Oxidation and Wear Resistant Coatings, TU Wien, 2015.

[58] J.H. Wu, D.A. Rigney, M.L. Falk, J.H. Sanders, A.A. Voevodin, J.S. Zabinski, Tribological behavior of WC/DLC/WS2 nanocomposite coatings, Surface and Coatings Technology, 188-189 (2004) 605-611.

[59] G. Gassner, P.H. Mayrhofer, K. Kutschej, C. Mitterer, M. Kathrein, A New Low Friction Concept for High Temperatures: Lubricious Oxide Formation on Sputtered VN Coatings, Tribology Letters, 17 (2004) 751-756.

[60] A. Magnéli, B.M. Oughton, Studies on the Vanadium Pentoxide - Molybdenum Trioxide System. I. The Relation between the Crystal Structures of the two Oxides.

, Acta Chem. Scand., DOI (**1951**) 581.

[61] A.A. Voevodin, C. Muratore, S.M. Aouadi, Hard coatings with high temperature adaptive lubrication and contact thermal management: review, Surface and Coatings Technology, 257 (2014) 247-265.

[62] A. Erdemir, A crystal-chemical approach to lubrication by solid oxides, Tribology Letters, 8 (2000) 97.

[63] A. Erdemir, R.A. Erck, Effect of niobium interlayer on high-temperature sliding friction and wear of silver films on alumina, Tribology Letters, 2 (1996) 23-36.

[64] A. Wells, D.J. De Wet, The use of platinum in thin tribological coatings, Wear, 127 (1988) 269-281.

[65] A.A. Voevodin, T.A. Fitz, J.J. Hu, J.S. Zabinski, Nanocomposite tribological coatings with "chameleon" surface adaptation, Journal of Vacuum Science & Technology A, 20 (2002) 1434-1444.

[66] F.P. Bowden, J.N. Gregory, D. Tabor, Lubrication of Metal Surfaces by Fatty Acids, Nature, 156 (1945) 97.

[67] P. Kapsa, J.M. Martin, Boundary lubricant films: a review, Tribology International, 15 (1982) 37-42.

[68] N.N. Gosvami, J.A. Bares, F. Mangolini, A.R. Konicek, D.G. Yablon, R.W. Carpick, Mechanisms of antiwear tribofilm growth revealed in situ by single-asperity sliding contacts, Science, 348 (2015) 102-106.

[69] S. Jahanmir, Wear of AISI 4340 steel under boundary lubrication, Wear, 74 (1981) 51-65.

[70] A. Morina, A. Neville, Tribofilms: aspects of formation, stability and removal, Journal of Physics D: Applied Physics, 40 (2007) 5476.

[71] M.L.S. Fuller, M. Kasrai, G.M. Bancroft, K. Fyfe, K.H. Tan, Solution decomposition of zinc dialkyl dithiophosphate and its effect on antiwear and thermal film formation studied by X-ray absorption spectroscopy, Tribology International, 31 (1998) 627-644.

[72] J.M. Martin, T. Onodera, C. Minfray, F. Dassenoy, A. Miyamoto, The origin of anti-wear chemistry of ZDDP, Faraday Discussions, 156 (2012) 311-323.

[73] H. Spikes, The History and Mechanisms of ZDDP, Tribology Letters, 17 (2004) 469-489.

[74] H. Spikes, Low- and zero-sulphated ash, phosphorus and sulphur anti-wear additives for engine oils, Lubrication Science, 20 (2008) 103-136.

[75] M. Ratoi, V.B. Niste, J. Zekonyte, WS2 nanoparticles - potential replacement for ZDDP and friction modifier additives, RSC Advances, 4 (2014) 21238-21245.

[76] A. Morina, A. Neville, M. Priest, J.H. Green, ZDDP and MoDTC interactions in boundary lubrication—The effect of temperature and ZDDP/MoDTC ratio, Tribology International, 39 (2006) 1545-1557.

[77] C. Grossiord, K. Varlot, J.M. Martin, T. Le Mogne, C. Esnouf, K. Inoue, MoS2 single sheet lubrication by molybdenum dithiocarbamate, Tribology International, 31 (1998) 737-743.

[78] C. Grossiord, J.M. Martin, T. Le Mogne, T. Palermo, In situ MoS2 formation and selective transfer from MoDPT films, Surface and Coatings Technology, 108-109 (1998) 352-359.

[79] J. Kogovšek, M. Kalin, Various MoS2-, WS2- and C-based micro- and nanoparticles in boundary lubrication, Tribology Letters, 53 (2014) 585-597.

[80] V.B. Niste, M. Ratoi, Tungsten dichalcogenide lubricant nanoadditives for demanding applications, Materials Today Communications, 8 (2016) 1-11.

[81] P. Rabaso, F. Dassenoy, F. Ville, M. Diaby, B. Vacher, T. Le Mogne, M. Belin, J. Cavoret, An Investigation on the Reduced Ability of IF-MoS2 Nanoparticles to Reduce Friction and Wear in the Presence of Dispersants, Tribology Letters, 55 (2014) 503-516.

[82] L. Rapoport, Y. Bilik, Y. Feldman, M. Homyonfer, S.R. Cohen, R. Tenne, Hollow nanoparticles of WS2 as potential solid-state lubricants, Nature, 387 (1997) 791.

[83] J. Tannous, F. Dassenoy, I. Lahouij, T. Le Mogne, B. Vacher, A. Bruhács, W. Tremel, Understanding the Tribochemical Mechanisms of IF-MoS2 Nanoparticles Under Boundary Lubrication, Tribology Letters, 41 (2011) 55-64.

[84] A. Tomala, B. Vengudusamy, M. Rodríguez Ripoll, A. Naveira Suarez, M. Remškar, R. Rosentsveig, Interaction Between Selected MoS2 Nanoparticles and ZDDP Tribofilms, Tribology Letters, 59 (2015) 26.

[85] G. Crisponi, V.M. Nurchi, J.I. Lachowicz, M. Peana, S. Medici, M.A. Zoroddu, Chapter 18 - Toxicity of Nanoparticles: Etiology and Mechanisms, in: A.M. Grumezescu (Ed.) Antimicrobial Nanoarchitectonics, Elsevier2017, pp. 511-546.

[86] M.A. Zoroddu, S. Medici, A. Ledda, V.A. Nurchi, J.I. Lachowicz, M. Peana, Toxicity of Nanoparticles, Current Medicinal Chemistry, 21 (2014) 3837-3853.

[87] A. Mnyusiwalla, A.S. Daar, P.A. Singer, 'Mind the gap': science and ethics in nanotechnology, Nanotechnology, 14 (2003) R9.

[88] F. Gustavsson, S. Jacobson, Diverse mechanisms of friction induced self-organisation into a low-friction material – An overview of WS2 tribofilm formation, Tribology International, 101 (2016) 340-347.

[89] M. Rodríguez Ripoll, V. Totolin, P.O. Bedolla, I. Minami, Methionine as a Friction Modifier for Tungsten Carbide-Functionalized Surfaces via in Situ Tribo-Chemical Reactions, ACS Sustainable Chemistry and Engineering, 5 (2017) 7030-7039.

[90] A. Neville, A. Morina, T. Haque, M. Voong, Compatibility between tribological surfaces and lubricant additives-How friction and wear reduction can be controlled by surface/lube synergies, Tribology International, 40 (2007) 1680-1695.

[91] A. Erdemir, G. Ramirez, O.L. Eryilmaz, B. Narayanan, Y. Liao, G. Kamath, S.K.R.S. Sankaranarayanan, Carbon-based tribofilms from lubricating oils, Nature, 536 (2016) 67.

[92] D. Berman, B. Narayanan, M.J. Cherukara, S.K.R.S. Sankaranarayanan, A. Erdemir, A. Zinovev, A.V. Sumant, Operando tribochemical formation of onion-like-carbon leads to macroscale superlubricity, Nature Communications, 9 (2018).

[93] N. Argibay, T.F. Babuska, J.F. Curry, M.T. Dugger, P. Lu, D.P. Adams, B.L. Nation, B.L. Doyle, M. Pham, A. Pimentel, C. Mowry, A.R. Hinkle, M. Chandross, In-situ tribochemical formation of self-lubricating diamond-like carbon films, Carbon, 138 (2018) 61-68.

[94] J. Musil, Hard and superhard nanocomposite coatings, Surface and Coatings Technology, 125 (2000) 322-330.

[95] P.H. Mayrhofer, R. Rachbauer, D. Holec, F. Rovere, J.M. Schneider, Protective Transition Metal Nitride Coatings, in: S. Hashmi, G.F. Batalha, C.J. Van Tyne, B. Yilbas (Eds.) Comprehensive Materials Processing, Elsevier, Oxford, 2014, pp. 355-388.

[96] K. Balasubramanian, S. Khare, D. Gall, Vacancy-induced mechanical stabilization of cubic tungsten nitride, Physical Review B, 94 (2016) 174111.

[97] S. Ganguli, L. Chen, T. Levine, B. Zheng, M. Chang, Development of tungsten nitride film as barrier layer for copper metallization, Journal of Vacuum Science & Technology B: Microelectronics and Nanometer Structures Processing, Measurement, and Phenomena, 18 (2000) 237-241.

[98] A.E. Geissberger, R.A. Sadler, F.A. Leyenaar, M.L. Balzan, Investigation of reactively sputtered tungsten nitride as high temperature stable Schottky contacts to GaAs, Journal of Vacuum Science & Technology A, 4 (1986) 3091-3094.

[99] Z. Wang, Z. Liu, Z. Yang, S. Shingubara, Characterization of sputtered tungsten nitride film and its application to Cu electroless plating, Microelectronic Engineering, 85 (2008) 395-400.

[100] K.S. Novoselov, A.K. Geim, S.V. Morozov, D. Jiang, Y. Zhang, S.V. Dubonos, I.V. Grigorieva, A.A. Firsov, Electric Field Effect in Atomically Thin Carbon Films, Science, 306 (2004) 666-669.

[101] D. Akinwande, N. Petrone, J. Hone, Two-dimensional flexible nanoelectronics, Nature Communications, 5 (2014) 5678.

[102] M. Chhowalla, H.S. Shin, G. Eda, L.-J. Li, K.P. Loh, H. Zhang, The chemistry of two-dimensional layered transition metal dichalcogenide nanosheets, Nature Chemistry, 5 (2013) 263.

[103] Z. Zeng, Z. Yin, X. Huang, H. Li, Q. He, G. Lu, F. Boey, H. Zhang, Single-Layer Semiconducting Nanosheets: High-Yield Preparation and Device Fabrication, Angewandte Chemie International Edition, 50 (2011) 11093-11097.

[104] M. Acerce, D. Voiry, M. Chhowalla, Metallic 1T phase MoS2 nanosheets as supercapacitor electrode materials, Nature Nanotechnology, 10 (2015) 313.

[105] X. Hong, J. Kim, S.-F. Shi, Y. Zhang, C. Jin, Y. Sun, S. Tongay, J. Wu, Y. Zhang, F. Wang, Ultrafast charge transfer in atomically thin MoS2/WS2 heterostructures, Nature Nanotechnology, 9 (2014) 682.

[106] A. Raja, A. Chaves, J. Yu, G. Arefe, H.M. Hill, A.F. Rigosi, T.C. Berkelbach, P. Nagler, C. Schüller, T. Korn, C. Nuckolls, J. Hone, L.E. Brus, T.F. Heinz, D.R. Reichman, A. Chernikov, Coulomb engineering of the bandgap and excitons in two-dimensional materials, Nature Communications, 8 (2017) 15251.

[107] L.C. Flatten, Z. He, D.M. Coles, A.A.P. Trichet, A.W. Powell, R.A. Taylor, J.H. Warner, J.M. Smith, Room-temperature exciton-polaritons with two-dimensional WS2, Scientific Reports, 6 (2016) 33134.

[108] P. Jiang, X. Qian, X. Gu, R. Yang, Probing Anisotropic Thermal Conductivity of Transition Metal Dichalcogenides MX2 (M = Mo, W and X = S, Se) using Time-Domain Thermoreflectance, Advanced materials (Deerfield Beach, Fla.), 29 (2017).

[109] G. Zhu, J. Liu, Q. Zheng, R. Zhang, D. Li, D. Banerjee, D.G. Cahill, Tuning thermal conductivity in molybdenum disulfide by electrochemical intercalation, Nature Communications, 7 (2016) 13211.

[110] Q. Liu, X. Li, Z. Xiao, Y. Zhou, H. Chen, A. Khalil, T. Xiang, J. Xu, W. Chu, X. Wu, J. Yang, C. Wang, Y. Xiong, C. Jin, P.M. Ajayan, L. Song, Stable Metallic 1T-WS2 Nanoribbons Intercalated with Ammonia Ions: The Correlation between Structure and Electrical/Optical Properties, Advanced Materials, 27 (2015) 4837-4844.

[111] C. Tsai, F. Abild-Pedersen, J.K. Nørskov, Tuning the MoS2 Edge-Site Activity for Hydrogen Evolution via Support Interactions, Nano Letters, 14 (2014) 1381-1387.

[112] X.-L. Fan, Y. Yang, P. Xiao, W.-M. Lau, Site-specific catalytic activity in exfoliated MoS2 single-layer polytypes for hydrogen evolution: basal plane and edges, Journal of Materials Chemistry A, 2 (2014) 20545-20551.

[113] S. Xu, Z. Lei, P. Wu, Facile preparation of 3D MoS2/MoSe2 nanosheet–graphene networks as efficient electrocatalysts for the hydrogen evolution reaction, Journal of Materials Chemistry A, 3 (2015) 16337-16347.

[114] Y. Yan, B. Xia, N. Li, Z. Xu, A. Fisher, X. Wang, Vertically oriented MoS2 and WS2 nanosheets directly grown on carbon cloth as efficient and stable 3-dimensional hydrogen-evolving cathodes, Journal of Materials Chemistry A, 3 (2015) 131-135.

[115] L. Wang, X. Zhou, T. Ma, D. Liu, L. Gao, X. Li, J. Zhang, Y. Hu, H. Wang, Y. Dai, J. Luo, Superlubricity of a graphene/MoS2 heterostructure: a combined experimental and DFT study, Nanoscale, 9 (2017) 10846-10853.

[116] Y. Chen, J. Xi, D.O. Dumcenco, Z. Liu, K. Suenaga, D. Wang, Z. Shuai, Y.-S. Huang, L. Xie, Tunable Band Gap Photoluminescence from Atomically Thin Transition-Metal Dichalcogenide Alloys, ACS Nano, 7 (2013) 4610-4616.

[117] H. Li, Q. Zhang, X. Duan, X. Wu, X. Fan, X. Zhu, X. Zhuang, W. Hu, H. Zhou, A. Pan, X. Duan, Lateral Growth of Composition Graded Atomic Layer MoS2(1–x)Se2x Nanosheets, Journal of the American Chemical Society, 137 (2015) 5284-5287.

[118] Y. Chen, D.O. Dumcenco, Y. Zhu, X. Zhang, N. Mao, Q. Feng, M. Zhang, J. Zhang, P.-H. Tan, Y.-S. Huang, L. Xie, Composition-dependent Raman modes of Mo1−xWxS2 monolayer alloys, Nanoscale, 6 (2014) 2833-2839.

[119] D.O. Dumcenco, H. Kobayashi, Z. Liu, Y.-S. Huang, K. Suenaga, Visualization and quantification of transition metal atomic mixing in Mo1−xWxS2 single layers, Nature Communications, 4 (2013) 1351.

[120] K. Momma, F. Izumi, VESTA 3 for three-dimensional visualization of crystal, volumetric and morphology data, Journal of Applied Crystallography, 44 (2011) 1272-1276.

[121] C. Donnet, J.M. Martin, T. Le Mogne, M. Belin, The origin of super-low friction coefficient of MoS2 coatings in various environments, Tribology Series, 1994, pp. 277-284.

[122] J.M. Martin, C. Donnet, T. Le Mogne, T. Epicier, Superlubricity of molybdenum disulphide, Physical Review B, 48 (1993) 10583-10586.

[123] J.M. Martin, H. Pascal, C. Donnet, T. Le Mogne, J.L. Loubet, T. Epicier, Superlubricity of MoS2: crystal orientation mechanisms, Surface and Coatings Technology, 68-69 (1994) 427-432.

[124] W.E. Jamison, Structure and Bonding Effects on the Lubricating Properties of Crystalline Solids, A S L E Transactions, 15 (1972) 296-305.

[125] R. Zallen, M. Slade, Rigid-layer modes in chalcogenide crystals, Physical Review B, 9 (1974) 1627.

[126] M.B. Peterson, Friction and Wear Investigation of Molybdenum Disulfide I : Effect of Moisture, NACA, 1953.

[127] G. Levita, P. Restuccia, M.C. Righi, Graphene and MoS2 interacting with water: A comparison by ab initio calculations, Carbon, 107 (2016) 878-884.

[128] S. Watanabe, J. Noshiro, S. Miyake, Tribological characteristics of WS2/MoS2 solid lubricating multilayer films, Surface and Coatings Technology, 183 (2004) 347-351.

[129] J.S. Zabinski, M.S. Donley, S.V. Prasad, N.T. McDevitt, Synthesis and characterization of tungsten disulphide films grown by pulsed-laser deposition, Journal of Materials Science, 29 (1994) 4834-4839.

[130] T. Polcar, A. Cavaleiro, Review on self-lubricant transition metal dichalcogenide nanocomposite coatings alloyed with carbon, Surface and Coatings Technology, 206 (2011) 686-695.

[131] T. Polcar, A. Cavaleiro, Self-adaptive low friction coatings based on transition metal dichalcogenides, Thin Solid Films, 519 (2011) 4037-4044.

[132] T. Polcar, F. Gustavsson, T. Thersleff, S. Jacobson, A. Cavaleiro, Complex frictional analysis of self-lubricant W-S-C/Cr coating, Faraday Discussions, 156 (2012) 383-401.

[133] T. Polcar, A. Nossa, M. Evaristo, A. Cavaleiro, Nanocomposite coatings of carbon-based and transition metal dichalcogenides phases: A review, Reviews on Advanced Materials Science, 15 (2007) 118-126.

[134] M.R. Hilton, P.D. Fleischhauer, Structural, chemical, and tribological studies of sputter-deposited MoS2 solid lubricants films, MRS Proceedings, DOI (1991).

[135] A.A. Tedstone, D.J. Lewis, R. Hao, S.-M. Mao, P. Bellon, R.S. Averback, C.P. Warrens, K.R. West, P. Howard, S. Gaemers, S.J. Dillon, P. O'Brien, Mechanical Properties of Molybdenum Disulfide and the Effect of Doping: An in Situ TEM Study, ACS Applied Materials & Interfaces, 7 (2015) 20829-20834.

[136] M.R. Hilton, G. Jayaram, L.D. Marks, Microstructure of cosputter-deposited metal- and oxide-MoS2 solid lubricant thin films, Journal of Materials Research, 13 (1998) 1022-1032.

[137] I. Levin, D. Brandon, Metastable alumina polymorphs: Crystal structures and transition sequences, Journal of the American Ceramic Society, 81 (1998) 1995-2012.

[138] G. Paglia, Determination of the structure of y-alumina using empirical and first principle calculations combined with supporting experiments, Department of Applied Physics & Department of Applied Chemistry, Curtin University of Technology 2004.

[139] L.K. Hudson, C. Misra, A.J. Perrotta, K. Wefers, F.S. Williams, Aluminum Oxide, Ullmann's Encyclopedia of Industrial Chemistry, Wiley-VCH Verlag GmbH & Co. KGaA2000.

[140] B. Lux, C. Colombier, H. Altena, K. Stjernberg, Preparation of alumina coatings by chemical vapour deposition, Thin Solid Films, 138 (1986) 49-64.

[141] C. Täschner, B. Ljungberg, V. Alfredsson, I. Endler, A. Leonhardt, Deposition of hard crystalline Al2O3 coatings by bipolar pulsed d.c. PACVD, Surface and Coatings Technology, 108-109 (1998) 257-264.

[142] M. Åstrand, T.I. Selinder, F. Fietzke, H. Klostermann, PVD-Al2O3-coated cemented carbide cutting tools, Surface and Coatings Technology, 188–189 (2004) 186-192.

[143] S. Zhu, F. Wang, H. Lou, W. Wu, Reactive sputter deposition of alumina films on superalloys and their high-temperature corrosion resistance, Surface and Coatings Technology, 71 (1995) 9-15.

[144] O. Zywitzki, G. Hoetzsch, Effect of plasma activation on the phase transformations of aluminum oxide, Surface and Coatings Technology, 76-77 (1995) 754-762.

[145] O. Zywitzki, G. Hoetzsch, Influence of coating parameters on the structure and properties of Al2O3 layers reactively deposited by means of pulsed magnetron sputtering, Surf Coat Technol, 86-87 (1996) 640-647.

[146] O. Zywitzki, G. Hoetzsch, F. Fietzke, K. Goedicke, Effect of the substrate temperature on the structure and properties of Al2O3 layers reactively deposited by pulsed magnetron sputtering, Surface and Coatings Technology, 82 (1996) 169-175.

[147] O. Zywitzki, G. Hoetzsch, Correlation between structure and properties of reactively deposited Al2O3 coatings by pulsed magnetron sputtering, Surface and Coatings Technology, 94–95 (1997) 303-308.

[148] A. Schütze, D.T. Quinto, Pulsed plasma-assisted PVD sputter-deposited alumina thin films, Surface and Coatings Technology, 162 (2003) 174-182.

[149] T. Kohara, H. Tamagaki, Y. Ikari, H. Fujii, Deposition of α-Al2O3 hard coatings by reactive magnetron sputtering, Surface and Coatings Technology, 185 (2004) 166-171.

[150] P. Jin, S. Nakao, S.X. Wang, L.M. Wang, Localized epitaxial growth of α-Al2O3 thin films on Cr2O3 template by sputter deposition at low substrate temperature, Appl Phys Lett, 82 (2003) 1024-1026.

[151] P. Eklund, M. Sridharan, M. Sillassen, J. Bøttiger, α-Cr2O3 template-texture effect on α-Al2O3 thin-film growth, Thin Solid Films, 516 (2008) 7447-7450.

[152] K. Bobzin, N. Bagciian, P. Immich, M. Ewering, Thermal investigation of al203 thin films for application in cutting operations, Adv. Eng. Mater., 11 (2009) 590-594.

[153] K. Bobzin, E. Lugscheider, M. Maes, C. Piñero, Relation of hardness and oxygen flow of Al2O3 coatings deposited by reactive bipolar pulsed magnetron sputtering, Thin Solid Films, 494 (2006) 255-262.

[154] B. Rother, J.Vetter, Plasma-Beschichtungsverfahren und Hartstoff-schichten, Vakuum in Forschung und Praxis, 5 (1993) 53-53.

[155] B. Hallstedt, J. Müller, D. Hajas, E. Münstermann, J.M. Schneider, R. Nickel, D. Parkot, K. Bobzin, E. Lugscheider, Coating of Turbine Blades (TP A3), Integral Materials Modeling: Towards Physics-Based Through-Process Models, John Wiley and Sons2007, pp. 103-124.

[156] K. Bobzin, Oberflächentechnik für den Maschinenbau, Wiley-VCH 2013.

[157] P.M. Martin, W. Andrew, Handbook of Deposition Technologies for Films and Coatings, 3rd ed., Elsevier B.V., New York, 2009.

[158] A. Goswami, Thin Film Fundamentals, New Age International Pvt Ltd Publishers, New Delhi, 1996.

[159] W. Kern, K.K. Schuegraf, 1 - Deposition Technologies and Applications: Introduction and Overview, in: K. Seshan (Ed.) Handbook of Thin Film Deposition Processes and Techniques (Second Edition), William Andrew Publishing, Norwich, NY, 2001, pp. 11-43.

[160] H.E. Rebenne, D.G. Bhat, Review of CVD TiN coatings for wear-resistant applications: deposition processes, properties and performance, Surface and Coatings Technology, 63 (1994) 1-13.

[161] W.R. Grove, On the Electro-Chemical Polarity of Gases, Phil. Trans. Roy. Soc., 142 (1852).

[162] J.E. Greene, Review Article: Tracing the recorded history of thin-film sputter deposition: From the 1800s to 2017, Journal of Vacuum Science & Technology A, 35 (2017) 05C204.

[163] P.J. Kelly, R.D. Arnell, Magnetron sputtering: a review of recent developments and applications, Vacuum, 56 (2000) 159-172.

[164] A. Anders, Cathodic Arcs - From Fractal Spots to Energetic Condensation, Springer Inc., New York, 2008.

[165] J. Vyskočil, J. Musil, Arc evaporation of hard coatings: Process and film properties, Surface and Coatings Technology, 43-44 (1990) 299-311.

[166] D.M. Mattox, Chapter 7 - Physical Sputtering and Sputter Deposition (Sputtering), in: D.M. Mattox (Ed.) Handbook of Physical Vapor Deposition (PVD) Processing (Second Edition), William Andrew Publishing, Boston, 2010, pp. 237-286.

[167] A.S. Penfold, Magnetron sputtering, in: D.A. Glocker, S.I. Shah (Eds.) Handbook of Thin Film Process Technology, Taylor & Francis2002.

[168] B. Window, N. Savvides, Charged particle fluxes from planar magnetron sputtering sources, Journal of Vacuum Science & Technology A, 4 (1986) 196-202.

[169] P. Sigmund, Theory of Sputtering. I. Sputtering Yield of Amorphous and Polycrystalline Targets, Physical Review, 184 (1969) 383-416.

[170] W.D. Westwood, Sputter deposition, AVS, New York, 2003.

[171] S. Maniv, W.D. Westwood, DISCHARGE CHARACTERISTICS FOR MAGNETRON SPUTTERING OF Al IN Ar AND Ar/O//2 MIXTURES, J Vac Sci Technol, 17 (1980) 743-751.

[172] S. Berg, T. Nyberg, H. Blom, C. Nender, Handbook of thin film process technology, Bristol, UK: Institute of Physics Publishing, (1998).

[173] I. Safi, Recent aspects concerning DC reactive magnetron sputtering of thin films: A review, Surface and Coatings Technology, 127 (2000) 203-219.

[174] T. Nyberg, S. Berg, U. Helmersson, K. Hartig, Eliminating the hysteresis effect for reactive sputtering processes, Appl Phys Lett, 86 (2005) 164106.

[175] E. Särhammar, S. Berg, T. Nyberg, Hysteresis-free high rate reactive sputtering of niobium oxide, tantalum oxide, and aluminum oxide, Journal of Vacuum Science & Technology A, 32 (2014) 041517.

[176] W.D. Sproul, D.J. Christie, D.C. Carter, Control of reactive sputtering processes, Thin Solid Films, 491 (2005) 1-17.

[177] J.E. Greene, Chapter 12 - Thin Film Nucleation, Growth, and Microstructural Evolution: An Atomic Scale View, in: P.M. Martin (Ed.) Handbook of Deposition Technologies for Films and Coatings (Third Edition), William Andrew Publishing, Boston, 2010, pp. 554-620.

[178] B.A. Movchan, A.V. Demchishin, STRUCTURE AND PROPERTIES OF THICK CONDENSATES OF NICKEL, TITANIUM, TUNGSTEN, ALUMINUM OXIDES, AND ZIRCONIUM DIOXIDE IN VACUUM, Fiz. Metal. Metalloved. 28: 653-60 (Oct 1969).

[179] J.A. Thornton, Influence of apparatus geometry and deposition conditions on the structure and topography of thick sputtered coatings, Journal of Vacuum Science and Technology, 11 (1974) 666-670.

[180] R. Messier, A.P. Giri, R.A. Roy, Revised structure zone model for thin film physical structure, Journal of Vacuum Science & Technology A, 2 (1984) 500-503.

[181] A. Anders, A structure zone diagram including plasma-based deposition and ion etching, Thin Solid Films, 518 (2010) 4087-4090.

[182] D. Depla, S. Mahieu, J.E. Greene, Chapter 5 - Sputter Deposition Processes, in: P.M. Martin (Ed.) Handbook of Deposition Technologies for Films and Coatings (Third Edition), William Andrew Publishing, Boston, 2010, pp. 253-296.

[183] R. Schneider, Photon Detection, Surface and Thin Film Analysis, Wiley-VCH Verlag GmbH2002, pp. 194-208.

[184] H. Hertz, Ueber einen Einfluss des ultravioletten Lichtes auf die electrische Entladung, Annalen der Physik, 267 (1887) 983-1000.

[185] A. Einstein, Über einen die Erzeugung und Verwandlung des Lichtes betreffenden heuristischen Gesichtspunkt, Annalen der Physik, 322 (1905) 132-148.

[186] V. Totolin, M. Rodríguez Ripoll, M. Jech, B. Podgornik, Enhanced tribological performance of tungsten carbide functionalized surfaces via in-situ formation of low-friction tribofilms, Tribology International, 94 (2016) 269-278.

[187] R.F.K. Herzog, F.P. Viehböck, Ion source for mass spectrography Physical Review, 76 (1949) 855-856.

[188] T. Grehl, Improvement in TOF-SIMS Instrumentation for Analytical Application and Fundamental Research, Mathematisch-Naturwissenschaftlichen Fakultät, Westfälischen-Wilhelms Universität Münster, 2003.

[189] A. Benninghoven, P. Steffens, E. Niehuis, T. Friese, APPLICATION OF A NEW TIME-OF-FLIGHT SIMS, Annual Conference on Mass Spectrometry and Allied Topics, 1983, pp. 54-55.

[190] J.C. Vickerman, Secondary ion mass spectrometry–basic concepts, instrumental aspects, applications and trends. A. BENNINGHOVEN, F. G. RUDENAUER and H. W. WERNER, Wiley, New York, 1987, 1277 pages, Surface and Interface Analysis, 10 (1987) 435-435.

[191] J.C. Vickerman, D. Briggs, ToF-SIMS: Materials Analysis by Mass Spectrometry, 2013.

[192] H. Hutter, Ion Detection, Surface and Thin Film Analysis, Wiley-VCH Verlag GmbH2002, pp. 106-121.

[193] C.V. Raman, A Change of Wave-length in Light Scattering, Nature, 121 (1928) 619.

[194] E.S. Ferrari, K.J. Roberts, D. Adams, A multi-edge X-ray absorption spectroscopy study of the reactivity of zinc di-alkyl-di-thiophosphates (ZDDPS) anti-wear additives:: 1. An examination of representative model compounds, Wear, 236 (1999) 246-258.

[195] A. Morina, A. Neville, Understanding the composition and low friction tribofilm formation/removal in boundary lubrication, Tribology International, 40 (2007) 1696-1704.

[196] A. Tomala, M.R. Ripoll, C. Gabler, M. Remškar, M. Kalin, Interactions between MoS2 nanotubes and conventional additives in model oils, Tribology International, 110 (2017) 140-150.

[197] B. Podgornik, D. Hren, J. Vižintin, Low-friction behaviour of boundary-lubricated diamond-like carbon coatings containing tungsten, Thin Solid Films, 476 (2005) 92-100.

[198] P. Nicolini, R. Capozza, P. Restuccia, T. Polcar, Structural Ordering of Molybdenum Disulfide Studied via Reactive Molecular Dynamics Simulations, ACS Applied Materials and Interfaces, 10 (2018) 8937-8946.

[199] P.A.G. O'Hare, W.N. Hubbard, G.K. Johnson, H.E. Flotow, Calorimetric measurements of the low-temperature heat capacity, standard molar enthalpy of formation at 298.15 K, and high-temperature molar enthalpy increments relative to 298.15 K of tungsten disulfide (WS2), and the thermodynamic properties to 1500 K, The Journal of Chemical Thermodynamics, 16 (1984) 45-59.

[200] A.C. Fischer-Cripps, Critical review of analysis and interpretation of nanoindentation test data, Surface and Coatings Technology, 200 (2006) 4153-4165.

[201] G.M. Pharr, W.C. Oliver, Measurement of Thin Film Mechanical Properties Using Nanoindentation, MRS Bulletin, 17 (1992) 28-33.

[202] G. Kresse, D. Joubert, From ultrasoft pseudopotentials to the projector augmented-wave method, Physical Review B, 59 (1999) 1758-1775.

[203] G. Kresse, J. Furthmüller, Efficient iterative schemes for ab initio total-energy calculations using a plane-wave basis set, Physical Review B, 54 (1996) 11169-11186.

[204] W. Kohn, L.J. Sham, Self-Consistent Equations Including Exchange and Correlation Effects, Physical Review, 140 (1965) A1133-A1138.

[205] J.P. Perdew, K. Burke, M. Ernzerhof, Generalized Gradient Approximation Made Simple, Physical Review Letters, 77 (1996) 3865-3868.

[206] H.J. Monkhorst, J.D. Pack, Special points for Brillouin-zone integrations, Physical Review B, 13 (1976) 5188-5192.

[207] F.D. Murnaghan, The Compressibility of Media under Extreme Pressures, Proceedings of the National Academy of Sciences, 30 (1944) 244.

[208] K. Reuter, M. Scheffler, Composition, structure, and stability of RuO_2 (110) as a function of oxygen pressure, Physical Review B, 65 (2001) 035406.

[209] D.V. Suetin, I.R. Shein, A.L. Ivanovskii, Elastic and electronic properties of hexagonal and cubic polymorphs of tungsten monocarbide WC and mononitride WN from first-principles calculations, physica status solidi (b), 245 (2008) 1590-1597.

[210] Z.T.Y. Liu, X. Zhou, D. Gall, S.V. Khare, First-principles investigation of the structural, mechanical and electronic properties of the NbO-structured 3d, 4d and 5d transition metal nitrides, Computational Materials Science, 84 (2014) 365-373.

[211] W.J. Schutte, J.L. De Boer, F. Jellinek, Crystal structures of tungsten disulfide and diselenide, Journal of Solid State Chemistry, 70 (1987) 207-209.

[212] F. Wang, C. Di Valentin, G. Pacchioni, Electronic and Structural Properties of WO3: A Systematic Hybrid DFT Study, The Journal of Physical Chemistry C, 115 (2011) 8345-8353.

[213] D.B. Migas, V.L. Shaposhnikov, V.N. Rodin, V.E. Borisenko, Tungsten oxides. I. Effects of oxygen vacancies and doping on electronic and optical properties of different phases of WO3, Journal of Applied Physics, 108 (2010) 093713.

[214] C. Kajdas, K. Hiratsuka, Tribochemistry, tribocatalysis, and the negative-ion-radical action mechanism, Proceedings of the Institution of Mechanical Engineers, Part J: Journal of Engineering Tribology, 223 (2009) 827-848.

[215] Z. Chen, X. Liu, Y. Liu, S. Gunsel, J. Luo, Ultrathin MoS2 Nanosheets with Superior Extreme Pressure Property as Boundary Lubricants, Scientific Reports, 5 (2015) 12869.

[216] M. Kalin, J. Kogovšek, M. Remškar, Mechanisms and improvements in the friction and wear behavior using MoS 2 nanotubes as potential oil additives, Wear, 280-281 (2012) 36-45.

[217] M.I. De Barros, J. Bouchet, I. Raoult, T. Le Mogne, J.M. Martin, M. Kasrai, Y. Yamada, Friction reduction by metal sulfides in boundary lubrication studied by XPS and XANES analyses, Wear, 254 (2003) 863-870.

[218] I.L. Singer, T. Le Mogne, C. Donnet, J.M. Martin, In situ analysis of the tribochemical films formed by SiC sliding against Mo in partial pressures of SO2, O2, and H2S gases, J. Vac. Sci. Technol. A Vac. Surf. Films, 14 (1996) 38-45.

[219] I.L. Singer, T.L. Mogne, C. Donnet, J.M. Martin, Third body formation and friction reduction on Mo/SiC sliding in reactive gases, Tribology Series, 1996, pp. 79-90.

[220] K.K. Mistry, A. Morina, A. Erdemir, A. Neville, Extreme pressure lubricant additives interacting on the surface of steel- and tungsten carbide-doped diamond-like carbon, Tribology Transactions, 56 (2013) 623-629.

[221] B. Podgornik, D. Hren, J. Vižintin, S. Jacobson, N. Stavlid, S. Hogmark, Combination of DLC coatings and EP additives for improved tribological behaviour of boundary lubricated surfaces, Wear, 261 (2006) 32-40.

[222] B. Podgornik, J. Vižintin, Tribological reactions between oil additives and DLC coatings for automotive applications, Surface and Coatings Technology, 200 (2005) 1982-1989.

[223] B. Podgornik, J. Vižintin, S. Jacobson, S. Hogmark, Tribological behaviour of WC/C coatings operating under different lubrication regimes, Surface and Coatings Technology, 177-178 (2004) 558-565.

[224] C. Lee, H. Yan, L.E. Brus, T.F. Heinz, J. Hone, S. Ryu, Anomalous Lattice Vibrations of Single- and Few-Layer MoS2, ACS Nano, 4 (2010) 2695-2700.

[225] G.L. Frey, R. Tenne, M.J. Matthews, M.S. Dresselhaus, G. Dresselhaus, Raman and resonance Raman investigation of MoS2 nanoparticles, Physical Review B, 60 (1999) 2883-2892.

[226] A.P.S. Gaur, S. Sahoo, M. Ahmadi, M.J.F. Guinel, S.K. Gupta, R. Pandey, S.K. Dey, R.S. Katiyar, Optical and Vibrational Studies of Partially Edge-Terminated Vertically Aligned Nanocrystalline MoS2 Thin Films, The Journal of Physical Chemistry C, 117 (2013) 26262-26268.

[227] H.A. MacPherson, C.R. Stoldt, Iron pyrite nanocubes: Size and shape considerations for photovoltaic application, ACS Nano, 6 (2012) 8940-8949.

[228] Z. Jin, S. Shin, D.H. Kwon, S.-J. Han, Y.-S. Min, Novel chemical route for atomic layer deposition of MoS2 thin film on SiO2/Si substrate, Nanoscale, 6 (2014) 14453-14458.

[229] Y.-S. Min, E.J. Bae, B.S. Oh, D. Kang, W. Park, Low-Temperature Growth of Single-Walled Carbon Nanotubes by Water Plasma Chemical Vapor Deposition, Journal of the American Chemical Society, 127 (2005) 12498-12499.

[230] E.J. Bae, Y.-S. Min, D. Kang, J.-H. Ko, W. Park, Low-Temperature Growth of Single-Walled Carbon Nanotubes by Plasma Enhanced Chemical Vapor Deposition, Chemistry of Materials, 17 (2005) 5141-5145.

[231] A.C. Ferrari, J. Robertson, Interpretation of Raman spectra of disordered and amorphous carbon, Physical Review B, 61 (2000) 14095-14107.

[232] G. Balakrishnan, P. Kuppusami, S.T. Sundari, R. Thirumurugesan, V. Ganesan, E. Mohandas, D. Sastikumar, Structural and optical properties of γ-alumina thin films prepared by pulsed laser deposition, Thin Solid Films, 518 (2010) 3898-3902.

[233] K. Bobzin, N. Bagcivan, P. Immich, M. Ewering, Thermal investigation of al203 thin films for application in cutting operations, Adv. Eng. Mater., 11 (2009) 590-594.

[234] V. Edlmayr, M. Moser, C. Walter, C. Mitterer, Thermal stability of sputtered Al2O3 coatings, Surface and Coatings Technology, 204 (2010) 1576-1581.

[235] H. Bolt, F. Koch, J.L. Rodet, D. Karpov, S. Menzel, Al2O3 coatings deposited by filtered vacuum arc - characterization of high temperature properties, Surface and Coatings Technology, 116-119 (1999) 956-962.

[236] G. Zhou, L. Wang, X. Wang, Y. Yu, Deposition of nanostructured crystalline alumina thin film by twin targets reactive high power impulse magnetron sputtering, Applied Surface Science, 455 (2018) 310-317.

[237] S. Berg, T. Nyberg, Fundamental understanding and modeling of reactive sputtering processes, Thin Solid Films, 476 (2005) 215-230.

[238] K. Bobzin, N. Bagcivan, M. Ewering, Influence of different pulse parameters on the deposition of Al 2O3, Mater.wis. Werkstofftech., 41 (2010) 670-674.

[239] D. Severin, O. Kappertz, T. Kubart, T. Nyberg, S. Berg, A. Pflug, M. Siemers, M. Wuttig, Process stabilization and increase of the deposition rate in reactive sputtering of metal oxides and oxynitrides, Appl Phys Lett, 88 (2006) 161504.

[240] E. Wallin, U. Helmersson, Hysteresis-free reactive high power impulse magnetron sputtering, Thin Solid Films, 516 (2008) 6398-6401.

[241] S. Berg, A.M. Barklund, B. Gelin, C. Nender, I. Katardjiev, Atom assisted sputtering yield amplification, Journal of Vacuum Science & Technology A, 10 (1992) 1592-1596.

[242] S. Berg, I.V. Katardjiev, Preferential sputtering effects in thin film processing, Journal of Vacuum Science & Technology A, 17 (1999) 1916-1925.

[243] T. Kubart, R.M. Schmidt, M. Austgen, T. Nyberg, A. Pflug, M. Siemers, M. Wuttig, S. Berg, Modelling of sputtering yield amplification in serial reactive magnetron co-sputtering, Surface and Coatings Technology, 206 (2012) 5055-5059.

[244] D. Depla, Z.Y. Chen, A. Bogaerts, V. Ignatova, R. De Gryse, R. Gijbels, Modeling of the target surface modification by reactive ion implantation during magnetron sputtering, Journal of Vacuum Science & Technology A, 22 (2004) 1524-1529.

[245] M. Austgen, D. Koehl, P. Zalden, T. Kubart, T. Nyberg, A. Pflug, M. Siemers, S. Berg, M. Wuttig, Sputter yield amplification by tungsten doping of Al2O 3 employing reactive serial co-sputtering: Process characteristics and resulting film properties, Journal of Physics D: Applied Physics, 44 (2011).

[246] T. Kubart, T. Nyberg, A. Pflug, M. Siemers, M. Austgen, D. Koehl, M. Wuttig, S. Berg, Modelling of sputtering yield amplification effect in reactive deposition of oxides, Surface and Coatings Technology, 204 (2010) 3882-3886.

[247] R.L. Merlino, Understanding Langmuir probe current-voltage characteristics, American Journal of Physics, 75 (2007) 1078-1085.

[248] N.P. Barradas, C. Jeynes, R.P. Webb, Simulated annealing analysis of Rutherford backscattering data, Appl Phys Lett, 71 (1997) 291-293.

[249] W.C. Oliver, G.M. Pharr, Measurement of hardness and elastic modulus by instrumented indentation: Advances in understanding and refinements to methodology, Journal of Materials Research, 19 (2004) 3-20.

[250] J.M. Andersson, E. Wallin, U. Helmersson, U. Kreissig, E.P. Münger, Phase control of Al2O3 thin films grown at low temperatures, Thin Solid Films, 513 (2006) 57-59.

[251] M. Ristić, S. Popović, S. Musić, Structural properties of the system Al_2O_3-Cr_2O_3, Mater Lett, 16 (1993) 309-312.

[252] Y. Kitaoka, K. Nakamura, T. Akiyama, T. Ito, Structural stability and electronic properties in Al2O3–Cr2O3 mixed crystal, Journal of Crystal Growth, 362 (2013) 42-44.

[253] M.G.J. Müller, F. Nahif, J. Mayer, J.M. Schneider, Transmission electron microscopy investigation of the effect of Si alloying on the thermal stability of amorphous alumina thin films deposited by filtered cathodic arc deposition, Surface and Coatings Technology, DOI 10.1016/j.surfcoat.2014.07.088(2014).

[254] K. Bobzin, N. Bagcivan, M. Müller, M. Ewering, R.H. Brugnara, Thermal stability of silicon-doped Al2O3PVD coatings, Mater.wis. Werkstofftech., 44 (2013) 679-683.

[255] Z. Zhou, Z. Li, X. Wang, Y. Liu, Y. Wu, M. Zhao, F. Yin, 700°C isothermal section of Al–Cr–Si ternary phase diagram, Thermochimica Acta, 577 (2014) 59-65.

[256] P. Todeschini, G. Champier, F.H. Samuel, Production of Al-(12–25) wt% Si alloys by rapid solidification: melt spinning versus centrifugal atomization, Journal of Materials Science, 27 (1992) 3539-3551.

[257] A. van der Rest, H. Idrissi, F. Henry, A. Favache, D. Schryvers, J. Proost, J.P. Raskin, Q. Van Overmeere, T. Pardoen, Mechanical behavior of ultrathin sputter deposited porous amorphous Al2O3 films, Acta Materialia, 125 (2017) 27-37.

[258] Y. Wang, H.M. Chan, J.M. Rickman, M.P. Harmer, Effect of oxygen partial pressure on grain-boundary transport in alumina, Acta Materialia, 153 (2018) 205-213.

[259] K. Bobzin, N. Bagcivan, A. Reinholdt, M. Ewering, Thermal stability of γ-Al2O3 coatings for challenging cutting operations, Surface and Coatings Technology, 205 (2010) 1444-1448.

[260] J.M. Schneider, W.D. Sproul, A.A. Voevodin, A. Matthews, Crystalline alumina deposited at low temperatures by ionized magnetron sputtering, J. Vac. Sci. Technol. A Vac. Surf. Films, 15 (1997) 1084-1088.

[261] J.M. Schneider, W.D. Sproul, A. Matthews, Phase formation and mechanical properties of alumina coatings prepared at substrate temperatures less than 500°C by ionized and conventional sputtering, Surface and Coatings Technology, 94-95 (1997) 179-183.

[262] C.M. Koller, N. Koutná, J. Ramm, S. Kolozsvári, J. Paulitsch, D. Holec, P.H. Mayrhofer, First principles studies on the impact of point defects on the phase stability of (AlxCr1−x)2O3 solid solutions, AIP Advances, 6 (2016) 025002.

[263] B. Alling, A. Khatibi, S.I. Simak, P. Eklund, L. Hultman, Theoretical investigation of cubic B1-like and corundum (Cr1−xAlx)2O3 solid solutions, Journal of Vacuum Science & Technology A, 31 (2013) 030602.

[264] A. Khatibi, J. Palisaitis, C. Höglund, A. Eriksson, P.O.Å. Persson, J. Jensen, J. Birch, P. Eklund, L. Hultman, Face-centered cubic $(Al_{1-x}Cr_x)_2O_3$, Thin Solid Films, 519 (2011) 2426-2429.

[265] R. Brill, F. Koch, J. Mazurelle, D. Levchuk, M. Balden, Y. Yamada-Takamura, H. Maier, H. Bolt, Crystal structure characterisation of filtered arc deposited alumina coatings: Temperature and bias voltage, Surface and Coatings Technology, 174-175 (2003) 606-610.

[266] J.A. Vreeling, Y.T. Pei, B. Wind, V. Ocelík, J.T.M. De Hosson, Formation of γ-Al2O3 in reaction coatings produced with lasers, Scripta Materialia, 44 (2001) 643-649.

[267] F. Klocke, K. Gerschwiler, R. Fritsch, D. Lung, PVD-coated tools and native ester - an advanced system for environmentally friendly machining, Surface and Coatings Technology, 201 (2006) 4389-4394.

[268] J. Musil, J. Blažek, P. Zeman, Š. Prokšová, M. Šašek, R. Čerstvý, Thermal stability of alumina thin films containing γ-Al2O3 phase prepared by reactive magnetron sputtering, Applied Surface Science, 257 (2010) 1058-1062.

[269] S. Vuorinen, L. Karlsson, Phase transformation in chemically vapour-deposited κ-alumina, Thin Solid Films, 214 (1992) 132-143.

[270] R. Prescott, M.J. Graham, The formation of aluminum oxide scales on high-temperature alloys, Oxidation of Metals, 38 (1992) 233-254.

[271] K.H. Hellwege, A.M. Hellwege, Crystal Structure Data of Inorganic Compounds, Springer, Berlin, 1975.

[272] J.M. Andersson, Z. Czigány, P. Jin, U. Helmersson, Microstructure of α-alumina thin films deposited at low temperatures on chromia template layers, J. Vac. Sci. Technol. A Vac. Surf. Films, 22 (2004) 117-121.

[273] J. Ramm, M. Ante, H. Brändle, A. Neels, A. Dommann, M. Döbeli, Thermal Stability of Thin Film Corundum-Type Solid Solutions of (Al1–xCrx)2O3 Synthesized Under Low-Temperature Non-Equilibrium Conditions, Adv. Eng. Mater., 9 (2007) 604-608.

[274] J. Ramm, M. Ante, T. Bachmann, B. Widrig, H. Brändle, M. Döbeli, Pulse enhanced electron emission (P3e™) arc evaporation and the synthesis of wear resistant Al-Cr-O coatings in corundum structure, Surface and Coatings Technology, 202 (2007) 876-883.

[275] D. Diechle, M. Stueber, H. Leiste, S. Ulrich, V. Schier, Combinatorial approach to the growth of α-(Al1-x,Crx)2O3 solid solution strengthened thin films by reactive r.f. magnetron sputtering, Surface and Coatings Technology, 204 (2010) 3258-3264.

[276] C.S. Nordahl, G.L. Messing, Thermal analysis of phase transformation kinetics in α-Al2O3 seeded boehmite and γ-Al2O3, Thermochimica Acta, 318 (1998) 187-199.

[277] J.M. McHale, A. Auroux, A.J. Perrotta, A. Navrotsky, Surface energies and thermodynamic phase stability in nanocrystalline aluminas, Science, 277 (1997) 788-789.

[278] K. Jiang, D. Music, K. Sarakinos, J.M. Schneider, Ab initio study of effects of substitutional additives on the phase stability of γ -alumina, J Phys Condens Matter, 22 (2010).

[279] J.M. Andersson, E. Wallin, V. Chirita, E.P. Münger, U. Helmersson, Ab initio calculations on the effects of additives on alumina phase stability, Physical Review B - Condensed Matter and Materials Physics, 71 (2005).

[280] F. Nahif, D. Music, S. Mráz, M. To Baben, J.M. Schneider, Ab initio study of the effect of Si on the phase stability and electronic structure of γ- And α-Al2O3, J Phys Condens Matter, 25 (2013).

[281] D.D. Ragan, T. Mates, D.R. Clarke, Effect of yttrium and erbium ions on epitaxial phase transformations in alumina, Journal of the American Ceramic Society, 86 (2003) 541-545.

[282] C.K. Loong, J.W. Richardson Jr, M. Ozawa, Structural phase transformations of rare-earth modified transition alumina to corundum, Journal of Alloys and Compounds, 250 (1997) 356-359.

[283] A. Douy, Stabilisation of transition aluminas by alkaline earth ions, Key Engineering Materials, 1997, pp. 101-104.

[284] O. Mekasuwandumrong, P. Tantichuwet, C. Chaisuk, P. Praserthdam, Impact of concentration and Si doping on the properties and phase transformation behavior of nanocrystalline alumina prepared via solvothermal synthesis, Materials Chemistry and Physics, 107 (2008) 208-214.

[285] T. Millner, J. Neugebauer, Volatility of the Oxides of Tungsten and Molybdenum in the Presence of Water Vapour, Nature, 163 (1949) 601.

[286] P. Eklund, M. Sridharan, G. Singh, J. Bøttiger, Thermal Stability and Phase Transformations of γ-/Amorphous-Al2O3 Thin Films, Plasma Processes and Polymers, 6 (2009) S907-S911.

[287] M. Hillert, M. Schalin, Modeling of solute drag in the massive phase transformation, Acta Materialia, 48 (2000) 461-468.

[288] M. Hillert, Solute drag, solute trapping and diffusional dissipation of Gibbs energy, Acta Materialia, 47 (1999) 4481-4505.

[289] M. Hillert, Solute drag in grain boundary migration and phase transformations, Acta Materialia, 52 (2004) 5289-5293.